DELFT UNIVERSITY OF TECHNOLOGY
FACULTY OF CIVIL ENGINEERING AND GEOSCIENCES

MASTER THESIS

CIE5060-09

Parametric Instability of an Oscillator Moving on a Railway Track

September 20, 2021

Graduation candidate
Rens van Leijden, 4723899

Hydraulic Engineering

Graduation committee
K.N. van Dalen (chairman)   Dynamics of Solids and Structures
J.M. Barbosa (daily supervisor)   Mechanics and Physics of Structures
M.J.M.M. Steenbergen   Mechanics and Physics of Structures
A.B. Faragau   Dynamics of Solids and Structures
T. Lu   Mechanics and Physics of Structures
A.V. Metrikine   Dynamics of Solids and Structures

TUDelft Delft University of Technology

Dedicated to Dad

Preface

This thesis will, for now, be the last product of my multi-year endeavor following several educations concerning the field of Civil Engineering. The endeavor itself, although taken quite some time as I have reached the age of 26 this year, has been quite interesting. It ultimately ranges from making new friends and having fun with them to finding out where my own interests lay, where both of these have changed quite a bit over time. For example, this thesis is all about moving load dynamics, whilst the master I have followed concerns Hydraulic Structures. Of course, mathematically speaking at least, waves in water or in a beam are not that different.

Although I had not anticipated to be working for almost a year (plus give or take a week) on this thesis, I did enjoy it very much. I do have to add to that statement that there were some periods I did not enjoy, but I think everyone experiences these feelings naturally throughout the progress of researching and writing.

I want to thank everyone that has been involved with me for the past year, namely Karel van Dalen for our several discussions leading up to the subject on which I would focus and for his advice during my thesis. Also, João de Oliveira Barbosa for lending me a hand with his Matlab programme whenever needed and for his support whenever I was in need. Finally, Andrei Faragau for meeting me individually whenever I had to discuss something very specific. I want to thank the three of you as well for treating me professionally and personally in the sense that you all really listened to the things I found out during my work on this thesis, whilst being critical of course, as that really let positive energy flow towards me. Last but not least I must say that I know that I had been working individually on this thesis for too long and had not asked much help until right near the end. That is something I must work on, as doing it all alone will never work.

Finally, as you often see in a preface, I would like to thank my friends, Jesse, and especially my mum for their support and kind words whenever I was grumpy about waiting for days on results from calculations or whenever I did not see the way forward. I wished that dad would have been able to read this as well, I know you would have been proud.

Rens van Leijden,
Rotterdam, July 2021

Contents

List of Figures

List of Tables

Summary

The instability of a moving mass / oscillator due to surpassing the velocity of the minimum group wave velocity (in a continuous homogeneous structure) has been studied extensively and is well understood. In contrary to that, Parametric Instability of a moving mass / oscillator on a continuous periodic structure has been studied less extensive and therefore the mechanism behind the instability is unknown. Literature that is avaiable on this topic mainly focuses on continuous periodic inhomogeneous structures, namely where the foundation is modeled as a continuous periodic inhomogeneous structure. Even less well studied are models where instead of a continuous periodic inhomogeneous foundation discrete periodic supports have been used. So far as known to the author there has also been no studies where the discrete supports are coupled through a medium. In order to solve the transition curves discerning the stable and unstable domains concerning the parametric instability of a moving mass / oscillator the analogy with the Mathieu equation is used, which tells us that the solution on those transition curves will be periodic with once or twice the period of the parametric excitation. In this thesis we have focussed on studying the use of the analogy on continuous structures founded upon periodic supports.

The Mathieu equation describes the motion of a parametric oscillator, for example a pendulum with a length that periodically varies over time. The theory that predicts the solution to the Mathieu equation is called Floquet theory and ascociated with the solution are the Floquet exponents, these exponents dictate whether the solution will be periodic and bounded or unbounded. By solving for the Floquet exponents of the Mathieu one sees that for an increase of the amplitude of the parametric excitation the system will experience a greater exponential growth. For a greater mistuning between the parametric excitation and the natural frequency of the equivalent non-parametrically forced equation we see that the system will experience a smaller exponential growth. Outside the instability domains the solutions will be bounded and periodic and contain a wide variety of frequencies. When damping is introduced, the value of the damping coefficient (if written in the canonical form of a viscously damped single degree of freedom equation) will be subtracted from the value of the undamped Floquet exponents and by that result in an upward shift and narrowing of the transition curves. Furthermore, outside the instability domains we will see two regions: the first lies close the the transition curves and is asymptotically stable with a period equal to that of the transition curve, the second covers the remaining stable region and is asymptotically stable and periodic with a wide variety of frequencies.

Regarding the Parametric Instability of a moving mass / oscillator we have studied three different models: a continuous Euler-Bernoulli beam on periodic spring supports, a continuous Euler-Bernoulli beam on periodic supports that are complex (i.e. modeled as an oscillator between two springs), and a continuous Euler-Bernoulli beam on periodic supports that are founded upon a 2-dimensional lattice. Of these models we have conducted a parametric study as to study what the effects are of the various parameters. We have seen that whenever the ratio between the stiffness of the supports and that of the beam is increased, the instability domains will shift to higher velocities and become wider. For certain combinations also 'islands' of instability may appear, where these 'islands' indicate stable areas between regions of instability. If damping is introduced into the system, this will generally narrow the instability domains and shift them to higher values of the mass and lower values of the velocity. However, for certain parameter combinations adding damping will lead to a widening of the instability domain. In the case of a moving oscillator the instability domains will narrow and be shifted to lower values. If the

support is modeled with a mass it will affect the general trend of the transition curves through its own resonance, hence for a complex structure it is advised to model the supports with the correct dynamic equations. Last but not least, if the supports are coupled through a medium (a 2-dimensional lattice in this case) one will generally see a similar effect as adding damping has.

In this thesis we have also studied three real world cases: a regular railway track, a high-speed railway slab-track, and the Hyperloop. In the first case we have seen that Parametric Instability will most likely have no influence. For the slab-track, being much more stiff, Parametric Instability will be important. However, a more extensive study with several cases must confirm this. In the last case, namely the Hyperloop, we have seen that for a moving mass the instability domains are relatively large as compared with the other cases. We have also studied the Parametric Instability of a test-pod, which showed that its instability domains that are negligible. Of course, this was merely a test-pod not capable of transporting people, hence when a larger pod is studied it may be expected that the instability domains may not be neglected.

Chapter 1

Introduction

1.1   Background

If one takes a good look around, periodic structures may be found everywhere. Examples are the periodic sleepers supporting a railway, the periodic structure of offshore platform legs [6], a multi-span viaduct [28], fluid-duct-systems [13], and even in architecture we find repetition due to aesthetic reasons. Often, periodic structures are applied due to their cost-effectiveness. However, more often than not the use is just a consequence of the type of structure that is built (e.g. a railway). Many of these aforementioned types of structures are subjected to dynamic loading, which may be in the form of a moving load (e.g. moving train) or even the dynamic forcing by wave attack. In any case, the periodic nature of the structure has a significant effect on the dynamic behaviour.

In any continuous homogeneous structure that is subjected to a moving load, waves will be generated that are either evanescent or propagative. It is well known that if the moving load travels with the minimum group velocity of those waves that do propagate, resonance of the structure will occur. Furthermore, if we expand on this and treat a moving mass instead of a moving load, surpassing this velocity can induce instability of the vertical vibrations of this mass. This instability is known to be ascociated with the radiation of anomalous Doppler waves [40, 58]. This type of instability only occurs in the super-critical velocity range (i.e. $V_{mass} > V_{min,phase}$).

Another type of instability, appropriately named Parametric Instability, may occur when either the type of dynamic loading is parametric or the structure itself induces a periodicity to the loading. An example of the first case would be a single-span viaduct which is loaded by periodical traversing masses [53]. Obiously, the structure itself is not periodic in this case. In contrast, a railway track is a periodic structure as it is periodically founded on sleepers. If a mass moves over this structure it will feel a periodically varying stiffness. In the former case, the motion of the structure may become unstable, whereas in the latter case the motion of the mass (and by that the structure as well).

The importance of studying this type of instability can mainly be attributed to the fact that it may occur in the sub-critical domain (i.e. $V_{mass} < V_{min,phase}$). This significantly lowers the range of velocities where instability might be an important factor.

1.2 Aims and Scope

As written above, Parametric Instability originates from the periodic nature of a structure and may for example be described by the Mathieu equation [31]. The Mathieu equation itself has been rigorously studied by numerous researchers, for example Acar [2] treated the stability and response frequencies of the undamped and damped Mathieu equation, Afzali [3] treated the stability and response frequencies of the periodically damped Mathieu equation, and Kovacic [24] treated the stability of the Mathieu equation with nonlinearities. All previous work done is based on Floquet theory [64], which gives us the mathematical framework to solve an ordinary differential equation with periodic coefficients. Others have used that theory as an analogy in the derivation of Parametric Instability for more complex systems, namely the instability of a moving mass on a periodic guideway, for example Verichev [57] made an analytic derivation of the instability of a moving mass on an Euler-Bernoulli beam with a continuous periodically inhomogeneous guideway, Metrikine [41] made a semi-analytic derivation for a moving mass on a periodically discrete supported infinite string, and Abe [1] made a semi-analytic derivation for a moving oscillator on a periodically discrete supported Timoshenko beam. Interesting to note here is that as far as is known only Abe [1] derived the magnitude of the instability for such a system as well. The latest addition to this type of research has been made by V. Oostrum [56], whom considers the coupled parametric instability of a moving oscillator on a periodically inhomogeneous foundation.

Of the mentioned literature that consider the parametric instability of a moving mass / oscillator on a periodic guideway, only Abe [1] considers higher instability zones. He has also been the only one that treats the influence of support if they have their own degree of freedom, albeit in a very simple manner (i.e. by using an equivalent dynamic stiffness based on one frequency). Also, no one has considered the case where the supports are coupled through the foundation, for example by a continuous half-space on which the supports have been founded. Furthermore, the Euler-Bernoulli beam has only been treated on a periodically inhomogeneous continuous foundation. Last but not least, the analogy between the Mathieu equation and the instability of a moving mass / oscillator on a periodic guideway has merely been adopted and used, it has not been verified numerically if the solution indeed is unstable in the instability domain. Considering literature regarding the Mathieu equation, Floquet exponents have been calculated [2, 3] however not in an extensive manner. The main focus has always been on the boundaries themselves.

1. Our first goal is thus to extend the study of the Floquet exponents of the Mathieu equation. We derive with the help of Floquet theory the Floquet exponents for a wide variety of system parameters, giving us a complete overview of the dynamic behaviour of the solutions to that equation. Doing so will allow us to analyse how far the analogy with Parametric Instability of a moving mass / oscillator on a guideway applies.

Since only little research has focused on discrete supports and none where these are coupled through the foundation as well, it is of interest to extend on the existing literature as was mentioned above.

2. Our second goal is thus to perform a parametric study on Parametric Instability in a variety of different models. The first model contains discrete spring supports, the second model has more complex supports that act as an oscillator (i.e. a movable mass between

two springs), and the third model accounts for the coupling by introducing a 2-dimensional lattice that will represent the foundation of the guideway. The importance of Parametric Instability in several real world applications is studied as well. All of these models are based on an Euler-Bernoulli beam model.

As mentioned above, so far as is known there have been no numerical verification of Parametric Instability of a moving mass / oscillator on a guideway. In order to do so, a Finite Element Model (FEM) will be used with which the time-domain response of periodic structures may be calculated.

3. Our third and final goal is thus to perform numerical time-domain calculations with the use of a Finite Element Model to verify the calculated transition curves (lines denoting the stable and unstable domains). To do so, critical locations will be chosen that define the transition of stable to unstable motion. With these numerical results we will also be able to verify the analogy between the Mathieu equation and the occurence of Parametric Instability in periodic structures.

1.3 Thesis Outline

As one may have seen already from the list of Contents, this thesis does have a fair amount of both pages and appendices. The variety and amount of work done over the course of studying this particular subject has certainly been the cause of this. The most important reason however is the fact that all theory related to the problems in this thesis are discussed in a great variety of literature, however no single paper or book was found that covers most of it. Hence one may treat this thesis as most of that information being compiled into one report, albeit distributed over the main body and appendices according to its importance and relation with the goals that were given above. Furthermore, this thesis may be treated as two different parts: the first being related to the Mathieu equation and the second to periodic structures. Although conclusions from the first part are used in the second, they may be read separately from each other.

In Chapter 2 we cover available literature of both the Mathieu equation and that of periodic structures. Wherever necessary we will make our own derivations as to expand on the available literature. Regarding the Mathieu equation we will discuss Floquet theory and the method to derive the transition curves and Floquet exponents. In case of periodic structures we will discuss their wave propagation properties, methods to derive these properties, their response to a moving (harmonic) load and how to use the latter in order to calculate the transition curves for a moving mass / oscillator.

In Chapter 3 we will introduce the method by deriving the transition curves of both the undamped and damped Mathieu equation. Afterwards we will derive the Floquet exponents of both the undamped and damped Mathieu equation.

In Chapters 4, 5, and 6 we will verify the method with previous literature, perform parametric studies, and treat several real world applications.

Finally, in Chapter 7 we will perform numerical time-domain calculation with a FE model as to verify the results of the semi-analytical calculations in the former chapters. We will also consider the analogy between Parametric Instability of the Mathieu equation and that of a moving mass / oscillator.

Chapter 2

Literature review and relevant theory

2.1 The Mathieu equation and Parametric Instability

The Mathieu equation, which is actually a specific case of the more general Hill's equation, is a famous linear differential equation with periodic coefficients. Originally proposed by Leonard Mathieu [31] for solving the vibrational behaviour of an elliptic drum, it has been subjected to further research in a lot of literature, ranging from proposing solution methods such as perturbation methods and the application of Floquet theory [47, 49, 48], harmonic balancing [24], a combination of Floquet theory and harmonic balancing [3, 2] and even using the general results for solving problems with analogies to the Mathieu equation [41, 1].

A different form of the Mathieu equation as presented by Kovacic [24] will be used throughout this thesis. This equation reads as follows:

$$\ddot{x}(t) + [\delta + \mu cos(t)]x(t) = 0 \tag{2.1.1}$$

where δ is analogous to ω_0^2 in the well known Single Degree of Freedom equation. In contrary to the original Mathieu equation, the parametric forcing period now has a period of $T = 2\pi$ s (or rather $\omega_p = 1$ rad/s, with ω_p being the frequency of parametric forcing).

In section 2.1.1 we cover some basic results from Floquet theory applicable on an undamped Mathieu equation, whereas this is extended to a damped Mathieu equation in section 2.1.2. Finally, in section 2.1.3 we shortly discuss the method of solution to obtain the boundaries discerning stable from unstable motion.

2.1.1 Floquet theory in the undamped case

As Floquet theory applies to ordinary differential equations (ODE's) with periodic coefficients, we will give the general form of such an equation for our discussion of the theory:

$$\ddot{x}(t) + p(t)x(t) = 0, \quad p(t + T) = p(t) \tag{2.1.2}$$

Since Eq. 2.1.2 (actually Hill's equation) is a second order ODE there exist two linearly independent, non-vanishing solutions: often referred to in literature as a *'fundamental set of solutions'*. This is also known from linear second order ODE's with constant coefficients, of which the general solution is very well known. Now, Floquet theory tells us the general solution to Eq. 2.1.2 may be written as follows:

$$x(t) = \mathrm{e}^{\lambda t} \phi(t) \quad where \ \phi(t + T) = \phi(t) \tag{2.1.3}$$

Thus, the general solution consists of a periodic term which is periodic with the same T as the parametric excitation and an exponential term of which the exponent may be either real, purely imaginary or complex valued. A direct inspection of Eq. 2.1.3 shows that the solutions will be bounded if the coefficient λ of the exponential function (called the *characteristic-* or *Floquet exponent*) will be zero or purely imaginary. Whenever one of the Floquet exponents has a real part that is positive, the solution will grow exponentially and thus be unstable. This type of instability is called Parametric Instability. As mentioned in [49], on the transition curves from stable to unstable motion, the Floquet exponents lead to general solutions that are periodic[1] with either $\underline{T}$ or $\underline{2T}$, hence the motion is in direct relation with the forcing period and $\underline{not}$ the natural period of vibration. This makes sense, since the system is periodically forced. Although the forcing is now a parametric excitation instead of a 'normal' forcing (i.e. the differential equation is homogeneous). From now on we will refer to the values T and $2T$ as T_1 and T_2 respectively. As mentioned above, at the boundaries between instability and stability one of the general solutions is purely periodic with either T_1 or T_2. Aside from the exponential growth, the imaginary part of the Floquet exponent will influence the periodic motion as well. This, and more, will become clear with the use of Floquet theory.

From Floquet theory [64] we know that the Floquet exponents are related via:

$$\rho_i = \varphi \pm \sqrt{\varphi^2 - 1}$$

$$\lambda_1 + \lambda_2 = 0 \tag{2.1.4}$$

$$\text{Where: } \rho_i = \mathrm{e}^{\lambda_i T}$$

Here, ρ_i is called a Floquet multiplier and $\varphi = \frac{1}{2}(x(T) + \dot{x}(T))$, thus defining the growth of the system over one period of time[2]. From Eq. 2.1.4b it becomes clear that there are five distinct zones defining different types of vibrations and stability, Ward [64] gives:

---

[1]In reality however, only one of the two solutions is periodic with T or 2T. The other actually increases linearly with t due to the multiplicity of the eigenvalue [64]. However, using the fact that only one solution is periodic is enough to find the transition curves.

[2]Note that $x(T)$ is related to initial conditions: $x(0) = 1$, and $\dot{x}(0) = 0$. And $\dot{x}(T)$ is related to initial conditions: $x(0) = 0$, and $\dot{x}(0) = 1$.

$$\varphi < -1 \rightarrow x(t) = c_1 e^{\lambda t} q_1(t) + c_2 e^{-\lambda t} q_2(t), \quad where \ q_i(t+2T) = q_i(t)$$

$$\varphi = -1 \rightarrow x(t) = (c_1 + tc_2)q_1(t) + c_2 q_2(t)$$

$$-1 < \varphi < 1 \rightarrow x(t) = c_1 \operatorname{Re}\{e^{i\sigma t}p(t)\} + c_2 \operatorname{Im}\{e^{i\sigma t}p(t)\}, \quad where \ p(t+T) = p(t) \qquad (2.1.5)$$

$$\varphi = 1 \rightarrow x(t) = (c_1 + tc_2)p_1(t) + c_2 p_2(t), \quad where \ p_i(t+T) = p_i(t)$$

$$\varphi > 1 \rightarrow x(t) = c_1 e^{\lambda t}p_1(t) + c_2 e^{-\lambda t}p_2(t)$$

How these functions $p_i(t)$ and $q_i(t)$ arise from the Floquet exponents and the definition of σ, may be found in Ward [64]. Just note that σ is real here, thus leading to stable motion for $-1 < \varphi < 1$.

As becomes clear from Eq. 2.1.5, we can determine the regions of stability by numerically calculating the value of φ. Where $|\varphi| > 1$ will lead to instability and $|\varphi| < 1$ to neutral stability. This makes sense, since no damping has been added to the system due to which asymptotic stability may occur. The value of φ can be derived by combining Eqs. 2.1.4, here we take the equation directly from Ward [64]:

$$\varphi = \cosh(\lambda_i T) \qquad (2.1.6)$$

With Eq. 2.1.6 the values of φ may be found in a different manner by solving for the Floquet exponents λ_i, which will be shown in 2.1.3. Furthermore, it is possible to quantify the exponential growth by taking the asbolute value of the real part of only one of the Floquet exponents (since they are related via Eq. 2.1.4c).

Thus, by using Floquet theory we are able to calculate for any combination of parameters whether the solution will be stable of unstable, which will give a more complete picture of the behaviour of the solutions. As opposed to only searching for the boundaries decerning between stable and unstable motion.

2.1.2 Floquet theory in the damped case

As the preceding section was based on an undamped ODE with periodic coefficients, we have to expand on the theory allowing us to include damping. Therefore, the equations used in section 2.1.1 above (i.e. Eqs. 2.1.4, 2.1.5, and 2.1.6) must be derived again. This may be done by employing the following relationship [64, 2]:

$$\rho_1 \rho_2 = \exp\left(\int_0^T \operatorname{tr}(A(s))ds\right) \qquad (2.1.7)$$

where $A(s)$ is the state-space coefficient matrix for the following damped Mathieu equation:

$$\ddot{x}(t) + 2\zeta\dot{x}(t) + [\delta + \mu cos(t)]x(t) = 0 \qquad (2.1.8)$$

Note that Eq. 2.1.8 differs from the standard canonical form of the EoM for a damped oscillator. Since the solution belonging to that equation does not have any meaning for the Mathieu equation, defining the damping ratio per (eigen)period of oscillation does not make any sense. Its state-space coefficient matrix now reads as follows:

$$A = \begin{bmatrix} 0 & 1 \\ -(\delta + \mu \cos(t)) & -2\zeta \end{bmatrix} \qquad (2.1.9)$$

Carrying out the integration and simplifying the expression gives

$$\rho_1 \rho_2 = e^{-2\zeta T} \quad \text{or,}$$

$$\lambda_1 + \lambda_2 = -2\zeta \qquad (2.1.10)$$

where these results are confirmed by Acar [2]. To be able to define the stability regions one more equation must be used, taken directly from Ward [64] as this will not change in the damped case:

$$\rho_1 + \rho_2 = 2\varphi \qquad (2.1.11)$$

Solving Eqs. 2.1.10a and 2.1.11 for ρ gives:

$$\rho_i = \varphi \pm \sqrt{\varphi^2 - e^{-2\zeta T}} \qquad (2.1.12)$$

The relationship with the undamped case is clearly seen, as setting $\zeta = 0$ leads to the original undamped relation, confirming the validity of the derivation. It is observed that the instability regions defined by φ are altered by the inclusion of damping, due to the value of $e^{-2\zeta T}$. The regions of stability change as well, adding two new zones. This may be seen by realising that for $|\rho_{1,2}|$ equal to 1 (i.e. defining the boundary between stable and unstable motion), a different value of ϕ is found. In the undamped case this was equal to $|\varphi| = 1$, defining a boundary with a transition from $|\rho_{1,2}|$ being real and larger than one, to being complex. In the damped case this boundary is equal to $\varphi = \left| e^{-\zeta T} \right|$, which upon substitution in Eq. 2.1.12 will give values of $|\rho_{1,2}| < 1$. Thus a new boundary may be found by searching for the values of $|\rho_{1,2}| = 1$. It can be shown that this will give

$$\varphi = \pm \left(\frac{e^{-2\zeta T}}{2} + \frac{1}{2} \right) \qquad (2.1.13)$$

such that the different regions are now defined as:

$$\begin{aligned} &a : \varphi < -\frac{e^{-2\zeta T}}{2} - \frac{1}{2}, && e : \varphi = e^{-\zeta T} \\ &b : -\frac{e^{-2\zeta T}}{2} - \frac{1}{2} < \varphi < -e^{-\zeta T}, && f : e^{-\zeta T} < \varphi < \frac{e^{-2\zeta T}}{2} + \frac{1}{2} \\ &c : \varphi = -e^{-\zeta T}, && g : \varphi > \frac{e^{-2\zeta T}}{2} + \frac{1}{2} \\ &d : -e^{-\zeta T} < \varphi < e^{-\zeta T} \end{aligned} \qquad (2.1.14)$$

Following Ward [64] and the solutions given in Eq. 2.1.5, we can determine the types of solutions belonging to the zones as defined in Eqs. 2.1.14 above. Due to the addition of a new zone where $|\rho_{1,2}| < 1$ and $\rho_1 \neq \rho_2$, the solution will be asymptotically stable with period T_2 for Eq. 2.1.14b and T_1 for Eq. 2.1.14f. As will be shown below, in these stable areas the period will remain constant whilst the exponential damping will decrease from $e^{-\zeta}$ to zero. The remaining zones will be similar to the ones from Eqs. 2.1.5.

To gain some further insight, the absolute values of Eqs. 2.1.4b, and 2.1.12 are plotted for values of φ and can be found in Figs. 2.1a, and 2.1b. Furthermore, we can use the definition of $|\rho_{1,2}|$ to see which values the real and imaginary part of $\lambda_{1,2}$ will attain. To that end, the real and imaginary parts of $\lambda_{1,2}$ will be plotted as well and can be found in Figs. 2.2a and 2.2b below.

(a) $\rho_{i,\zeta=0}$ for different values of φ

(b) $\rho_{i,\zeta=0.05}$ for different values of φ
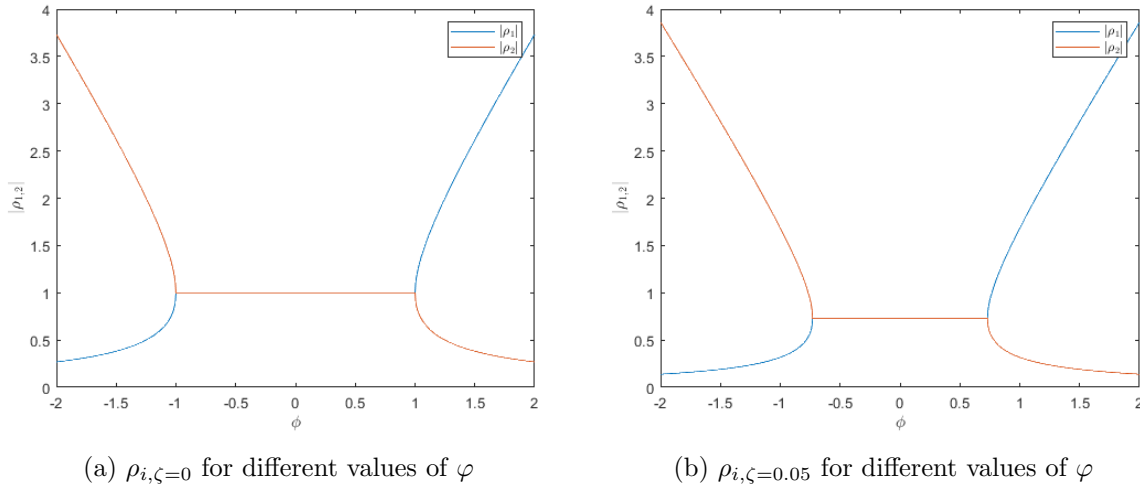
Figure 2.1: Floquet multipliers for different values of φ

(a) $\rho_{i,\zeta=0}$ for different values of φ

(b) $\rho_{i,\zeta=0.05}$ for different values of φ
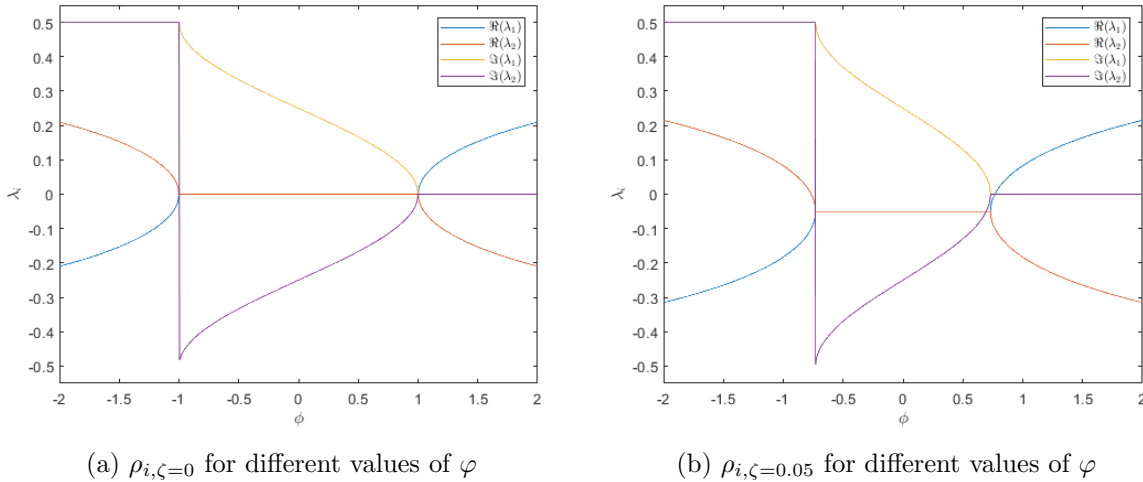
Figure 2.2: Floquet exponents for different values of φ

As becomes clear from the aforementioned figures, for $\zeta = 0$ the values of $|\rho_{1,2}|$ in the zone of stability are equal to 1, complying with Ward [64]. When damping is added, in the range defined by Eq. 2.1.14d the Floquet multipliers will have values: $|\rho_{1,2}| = e^{-\zeta T}$. In the range defined by Eqs. 2.1.14b, and 2.1.14f these will have values: $e^{-\zeta T} < |\rho_{1,2}| < 1$. In both these

ranges the solution will be asymptotically stable. Further increasing the value of ζ will lead to a narrowing of the zones where $|\rho_{1,2}|$ is complex and smaller than 1. One might be tempted to think this would increase the zones of instability, as a smaller value of φ is needed to reach instability. However, it makes sense that by increasing the damping the value of φ will decrease as well (remember its definition), such that although the instability zone as defined by φ might increase, the value of φ itself will decrease, effectively counterbalancing the aforementioned increase.

From Figs. 2.2a and 2.2b we can see that in the case of the undamped Mathieu equation the real part of $\lambda_{1,2}$ will be zero in the stable region, whereas they are equal but opposite in sign in the unstable regions. Furthermore the imaginary value clearly shows vibration with period T_2 for $\varphi < 1$ and with period T_1 for $\varphi > 1$, whereas these are equal but opposite in sign and vary in the stable region. In the damped case, both real parts attain the value of $-\zeta$ in the stable region where $|\rho_1| = |\rho_2|$, and vary with constant phase value (i.e. imaginary part of $\lambda_{1,2}$) in the remaining 4 regions. Additionally, we see that the phase constant defined by $\text{Im}\{\lambda_{1,2}\}$ does not change by the addition of damping.

The last thing to do is derive φ from Eqs. 2.1.10b, and 2.1.11, which as defined by only one of the Floquet exponents lead to

$$\varphi = \frac{e^{\lambda_1 T}}{2} + \frac{e^{(-2\zeta - \lambda_1)T}}{2} \tag{2.1.15}$$

such that the equation above can be used to determine the value of φ and with that the different regions.

2.1.3   Hill's infinite determinant

As shown above, on the boundaries between stable and unstable motion the general solution will be periodic with either T_1 or T_2. As explained by Nayfeh [49] and applied by Metrikine's [41], one may find these boundaries by constructing Hill's determinant. In order to derive Hill's determinant, one may apply two infinite Fourier series (with periods T_1 and T_2 respectively) to the ODE. Metrikine [41] gives:

$$x(t) = A_n \cos 2nt + B_n \sin 2nt, \quad n = 0, 1, 2, \ldots \quad \text{for periodic motion with } T_1 = \pi$$

$$x(t) = A_n \cos(2n-1)t + B_n \sin(2n-1)t, \quad n = 1, 2, 3, \ldots \quad \text{for periodic motion with } T_2 = 2\pi \tag{2.1.16}$$

It is chosen to use the complex forms of the equations above for solving the transition curves, which will result in a method analogous to Metrikine [41] (only easing up the mathematics) and to the one used by Nayfeh [49] to obtain Hill's infinite determinant (but ignoring the exact solution). The complex form of the equations above are written as follows:

$$x(t) = \sum_{n=-\infty}^{\infty} A_n e^{2int}, \quad \text{for periodic motion with } T_1 = \pi$$

$$x(t) = \sum_{n=-\infty}^{\infty} A_n e^{(2n-1)int}, \quad n \neq 0, \quad \text{for periodic motion with } T_2 = 2\pi \tag{2.1.17}$$

In order to derive Hill's determinant one now proceeds by substituting Eqs. 2.1.17 in Hill's equation (i.e. Eq. 2.1.2), whereafter the harmonic balance method [49] may be applied to derive an infinite set of linear, algebraic, homogeneous equations in terms of the coefficients A_n. This set of equations can be solved by truncating up to a certain value of n, collecting all terms in a coefficient matrix and subsequently solving this by equating its determinant to zero. This results in a characteristic equation in terms of the systems parameters, whose combinations will define the location of the boundaries.

In Chapter 3 we will apply Floquet theory and make use of Hill's determinant on the undamped and damped Mathieu equation to show how the general method of solution works in practice.

2.2   1-Dimensional periodic structures

The very first appearance of periodic systems was due to Newton, who tried to derive the velocity of sound trough air with the use of an infinite 1-dimensional lattice [14]. Floquet derived the general solution for differential equations with periodic coefficients, whereas Bloch expanded and generalised this to three dimensions as to solve the Schrödinger equation with periodic boundary conditions [52]. Often, Bloch's theorem is called Bloch-Floquet theorem and the ascociated waves are called Bloch waves [13].

Brillouin showed via a perturbation analysis that infinite lattices behave similar to the general solution used in Bloch-Floquet theory [14] and subsequently applied the general solution to obtain infinite determinants similar to Hill's infinite determinant. Similar to Floquet theory, curves may be derived from these determinants, where these curves now indicate stop- or propagation-bands instead of instability zones. The variables associated with these curve are often called the propagation coefficients[14] and essentially give the dispersion curves of a periodic system. Furthermore, Brillouin showed that there is an ambiguity in the wavenumber defined by the periodic distance of the system. Dispersion curves will show the typical property that the frequency of different modes are a periodic function with period $k/2$ (which is a nice analogy to the Nyquist frequency in Fourier analysis of signals).

Mead formulated a method to calculate the propagation coefficients of infinite periodic structures based on receptances of one periodic element [32], the dynamic stiffness matrix [37], and by flexural wave analysis [36]. He also showed how to deal with mono- and multi-coupled systems with one or two directions, the influence of finite systems or damping on the propagation coefficients, and the relation of the latter with the natural frequencies of the free and locked single elements[3] [34, 35, 33]. Furthermore he derived the forced response of both finite [38] and infinite [39] periodic systems by means of a flexural wave analysis. Banerjee [7], Kumar [25] and Asiri [6] used the transfer matrix method to derive the propagation coefficients. Abe [1] uses the general solution to a periodic system with which an infinite determinant analogous to Hill's infinite determinant is derived. Opposed to the previous methods, this one also allows the calculation of the magnitude of the exponential growth of the solutions.

The wave propagation properties of periodic discrete/continuous structures will be covered in section 2.2.1. Next, in section 2.2.2 we will cover the application of the Transfer Matrix Method that allows us to derive the Dispersion curves of periodic structures. In section 2.2.3 an overview will be given of methods by which one can calculate the response of periodic structures to a

---

[3]Free: simply supported beam, Locked: clamped beam on both ends

moving (harmonic) load. One of these methods has been chosen and an elaborate derivation will be given from which the periodicity condition [9, 41] naturally arises. We will also shortly discuss the infinite kinematic invariant as this will aid us in our discussion later on. The results from section 2.2.3 will be used in the calculation of the transition curves for which the mathematical framework will be laid in section 2.2.4.

2.2.1 Wave propagation properties of periodic structures

Waves in a periodic structure have some different properties as opposed to waves in continuous structures. First of all, as mentioned above, there exists an ambiguity in the observable wavelengths. In a discrete periodic system, for example a 1-dimensional lattice, wavelengths shorter than the periodic length $2L$ cannot be observed. Very much the same as with digital signal processing and therefore the Nyquist frequency. This also results in the dispersion curve, relating wavenumber and frequency, showing a periodic property. That is, the wavenumber is periodic with $\frac{2\pi}{L}$. This property may be observed in Fig. 2.3, where the 2π part is not taken into account. Fig. 2.3b shows the same curve as 2.3a, however only over the first Brillouin zone. Where the Brillouin zones are defined as the zones over which the dispersion curves show a periodic property. This property is also the reason why the inverse Floquet transform is over one Brillouin zone instead of over the whole range of $[-\infty, \infty]$, in perfect analogy with the Discrete Time Fourier Transform (DTFT) [22].
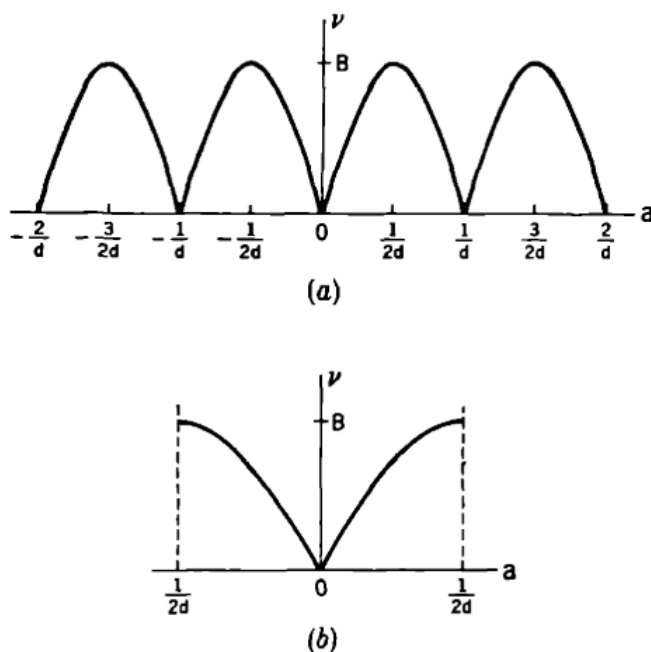
Figure 2.3: 1-dimensional lattice from Brillouin [14]; (a) frequency as function of wavenumber; (b) first Brillouin zone

Apart from the mentioned ambiguity, waves in periodic structures also show wave attenuation without the inclusion of damping. Actually, for a 1D-lattice with possible motion in one direction, there exists a critical frequency after which wave propagation is not allowed and only wave attenuation occurs. An example of this is shown in Fig. 2.4, where the solid line defines the dispersion relation for propagating waves and the dashed line gives the amount of attenuation

of the wave. The mathematical interpretation of these values would be as follows:

$$
\begin{array}{c|c}
\text{for real } a & \text{for imaginary } \beta \\[2mm]
w(x,t) = \mathrm{e}^{\mathrm{i}(\omega t - ax)} & w(x,t) = \mathrm{e}^{-\beta x}\mathrm{e}^{\mathrm{i}\omega t}
\end{array}
\tag{2.2.1}
$$

The frequency-band where wave propagation is allowed is denoted as the propagation-band, whereas the attenuation band is denoted as either attenuation- or stop-band.
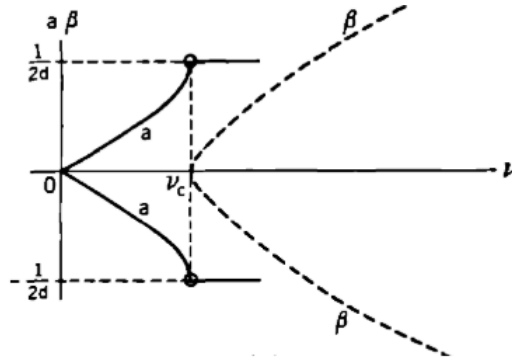
Figure 2.4: existence of a critical frequency [14]

The example of Brillouin [14] in Figs. 2.3 and 2.4 were derived for a 1 DoF 1D-lattice. He continues his discussion for lattices with multiple degrees of freedom and eventually expands that to 2D and 3D lattices. As our interest right now lies with 1D continous periodic structures, we must shift our view a little bit and forget about lattices. Instead, we will focus on continous periodic structures, which have been extensively discussed by Mead and others.
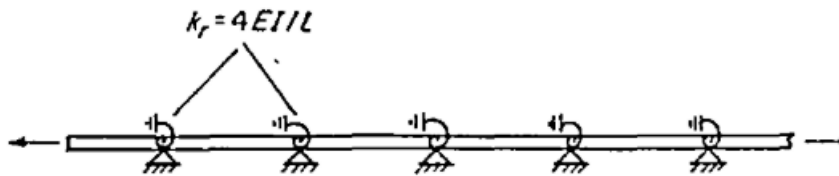
Figure 2.5: Example continuous periodic structure with 1 DoF [32]

Although the same periodicity for the dispersion equation occurs, the ambiguity between possible wavelength is not present in the same manner as for discrete periodic structures (more on this later). Another important difference is the fact that even in the case where we have one Degree of Freedom (DoF) at every support (e.g. Fig. 2.5), there will be multiple 'critical frequencies', defining multiple stop- and propagation bands [32]. These frequencies are defined by the bounding frequencies and have a close relation with natural frequencies of the single elements [35]. In the example of Fig. 2.5 only rotational motion is possible, due to the simple support, which will lead to the existence of only one propagation coefficient and thus only one Bloch wave [32]. If we were to have supports with a spring, vertical motion would also be possible and this would thus lead to two propagation coefficients.

Waves in periodic structure, also called Bloch waves, may be represented by:

$$\Psi(x) = A(x)\mathrm{e}^{\lambda x}, \quad \text{with } A(x+L) = A(x) \tag{2.2.2}$$

If one advances one period, the equation above gives the following Bloch boundary condition (B.C.):

$$\Psi(x+L) = \mathrm{e}^{\lambda L}\Psi(x) \tag{2.2.3}$$

Here, λ denotes the Bloch wave number, which may be either real, imaginary, or complex. Several literature discuss the Bloch wave number, also calling it the propagation coefficient [32], which seems most appropriate as it dictates the difference in amplitude and phase of the solution from one cell to the other. However, from here on we will call it the eigenvalues of the periodic system. The different values this eigenvalue may take can be summarised as follows [66, 62]:

- $\mathrm{Re}\{\lambda L\} \neq 0$, $\mathrm{Im}\{\lambda L\} = n\pi \to$ attenuation band: The real part dictates the amplitude decay, whereas the imaginary part determines whether the reponse is in-phase or out of phase. n may be any integer value. Either a standing or evanescent wave;

- $\mathrm{Re}\{\lambda L\} = 0$, $\mathrm{Im}\{\lambda L\} \neq n\pi \to$ propagation band: with the imaginary part not being equal to $n\pi$, propagation from one bay to another is now possible without attenuation;

- $\mathrm{Re}\{\lambda L\} \neq 0$, $\mathrm{Im}\{\lambda L\} \neq n\pi \to$ complex band: a propagating wave which decays exponentially with distance, where the eigenvalues occur as complex conjugates.

Examples of the real and imaginary parts of the eigenvalue are shown in Figs. 2.6 and 2.7, which correspond to the example shown in Fig. 2.5.
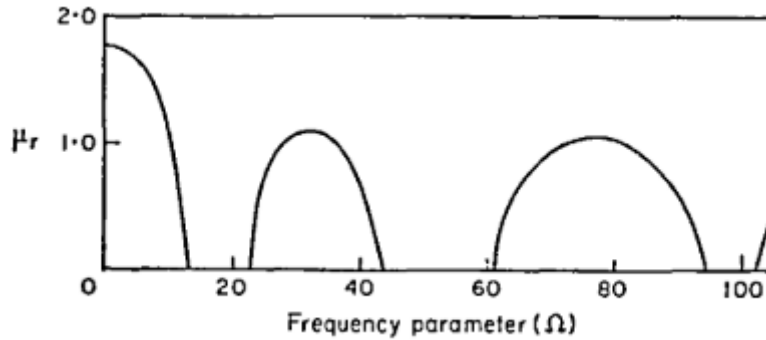
Figure 2.6: example real part of propagation constant [32]

As can be seen from the figures, in the so called attenuation- or stop-bands the real part varies in value starting at zero and returning to zero, whilst the imaginary part is constant with either 0 or a multiple of π. The border between propagation and attenuation bands are governed by the bounding frequencies, which in the case of symmetric elements are given by the natural frequencies of a single element [34]. More complex behaviour may also be observed [66, 7, 62, 63, 13, 6], depending on the type of periodic elements. An example is shown in Fig. 2.8, do note that due to the definition in that paper the real part now dictates wave propagation and the imaginary part the attenuation.
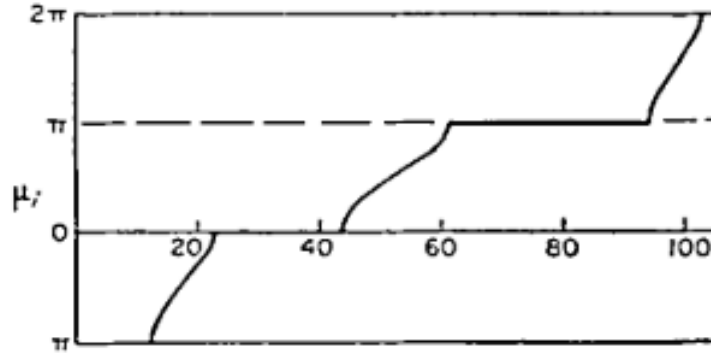
Figure 2.7: example imaginary part of propagation constant [32]
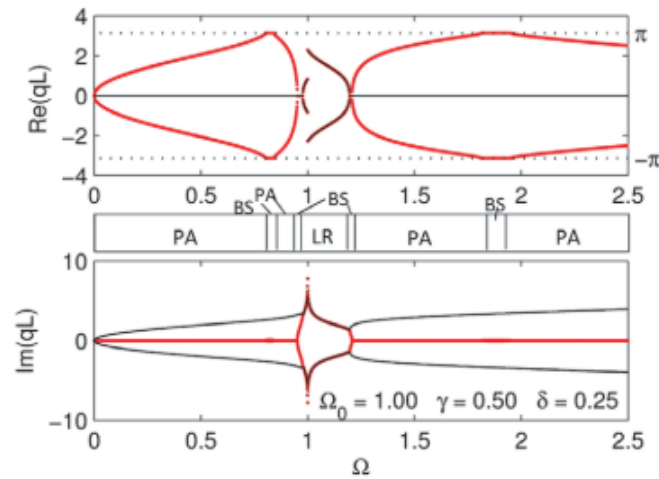
Figure 2.8: Example of more complex behaviour of the eigenvalues, including local resonance [62]

The aforementioned types of bands may occur, in the case of multiple degree of freedoms (MDOF), simultaneously in pairs and thus will lead to a different behaviour of the structure to which we may identify different types. These types are commonly known as [66, 62, 63]:

- Propagation, Attenuation (PA) → one wave is propagated whilst the other is attenuated;

- PP → both waves will propagate, also called double-speed propagation;

- Bragg scattering (BS), or (AA) → both waves decay exponentially and have a phase difference of $n\pi$ from cell to cell, leading to a standing wave. Bragg scatter is ascociated with $k = \frac{n\pi}{L}$, due to which destructive interference occurs [45]. Here, k denotes the wavenumber;

- Local resonance (LR) → two complex waves, 'attributed to the local resonance mechanism due to the presence of the resonators' [62].

The description above is valid only for Euler-Bernoulli and Timoshenko beams, which have

two degrees of freedom (referring to the possible types of motion at the support) and thus two propagation constants. The example shown in Fig. 2.8 also nicely shows the different types of bands, denoted accordingly. Here, one can see that a LR-band occurs in the surrounding of the resonator frequency, denoted with Ω_0.

We have already mentioned that in the case of a continuous periodic structure the ambiguity between wavenumbers is not present in the same manner as is the case for discrete periodic structures. However, the propagation constants are still multivalued which has another very important consequence as mentioned by Mead [32]: instead of one wave there will be infinitely many waves, each having a or wavenumber that differs by an amount of $\frac{2\pi}{L}$ with both negative and positive phase velocities. Depending on the frequency of excitation, certain waves will have more energy than others and thus leading to an overall direction of energy as dictated by the group velocity which will be the same for all waves.

The attentive reader will have noticed already that we have used both the word propagation constant and wavenumber in the previous paragaph, seemingly leading to another ambiguity. An ambiguity that is also very present in the various literature available on periodic continuous structures and often leads to confusion. This is also related with the propagation constant being multivalued and its representation by use of the first Brillouin zone. For a pure discrete periodic structure, indeed all the information regarding the dispersion characteristics are present in the first Brillouin zone. However, as we have mentioned above energy will be distributed along the Brillouin zones depending on the frequency of excitation. With this information, we can assign so called primary waves [32] ascociated with their primary wavenumbers. All the other waves ascociated with that primary wave will be secondary waves. With this, one is able to discern the primary dispersion curves from the secondary ones. For an example of this see Fig. 2.9, where the Brillouin zones have been distincted by use of the vertical dashed line. Regarding the use of the terms, when one considers any of the individual waves that constitute to a Bloch wave, it is appropriate to use the term wavenumber and the correct term depending on the Brillouin zone. When one considers the change in amplitude and phase from one section to another, it is appropriate to use the term propagation constant and it will not matter which value is used. A change in phase by $\lambda_{primary} \pm \frac{2\pi m}{L}$ for any value of m will result in the same phase, after all the structure itself is periodic with $\frac{2\pi}{L}$.

2.2.2 The Transfer Matrix Method

In this section we will show how the Transfer Matrix Method is applied to derive the propagation constants of a periodic structure. Our choice for this method comes down to the fact that it is by far the easiest to apply. Furthermore, one would also be able to derive the Bloch wave functions with this method and by that the Greens function, giving a much easier alternative to the derivation made by Nordborg [50]. The interested reader is therefore referred to Appendix B, where a complete derivation of Greens function is given together with two examples which will lead to a better understanding of Bloch waves and the method of solution for periodic structures. We will also shortly give the reader an introduction to Floquet-Bloch theory, which forms the basis for solving any periodic structure.

The Floquet-Bloch theorem is essentially just an expansion of Floquet theory to three-dimensional spatial systems. Whereas Bloch used it to derive 'the description of the wave function associated with an electron traveling across a periodic crystal lattice' [21, 10]. In its most general form, namely in three spatial dimensions, the general solution may be written as follows [14]:
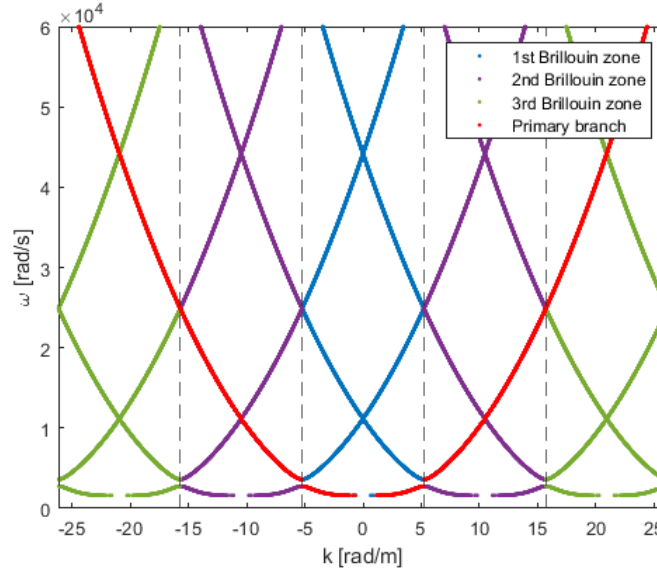
Figure 2.9: Example of the primary branch of the Dispersion curve over several Brillouin zones

$$\Psi(\underline{r}, t) = A(\underline{r})e^{\omega t - a\underline{r}} \quad \text{with: } \underline{r} \text{ the three-dimensional spatial vector} \tag{2.2.4}$$

One may observe the similarities with Floquet theory as treated in Chapter 2.1.1, however now in three spatial dimensions. For our 1D case, Eq. 2.2.4 simplifies to (with the temporal part omitted and a replaced by λ):

$$\Psi(x) = A(x)e^{\lambda x}, \quad \text{with } A(x + L) = A(x) \tag{2.2.5}$$

From which the Bloch B.C., as in the previous section, can be obtained:

$$\Psi(x + L) = e^{\lambda L}\Psi(x) \tag{2.2.6}$$

The Transfer Matrix Method, closely related to the one Mead used (i.e. via the dynamic stiffness matrix), makes use of the transfer matrix. Where the transfer matrix is defined as the relation between the displacements and forces of one end of a cell to the start of the other [7, 63, 6, 15, 65]. The fundamental difference within the derivation of the propagation constants lies in the fact that instead of first solving for the constants of the general solution as would be done for the derivation of a finite element, a relation between those constants at the intersection of two cells is made, which is done by enforcing the boundary conditions at the connection of those, instead of the boundary condition of one cell (with the use of symmetry conditions).

Let us start with the partial differential equation of the Euler-Bernoulli beam governing the displacements of the generic cell in Fig. 2.10:

$$m\ddot{w}(x, t) + EI w''''(x, t) = 0 \tag{2.2.7}$$

Applying a temporal Fourier transform leads to
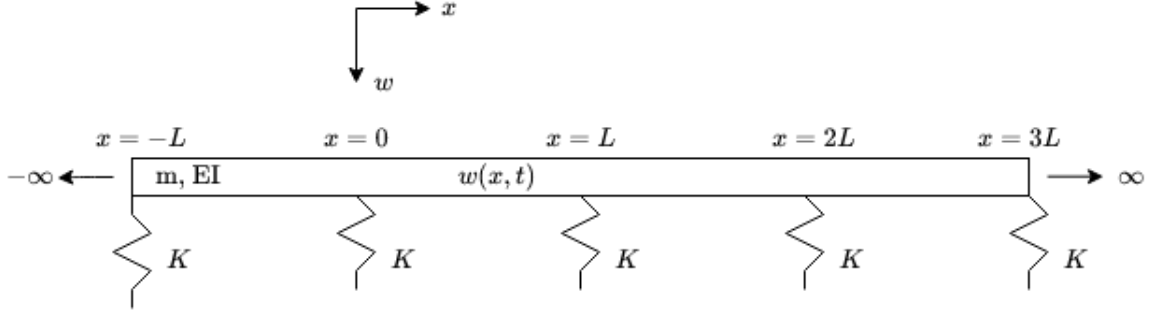
Figure 2.10: Beam on periodic spring supports

$$-\omega^2 m W(x,\omega) + EIW''''(x,\omega) = 0 \rightarrow$$

$$W''''(x,\omega) - k^4 W(x,\omega) = 0 \quad with \ k = \sqrt[4]{\frac{m\omega^2}{EI}}$$

(2.2.8)

where the forward and backward Fourier transforms are defined as:

$$W(x,\omega) = \int_{-\infty}^{\infty} w(x,t)\mathrm{e}^{-\mathrm{i}\omega t} dt$$

$$w(x,t) = \frac{1}{2\pi} \int_{\infty}^{\infty} W(x,\omega)\mathrm{e}^{\mathrm{i}\omega t} d\omega$$

(2.2.9)

The general solution to Eq. 2.2.8 is well known and reads as:

$$W(x,\omega) = A_1 \mathrm{e}^{\mathrm{i}kx} + A_2 \mathrm{e}^{-\mathrm{i}kx} + A_3 \mathrm{e}^{kx} + A_4 \mathrm{e}^{-kx} \qquad (2.2.10)$$

Now, write down the boundary conditions at $x = L$:

$$W_n(L,\omega) = W_{n+1}(0,\omega)$$

$$W_n'(x,\omega)|_{x=L} = W_{n+1}'(x,\omega)|_{x=0}$$

$$W_n''(x,\omega)|_{x=L} = W_{n+1}''(x,\omega)|_{x=0}$$

(2.2.11)

$$EIW_n'''(x,\omega)|_{x=L} + KW_n(L,\omega) = EIW_{n+1}'''(x,\omega)|_{x=0}$$

These boundary conditions may also be written in matrix form as follows:

$$\mathbf{H}\underline{A}_n = \mathbf{K}\underline{A}_{n+1} \qquad (2.2.12)$$

where

$$\mathbf{H} = \begin{bmatrix} \mathrm{e}^{ikL} & \mathrm{e}^{-ikL} & \mathrm{e}^{kL} & \mathrm{e}^{-kL} \\ -\mathrm{i}k\mathrm{e}^{ikL} & \mathrm{i}k\mathrm{e}^{-ikL} & -k\mathrm{e}^{kL} & k\mathrm{e}^{-kL} \\ EIk^2\mathrm{e}^{ikL} & EIk^2\mathrm{e}^{-ikL} & -EIk^2\mathrm{e}^{kL} & -EIk^2\mathrm{e}^{-kL} \\ \mathrm{i}EIk^3\mathrm{e}^{ikL} + K\mathrm{e}^{ikL} & -\mathrm{i}EIk^3\mathrm{e}^{-ikL} + K\mathrm{e}^{-ikL} & -EIk^3\mathrm{e}^{kL} + K\mathrm{e}^{kL} & EIk^3\mathrm{e}^{-kL} + K\mathrm{e}^{-kL} \end{bmatrix}$$

$$(2.2.13)$$

and

$$\mathbf{K} = \begin{bmatrix} 1 & 1 & 1 & 1 \\ -\mathrm{i}k & \mathrm{i}k & -k & k \\ EIk^2 & EIk^2 & -EIk^2 & -EIk^2 \\ \mathrm{i}EIk^3 & -\mathrm{i}EIk^3 & -EIk^3 & EIk^3 \end{bmatrix} \qquad (2.2.14)$$

Eq. 2.2.12 may be rewritten with the use of the Bloch boundary condition $\underline{A}_{n+1} = \mathrm{e}^{\mathrm{i}\lambda L}\underline{A}_n$ (note that we use $\mathrm{i}\lambda L$ now instead of λL):

$$\mathbf{K}^{-1}\mathbf{H}\underline{A}_n = \underline{A}_{n+1} \rightarrow$$

$$\mathbf{K}^{-1}\mathbf{H}\underline{A}_n = \mathrm{e}^{\mathrm{i}\lambda L}\underline{A}_n \rightarrow \qquad (2.2.15)$$

$$\left[\mathbf{T} - \mathrm{e}^{\mathrm{i}\lambda L}\mathbf{I}\right]\underline{A}_n = 0$$

Now, obviously, an eigenvalue problem has been created. The solution thereof are the propagation coefficients. The four propagation coefficients may be found by requiring non-trivial solutions, i.e.:

$$\left|\mathbf{T} - \mathrm{e}^{\mathrm{i}\lambda L}\mathbf{I}\right| = 0 \qquad (2.2.16)$$

As should be apparent from Eq. 2.2.15, the Transfer Matrix method allows us to derive the accompanying eigenvectors. There are four propagation coefficients and thus four eigenvectors, where each eigenvector contains solutions for the constants $\underline{A}$ and thus constitutes to one Bloch wave. The interested reader is referred to Appendix B where one may find a derivation of these Bloch waves and a verification of the Transfer Matrix Method.

2.2.3 Moving loads on periodic structures

In this section we will go over the theory as to derive the response of a periodic structure to a moving (harmonic) load. It is necessary to be able to do so, as the solution method for acquiring the transition curves of oscillators moving on top of a periodic structure actually depends on this response (see chapter 2.2.4). To the authors knowledge there are five distinct methods available.

The first method makes use of the Greens function and has been derived and applied by Nordborg [51, 50]. The second method uses the Floquet transform by applying the Bloch Boundary condition (see Eq. 2.2.3) on a generic cell of the periodic system. This has been derived and applied in several literature. Chebli [17] made based on earlier work by Clouteau [18] a simple derivation concerning the Floquet transform and the response of a periodic system to

a moving load. This was later applied in a follow up paper to a three-dimensional problem [16]. Botshekan [11] applied the Bloch boundary condition on a 1-dimensional periodic beam on supports subjected to a moving load, much like the periodicity condition used by Belotserkovskiy [9], Vesnitskii [60, 59], and Metrikine [43, 42, 41]. Based of the previous mentioned literature by Chebli, Lu [28, 29] made a more elaborate derivation concerning the proper use of the Floquet transform and applied this in two cases. The third method was found in several mathematical papers/theses [46, 4, 8] and is called the Bloch transform. The application of this Bloch transform was done by Lassoued [26]. The fourth method uses the general solution to a periodic structure much like what we did in Chapter 3, which has been applied by Jezequel [23] and Abe [1]. The fifth makes use of Floquet (or Discrete Fourier) transform being applied on the compatibility equations governing the whole model [20].

Although simple and intuitive, the derivation by Chebli [17] does miss a few intermediate steps. Next to that, both his and the derivation by Lu [28, 29] does not include a moving load that varies harmonic in time. Also, the writer was unable to find any proper explanation of the use and origins of the periodicity condition. However, following the Floquet transform one will see the periodicity condition actually arises naturally. Hence, in the following section we will give the elaborate derivation based on the works by Lu [28, 29] for the case of a moving harmonic load. Furthermore, an equivalent but more simple derivation may be found in Appendix C for the interested reader. The Transfer Matrix method is used in Chapters 4, 5, and 6 to calcualate the dispersion curves of several systems.

2.2.3.1 Reponse of a periodic structure to a moving harmonic load using the Floquet transform

Let us first define the forward and inverse Floquet transform as given by Lu [28, 29]:

$$\bar{f}(\kappa) = \sum_{n=-\infty}^{\infty} f(nL)e^{in\kappa L}, \quad f(nL) = \frac{L}{2\pi} \int_{-\pi/L}^{\pi/L} \bar{f}(\kappa)e^{-in\kappa L}d\kappa \tag{2.2.17}$$

From these definitions we can see that the Floquet wavenumber (i.e. κ) really is the result of the discrete spatial function given by nL, which dictates the transfer of information from one cell to the another. This makes sense, as for a periodic structure we have discrete cells (hence the dependency on nL) and within those discrete cells we have a continuous representation of space. Furthermore, we have the convolution of two discrete spatial functions and its corresponding Floquet transform [28]:

$$(f * g)(nL) = \sum_{m=-\infty}^{\infty} f(mL)g([n-m]L)$$
$$(\overline{f * g})(\kappa) = \sum_{n=-\infty}^{\infty} \left\{ \sum_{m=-\infty}^{\infty} f(mL)g([n-m]L) \right\} e^{in\kappa L} = \bar{f}(\kappa)\bar{g}(\kappa) \tag{2.2.18}$$

Having defined our requisites, we start with the response at x to an arbitrary load at x_0 in the frequency domain for an infinite structure [50, 20]:

$$\hat{U}(x_0, \omega) = \int_{-\infty}^{\infty} \hat{F}(x, \omega)\hat{G}(x_0, x, \omega)dx \tag{2.2.19}$$

Here, $\hat{F}(x_0, \omega)$ denotes the temporal Fourier transform (defined by Eq. 2.2.9) of $f(x, t)$, and

$\hat{G}(x_0, x, \omega)$ denotes the temporal Fourier transform of the Green's function $G(x_0, x, t)$. Following Lu [28], we can decompose the variables x_0 and x into $x_0 = x_0^e + mL$ and $x = x^e + nL$, where the superscript e denotes the x-location of an arbitrary cell (varying from 0 to L). Doing so we can also write the integral as an infinite sum of integrals (note that as we have already made a change of variables our integral can be set to 0 to L immediately):

$$\hat{U}(x_0^e + mL, \omega) = \sum_{n=-\infty}^{\infty} \int_0^L \hat{F}(x^e + nL, \omega)\hat{G}(x_0^e + mL, x^e + nL, \omega)dx^e \quad x_0^e, x^e \in [0, L] \quad (2.2.20)$$

Using the following property of the Green's function, which merely says that when we shift the point of excitation by a certain value we get the same response if we would have shifted the point of observation with a same amount but in opposite direction:

$$\hat{G}(x_0^e, x^e + nL, \omega) = \hat{G}(x_0^e - nL, x^e, \omega) \quad (2.2.21)$$

Such that we can rewrite our function as follows:

$$\hat{U}(mL, x_0^e, \omega) = \sum_{n=-\infty}^{\infty} \int_0^L \hat{F}(nL, x^e, \omega)\, \hat{G}([m-n]L, x_0^e, x^e, \omega)\, dx^e \quad (2.2.22)$$

Note that we have written the dependencies on the variables x_0^e, x^e, nL, and mL now in a different manner. Interchanging the order of integration and summation, applying the Floquet transform to both sides and using Eq. 2.2.18 we get:

$$\bar{\hat{U}}(\kappa, x_0^e, \omega) = \int_0^L \bar{\hat{F}}(\kappa, x^e, \omega)\, \bar{\hat{G}}(\kappa, x_0^e, x^e, \omega)\, dx^e, \quad \kappa \in \left[-\frac{\pi}{L}, \frac{\pi}{L}\right] \quad (2.2.23)$$

To be able to continue we first must calculate the Floquet transform of the forcing function. As there exists a relation between the Floquet and Fourier transforms of a function, we can calculate the latter and use the relationship to get our function. The following holds [27, 17, 18]:

$$\bar{f}(\kappa, x^e) = \frac{1}{L} \sum_{m=-\infty}^{\infty} \hat{f}\left(\kappa + \frac{2m\pi}{L}\right) e^{-i(\kappa + \frac{2m\pi}{L})x^e} \quad (2.2.24)$$

Thus, once we have the temporal and spatial Fourier transform we can easily retrieve its Floquet transform. Our forcing function in the time-space domain is as follows:

$$f(x, t, \omega_0) = \delta(x - Vt)e^{i\omega_0 t} \quad (2.2.25)$$

Its temporal Fourier transform is as follows:

$$\hat{F}(x, \omega, \omega_0) = \int_{-\infty}^{\infty} \delta(x - Vt)e^{i\omega_0 t}e^{-i\omega t}dt = \frac{1}{V}e^{-i\frac{\omega - \omega_0}{V}x} \quad (2.2.26)$$

And its spatial Fourier transform:

$$\hat{F}(k, \omega, \omega_0) = \int_{-\infty}^{\infty} \frac{1}{V} e^{-i\frac{\omega-\omega_0}{V}x} e^{ikx} dx = \frac{2\pi}{V} \delta(k - \frac{\omega - \omega_0}{V}) \tag{2.2.27}$$

Using Eq. 2.2.27 in Eq. 2.2.24 we get:

$$\bar{\hat{F}}(\kappa, x^e, \omega, \omega_0) = \frac{2\pi}{VL} \sum_{m=-\infty}^{\infty} \delta\left(\left[\kappa + \frac{2m\pi}{L}\right] - \frac{\omega - \omega_0}{V} \right) e^{-i(\kappa + \frac{2m\pi}{L})x^e} \tag{2.2.28}$$

Now we can insert the Floquet transform of the forcing function into Eq. 2.2.23 and apply the inverse Floquet transform:

$$\hat{U}(nL, x_0^e, \omega) = \frac{L}{2\pi} \int_{-\frac{\pi}{L}}^{\frac{\pi}{L}} \left[\int_0^L \frac{2\pi}{VL} \sum_{m=-\infty}^{\infty} \delta\left(\kappa + \frac{2m\pi}{L} - \frac{\omega - \omega_0}{V} \right) e^{-i(\kappa + \frac{2m\pi}{L})x^e} \bar{\hat{G}}(...) dx^e \right] e^{-in\kappa L} d\kappa \tag{2.2.29}$$

Which can easily be solved due to the presence of the Delta Dirac function, we just have to make sure that the value of κ lies in the integration zone, which can be tuned with the value of m:

$$\hat{U}(nL, x_0^e, \omega, \omega_0) = \frac{1}{V} e^{-in\kappa L} \int_0^L e^{-i\frac{\omega-\omega_0}{V}x^e} \bar{\hat{G}}(\kappa, x_0^e, x^e, \omega) dx^e \tag{2.2.30}$$

Where $\kappa = \frac{\omega-\omega_0}{V} - \frac{2m\pi}{L} \in \left[-\frac{\pi}{L}, \frac{\pi}{L}\right]$. One known to the periodicity condition will recognise it from the exponential in front of the intregal in Eq. 2.2.30 and the definition of κ. A remark has to be made about κ, it contains the value $\frac{2m\pi}{L}$ which was needed to obey the integral from Eq. 2.2.29. However, the Floquet transform is strongly related (if not the same) to the Discrete Time Fourier Transform (DTFT), which happens to be periodic with 2π [22]. Hence, the requirement of $\kappa \in \left[-\frac{\pi}{L}, \frac{\pi}{L}\right]$ seems to be superfluous. Indeed, calculations of the author have shown that one does not need to take into account this requirement.

To obtain the time domain response at any location in the structure one simply applies the inverse temporal Fourier transform on Eq. 2.2.30. We see now that all we need is the Floquet transform of the Greens function of the periodic structure. As we have that one available from Appendix B we could apply the transform and use that solution in the integral. However, that would mean we would have to make a distinction between every frequency as the propagation coefficients also depend on frequency. This would be much too laborious and thus an easier way would be to use the periodic property of the Floquet transform on a generic cell of the structure. The periodic property is as follows [18, 17]:

$$\bar{f}(x + nL, \kappa) = e^{-in\kappa L} \bar{f}(x, \kappa) \tag{2.2.31}$$

The periodicity of the continuous variable in Eq. 2.2.31 merely resembles the correct form of the Bloch Boundary Condition as given by Eq. 2.2.3. Examples of its use are abundant in literature, see for example Belotserkovskiy [9], Metrikine [41], and Botshekan [11]. With the only difference that those applications are not related to the Greens function.

2.2.3.2   The infinite Kinematic Invariants and Anomalous Doppler waves

In case of homogenous infinite structures, there exists a graphical method by which one can find the excited waves due to a moving (harmonic) load or mass [44]. In the latter situation it can also be used to determine the onset of instability induced by the radiation of Anomalous Doppler waves [40, 58]. The kinematic invariant can simply be understood as the equality in phase of the responses of the mass and the beam and it is easily derived by using the condition of permanent contact between the moving mass and the beam [58] and may be written as follows:

$$\omega = \Omega + kV \tag{2.2.32}$$

Intersections between Eq. 2.2.32 and the dispersion curve of a structure give the frequencies and wavenumbers of the excited waves.

Similarly, in the case of periodic discrete structures this method may also be applied. As was done for a 2D periodic discrete lattice by Suiker [55, 54]. However, the periodicity of the lattice does have an effect. Due to the multivalued wavenumber, the kinematic invariant has infinite variants as defined as follows [54]:

$$\omega_m = \Omega + kV + \frac{2\pi m}{L}V, \quad where \; k_i \in [\frac{-\pi}{L}, \frac{\pi}{L}], \quad m = -\infty...\infty \tag{2.2.33}$$

This means that in a periodic structure excited by a moving (harmonic) load there will be infinite waves as determined by the infinite number of intersections due to the infinitely many kinematic invariants. This also means that in a periodic structure, regardless of the cut-off frequency and thus for any velocity, propagating waves will be excited. These will both be normal Doppler and Anomalous Doppler waves and has led to the believe that latter waves will be responsible for parametric instability in a periodic structure [41]. After all, Anomalous Doppler waves will increase the energy of a moving mass whilst normal Doppler waves extract this energy [40]. So far, it has not been proven whether this is also the responsible mechanism for Parametric Instability. During the analysis of Parametric Instability in Chapters 4, 5, and 6 we relate any observations with Anomalous Doppler waves if possible. To that end we use the dispersion curves as derived by means of the Transfer Matrix method (Section 2.2.2).

2.2.4   Parametric Instability of a moving mass / oscillator on a 1-dimensional periodic guideway

In this chapter we will treat the mathematical models that will be used to determine the transition curves (from stability to instability) for either a moving mass and a moving oscillator. The derivation in case of a moving mass has been made by de Oliveira Barbosa and is based on Appendix E (which was added with permission from João de Oliveira Barbosa). As the derivation has not been published, it will be reproduced here. In case of a moving oscillator we will have to derive it ourselves, although similar as the moving mass and loosely based on what was done by Abe [1].

2.2.4.1 Mathematical model for calculating the Parametric Instability of a moving mass

In the case of a moving mass we must determine the interaction between this mass and the beam upon which it travels. Following a similar method as with the Mathieu equation, i.e. using a Fourier series, we can write the motion of the mass as

$$u^m(t) = \sum_{j=-\infty}^{\infty} \tilde{F}_j^m \tilde{h}_j \mathrm{e}^{\mathrm{i}\omega_j t} \tag{2.2.34}$$

where the transfer function of a single mass may be easily derived and thus is given as:

$$\tilde{h}_j = -\frac{1}{M\omega_j^2} \tag{2.2.35}$$

Of course, we can do the same in the case of the beam. As is shown in Appendix E, for each forcing frequency, the periodic structure will have response frequencies at that forcing frequency and others as well. Thus we can write:

$$w^b(t) = \sum_{j=-\infty}^{\infty} \tilde{F}_j^b w_j^b(t, \omega_j) = \sum_{j=-\infty}^{\infty} \tilde{F}_j^b \sum_{k=-\infty}^{\infty} \tilde{u}_{k,j}^b \mathrm{e}^{\mathrm{i}(\omega_j - k\frac{2\pi V}{L})} \tag{2.2.36}$$

Enforcing both compatibility and equilibrium we set their displacements as equal and their forces as equal and opposite:

$$u^m(t) = w^b(t)$$
$$\tilde{F}_j^m = -\tilde{F}_j^b \tag{2.2.37}$$

Using Eqs. 2.2.34, 2.2.36 in Eq. 2.2.37 and dropping the superscript of the force variable gives:

$$\sum_{j=-\infty}^{\infty} \tilde{F}_j \tilde{h}_j \mathrm{e}^{\mathrm{i}\omega_j t} = \sum_{j=-\infty}^{\infty} -\tilde{F}_j \sum_{k=-\infty}^{\infty} \tilde{u}_{k,j}^b \mathrm{e}^{\mathrm{i}(\omega_j - k\frac{2\pi V}{L})} \tag{2.2.38}$$

By using the orthogonality properties of exponential functions, or simply harmonic balancing, we can write an equivalent of Hill's infinite determinant

$$[\mathbf{H} + \mathbf{U}]\,\underline{\tilde{F}} = \underline{0} \tag{2.2.39}$$

where, after truncation of j up to N:

$$\mathbf{H} = \begin{bmatrix} \tilde{h}_{-N} & & \\ & \ddots & \\ & & \tilde{h}_N \end{bmatrix}, \quad \mathbf{U} = \begin{bmatrix} \tilde{u}_{0,-N} & \cdots & \tilde{u}_{2N,N} \\ \vdots & \ddots & \vdots \\ \tilde{u}_{-2N,-N} & \cdots & \tilde{u}_{0,N} \end{bmatrix} \quad \underline{\tilde{F}} = \begin{bmatrix} \tilde{F}_{-N} \\ \vdots \\ \tilde{F}_N \end{bmatrix} \tag{2.2.40}$$

For Eq. 2.2.39 to hold, its determinant must be equal to zero, i.e.:

$$det\,[\mathbf{H} + \mathbf{U}] = 0 \qquad (2.2.41)$$

With Eq. 2.2.41 the values of M satisfying this condition may be found, which will give the transition curves in the $M - V$ space. The fundamental frequencyies of ω_j are defined by either once or twice the passing period of the moving mass, which are defined as $T_1 = L/V$ and $T_2 = 2L/V$, in perfect analogy with the Mathieu equation.

In order to calculate the matrix $\mathbf{U}$ one simply has to calculate the time-domain response of the periodic structure due to a unit moving harmonic load and calculate its Fourier coefficients corresponding to the frequencies present in $\mathbf{U}$.

2.2.4.2 Mathematical model for calculating the Parametric Instability of a moving oscillator
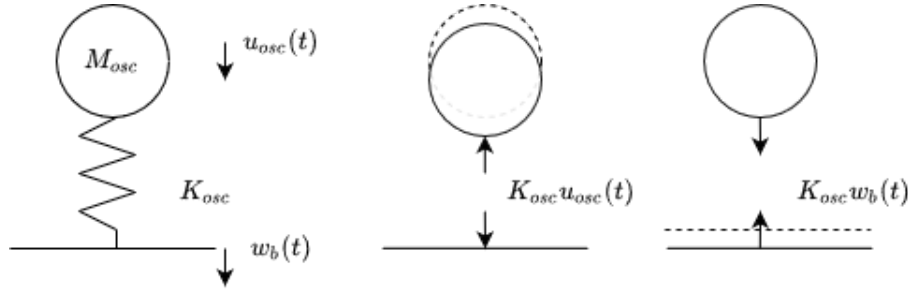
Figure 2.11: Mechanical model moving oscillator

In the case of a moving oscillator inspiration has been taken from Abe [1], therefore the mathematical model changes only a little. Looking at the mechanical model (mass-spring-beam system) in Fig. 2.11, and defining the interaction force in the spring positive in the case of tension, we can write:

$$F(t) = K_{osc}[u_m(t) - w_b(t)] \qquad (2.2.42)$$

If we define the interaction force similarly to the motion of the mass and the rails:

$$F(t) = \sum_{j=-\infty}^{\infty} \tilde{F}_j \mathrm{e}^{\mathrm{i}\omega_j t} \qquad (2.2.43)$$

we can write the motion of the mass as:

$$u^m(t) = \sum_{j=-\infty}^{\infty} -\tilde{F}_j \tilde{h}_j \mathrm{e}^{\mathrm{i}\omega_j t} \qquad (2.2.44)$$

and the motion of the beam as:

$$w^b(t) = \sum_{j=-\infty}^{\infty} \tilde{F}_j \sum_{k=-\infty}^{\infty} \tilde{u}_{k,j}^b \mathrm{e}^{\mathrm{i}(\omega_j - k\frac{2\pi V}{L})} \qquad (2.2.45)$$

Inserting Eqs. 2.2.43, 2.2.44, and 2.2.45 into Eq. 2.2.42 gives:

$$\sum_{j=-\infty}^{\infty} \tilde{F}_j \mathrm{e}^{\mathrm{i}\omega_j t} = K_{osc}[-\sum_{j=-\infty}^{\infty} \tilde{F}_j \tilde{h}_j \mathrm{e}^{\mathrm{i}\omega_j t} - \sum_{j=-\infty}^{\infty} \tilde{F}_j \sum_{k=-\infty}^{\infty} \tilde{u}_{k,j}^b \mathrm{e}^{\mathrm{i}(\omega_j - k\frac{2\pi V}{L})}] \tag{2.2.46}$$

As before, using the orthogonality properties of the exponential functions or simply harmonic balancing we can create an infinite system equivalent to Hill's determinant:

$$\left[\mathbf{I} + K_{osc}\mathbf{H} + K_{osc}\mathbf{U}\right]\underline{\tilde{F}} = \underline{0} \tag{2.2.47}$$

Where $\mathbf{I}$ is the identity matrix and the other matrices are as defined in Eq. 2.2.40. This leaves us with solving the following determinant:

$$det\left[\mathbf{I} + K_{osc}\mathbf{H} + K_{osc}\mathbf{U}\right] = 0 \tag{2.2.48}$$

2.2.4.3 The effect of the constant Fourier series component on the solution method

As we have seen in section Chapter 3, in the case of periodic motion with T_1 we need the constant Fourier series component as well as the fundamental period and its higher harmonics. Whilst the opposite is true for periodic motion with T_2, where we only need the fundamental period and its higher harmonics. In the case of a constant force, the transfer function of the mass will be infinite due to the fact that $\omega_0 = 0$, which physically makes sense since in the transfer function itself no spring is taken into account to oppose any applied constant force. The question that remains is what to do with the transfer function $\mathbf{H}$ within Eq. 2.2.39. The most obvious thing to do would be to completely omit it, the constant force $\tilde{F}_0$ is known after all (i.e. Mg). However the question that follows is whether this would influence the results or not. To answer this question, we shortly revisit the Mathieu equation and investigate what happens when we omit the constant Fourier component.

First of all, in Fig. 2.12 one can see what happens if we omit the constant Fourier component in case of the Mathieu equation. We are now unable to find the boundary emanating from $\delta = 0$, whilst the other boundaries (although only one is shown here) are still valid. As the method of deriving the transition curves in case of a moving mass / oscillator is the same as the one applied for the Mathieu equation we may reason that leaving out a component of the Fourier series will not affect the other transition curves.

However, the question remains whether we will miss an important boundary in the case of the moving mass. For that one must consider the physical meaning behind a negative value of δ. Say we have a parametrically excited pendulum, like the one considered by v. Oostrum [56]. As $\delta = \omega_0^2$, a negative value would simply imply that the pendulum is inverted. In a non-parametric pendulum this position will always be unstable, however one is able to stabilise the motion by exciting it parametrically. Such a physical interpretation is not possible for our moving mass, which can be thought of as an parametric oscillator where the stiffness varies over time. If the squared frequency was to be negative, the opposing force would always have the same sign as the direction of movement and thus would always become unstable. This does not make sense at all for our moving mass and thus we may conclude that omitting the constant Fourier component will not lead to missing a transition curve. Of course, this is due to mere physical reasoning.
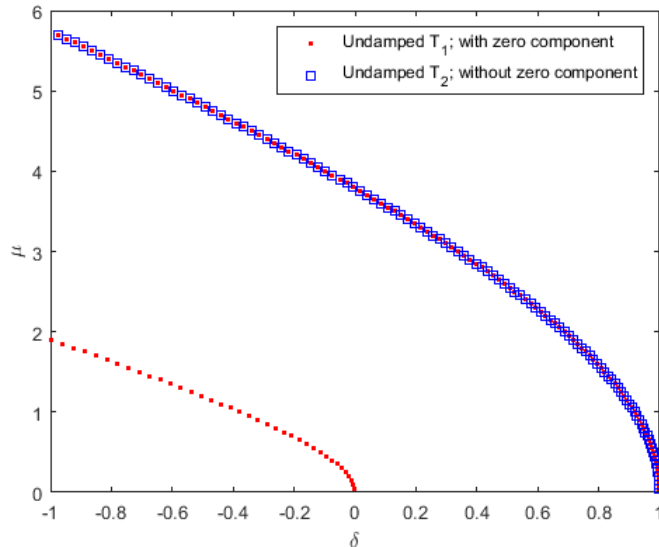
Figure 2.12: Instability Boundaries Mathieu equation

2.2.4.4 Mathematical model for calculating Parametric Instability including a 2-dimensional lattice

Although we have succesfully derived the mathematical model by which we are able to derive the Fourier coefficients of the response due to a moving harmonic load, implementation of this method proved to be rather laborious and time consuming. The method from Chapter 2.2.3 is only able to calculate the full time-domain response of a certain location on the periodic structure. Unsuccesful efforts were made by the author to rewrite them in a moving reference frame. Therefore, to obtain the response directly under a moving harmonic load we would have to calculate the response at many different locations and choose the correct time instants of every single response. The level of accuracy required made it unfeasible to do so and thus this method was abandoned.

The mathematical model created by Barbosa [20] has originally been derived to include a 2D-lattice. Furthermore, Barbosa made a derivation (see Appendix E) which made it possible to directly calculate the Fourier coefficients of the time-domain response under the moving load. He has also written and provided a Matlab script which implemented this method and altered it such that models without a lattice could be calculated as well. Due to the impracticality of the mathematical model mentioned in the previous paragraph, it was chosen to use the model by Barbosa for all calculations regarding Parametric Instability.

Nonetheless, this proved to give problems of its own: calculations including a lattice are extremely slow and a lack of damping will significantly decrease the speed of the calculations as well. The former problem was mainly due to the many calculation steps needed to include the lattice (for more info see [20]), whereas the latter problem was caused by the infinite integration over the frequency spectrum which included singularities. The latter problem could partly be solved by changing the bounds of integration, where the fact that not much energy content was located beyond twice the maximum frequency was used. Furthermore, the standard integration method by Matlab was replaced by the trapezoïdal integration method which was used over equidistant frequencies. An accuracy analysis (see Appendix D) showed that $\Delta \omega = 1$ proved to

be sufficient for most cases.

Chapter 3

Parametric instability of the Mathieu equation

In this chapter we will cover the calculation of Parametric Instability for the Mathieu equation. Firstly, we will derive the boundaries discerning the unstable and stable domains of the Mathieu equation. By that, we are able to find only the location of the boundaries themselves. Secondly, we will derive the Floquet exponents of a whole range of parameters which will give the magnitude of exponential growth (decay) inside (outside) the instability domains. This way we are able to introduce the method of calculation for deriving the transition curves, as a similar method will be applied in the case of a moving mass / oscillator.

3.1 Transition curves of the Mathieu equation

3.1.1 Transition curves of the undamped Mathieu equation

We will start by deriving the transition curves of the undamped Mathieu equation. First we will derive the Hill's infinite determinant and the characteristic equation, wherafter we will numerically solve for the boundaries.

3.1.1.1 Derivation of the characteristic equation for period T_1

To solve the transition curves related to periodic motion with T_1, we will follow section 2.1.3 and apply a complex Fourier series with a fundamental period of $T = 2\pi$ [49]. Using Eq. 2.1.17 and changing its period according to Eq. 2.1.1 leads to the following infinite series:

$$x(t) = \sum_{n=-\infty}^{\infty} C_n \mathrm{e}^{int} \tag{3.1.1}$$

Upon substitution in Eq. 2.1.1 and rewriting the cosine in complex form, the following equation is obtained

$$\frac{d^2}{dt^2} \sum_{n=-\infty}^{\infty} C_n e^{int} + \left(\delta + \mu\left(\frac{e^{it}}{2} + \frac{e^{it}}{2}\right)\right) \sum_{n=-\infty}^{\infty} C_n e^{int} = 0 \tag{3.1.2}$$

which can be rewritten and expanded to:

$$\left(\delta - n^2\right) \sum_{n=-\infty}^{\infty} C_n e^{int} + \frac{\mu}{2} \sum_{n=-\infty}^{\infty} C_n e^{i(n+1)t} + \frac{\mu}{2} \sum_{n=-\infty}^{\infty} C_n e^{i(n-1)t} = 0 \tag{3.1.3}$$

Using the orthogonality property of exponential functions as derived in Appendix A, with respect to the period of vibration of Eq. 3.1.1, leads to:

$$(\delta - n^2)C_n \delta_{mn} + \frac{\mu}{2}(C_n \delta_{m,n+1} + C_n \delta_{m,n-1}) = 0 \tag{3.1.4}$$

In the equation above δ_{mn} denotes the Kronecker delta function. Thus having created an infinite set of coupled linear, algebraic, and homogeneous equations for the Fourier coefficients, we may continue by truncating this up to a certain dimension (i.e. dimension of the matrix: N) and solve the matrix for the non-trivial solution by equating its determinant to zero. This gives the characteristic equation which must be solved to obtain the transition curves. The determinant has the following general form

$$\begin{vmatrix} \ddots & & & \vdots & & \\ & -4+\delta & \frac{\mu}{2} & 0 & 0 & 0 \\ & \frac{\mu}{2} & -1+\delta & \frac{\mu}{2} & 0 & 0 \\ & 0 & \frac{\mu}{2} & \delta & \frac{\mu}{2} & 0 \\ & 0 & 0 & \frac{\mu}{2} & -1+\delta & \frac{\mu}{2} \\ & 0 & 0 & 0 & \frac{\mu}{2} & -4+\delta \\ & & & \vdots & & & \ddots \end{vmatrix} = 0 \tag{3.1.5}$$

where we have only shown the values up to $n = 5$. It is informative to compare this determinant with the ones obtained in [24] by applying the harmonic balance method with a real Fourier series. Upon inspection the following similar determinants are found (Eqs. 3.1.6):

$$a_{\text{even}} : \begin{vmatrix} \delta & \epsilon/2 & 0 & 0 \\ \epsilon & \delta-1 & \epsilon/2 & 0 \\ 0 & \epsilon/2 & \delta-4 & \epsilon/2 & \cdots \\ & & \vdots & \end{vmatrix} = 0$$

$$(3.1.6)$$

$$b_{\text{even}} : \begin{vmatrix} \delta-1 & \epsilon/2 & 0 & 0 \\ \epsilon/2 & \delta-4 & \epsilon/2 & 0 \\ 0 & \epsilon/2 & \delta-9 & \epsilon/2 & \cdots \\ & & \vdots & \end{vmatrix} = 0$$

Apparently, applying the Fourier series with a fundamental period of T_1 that is equavalent to the one as applied in [24] that gives the determinant for the even coefficients. Note that the first

one or two rows in Eqs. 3.1.6 are different from the rows in Eq. 3.1.5. This difference is merely due to the fact that applying the harmonic balance as is done in [24] will give negative values for the cosine and sine function, which may be rewritten due to the properties of those functions (i.e. the former is even and the latter odd). With the application of the complex Fourier series negative frequencies arise only naturally, which leads to the orthogonality properties as derived in Appendix A. Furthermore, the complex Fourier series leads to determinants of which all the curves emanating from their origins may be found, reducing the amount of determinants to be solved for by two (as the same will be the case for periodic motion with T_2, see section 3.1.1.2). It must be noted that this is only in relation with the harmonic balance method and the type of Fourier series used, as Metrikine [41] already only solves 2 determinants.

3.1.1.2 Derivation of the characteristic equation for period T_2

The other transition curve is related to periodic motion with T_2. Thus, a complex Fourier series in the form as Eq. 2.1.17b with the only difference that $T = 4\pi$, is applied:

$$x(t) = \sum_{n=-\infty}^{\infty} C_n e^{i(n-\frac{1}{2})t} \tag{3.1.7}$$

Upon substitution in Eq. 2.1.1, rewriting and expanding as before we get

$$\left(\delta - (n-\frac{1}{2})^2\right) \sum_{n=-\infty}^{\infty} C_n e^{i(n-\frac{1}{2})t} + \frac{\mu}{2} \sum_{n=-\infty}^{\infty} C_n e^{i(n+\frac{1}{2})t} + \frac{\mu}{2} \sum_{n=-\infty}^{\infty} C_n e^{i(n-\frac{3}{2})t} = 0 \tag{3.1.8}$$

which, after applying the orthogonality property with respect to the period of vibration of Eq. 3.1.7, lead to the following infinite set of linear, algebraic equations for the Fourier coefficients:

$$(\delta - (n-\frac{1}{2})^2)C_n \delta_{mn} + \frac{\mu}{2}(C_n \delta_{m,n+1} + C_n \delta_{m,n-1}) \tag{3.1.9}$$

Showing entries of Eq. 3.1.9 up to $N = 6$ gives the following general form of the determinant:

$$\begin{vmatrix} \ddots & & & \vdots & & & \\ -\frac{25}{4}+\delta & \frac{\mu}{2} & 0 & 0 & 0 & 0 \\ \frac{\mu}{2} & -\frac{9}{4}+\delta & \frac{\mu}{2} & 0 & 0 & 0 \\ 0 & \frac{\mu}{2} & -\frac{1}{4}+\delta & \frac{\mu}{2} & 0 & 0 \\ 0 & 0 & \frac{\mu}{2} & -\frac{1}{4}+\delta & \frac{\mu}{2} & 0 \\ 0 & 0 & 0 & \frac{\mu}{2} & -\frac{9}{4}+\delta & \frac{\mu}{2} \\ 0 & 0 & 0 & 0 & \frac{\mu}{2} & -\frac{25}{4}+\delta \\ & & & \vdots & & & \ddots \end{vmatrix} = 0 \tag{3.1.10}$$

Note how we have shown , the reason for this is the fact that in Eq. 3.1.5 also the instability curve emanating from 0 is included, which has only 1 curve and thus leads to an odd dimension [49].

Again, by comparing Eq. 3.1.10 with the ones from [24] leads to the same conclusions as in section 3.1.1.1: however now for the odd coefficients.

3.1.1.3   Solving the characteristic equations

In this section we will present the results from calculating the values of δ corresponding to μ by numerically solving the determinants from the sections above. For both determinants an arbitrary truncation up to $N = 25$ is applied, which will ensure accuracy and convergence of the transition curves within the region of $\mu = 0 \ldots 10$ and $\delta = -1 \ldots 10$. This region has been chosen arbitrarily just to show the applicability of the method.

Generally, one can employ a standard numerical root finder with an arbitrary method (e.g. Newton-Rhapson) to find the roots of any algebraic expression. In the case of the determinant, one will be able to find the characteristic equation algebraically by using e.g. Maple, whereafter one may continue by looping over all the values of μ and plotting the values of δ for which this characteristic equation turns to zero. For this purpose the Newton-Rhapson method is applied.[1]
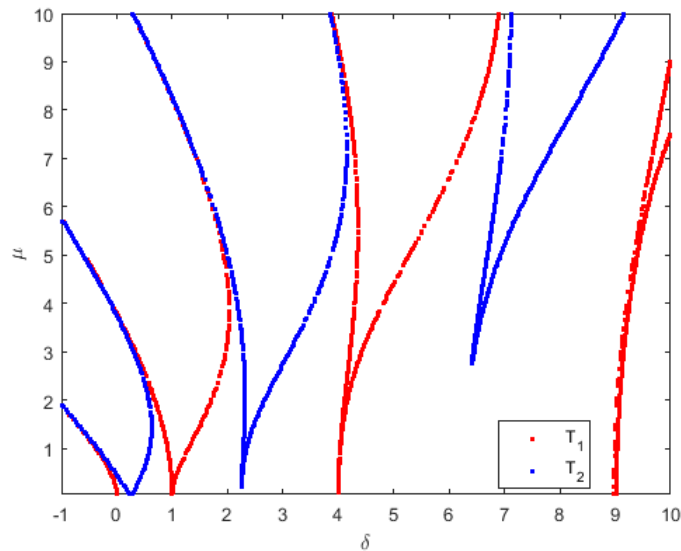
Figure 3.1: Transition curves for the undamped Mathieu equation

The results from the numerical calculations are shown in Fig. 3.1, denoting the type of characteristic equation from which the solutions are obtained. One will see empty spaces in the graph, these account for the instances where the root-finding programme was not able to find all the roots (due to convergence issues). Furthermore, not all the transition curves touch the δ-axis. This can be accounted to the root-finding programme or the truncation of the characteristic equation. Nonetheless, the method is very well able to find all the transition curves. Note that the unstable domains are the ones enclosed by the transition curves.

---

[1]The Newton-Rhapson exhibits quadratic convergence locally but chaos globally [5], and is thus adapted according to the mentioned paper such that it is able to find all roots in a certain range.

3.1.2 Transition curves of the damped Mathieu equation

Since in any physical system a little bit of damping exists, the method would not be complete without including this as well. Therefore the same method is applied, however on a Mathieu equation that includes viscous damping (see Eq. 2.1.8).

3.1.2.1 Derivation of the characteristic equation for periods T_1 and T_2

In the derivations below, most steps have been omitted since they should be clear from the preceding section.

Substituting Eq. 3.1.1 in Eq. 2.1.8, rewriting and applying the orthogonality properties we get the following infinite set of equations:

$$(\delta - n^2 + 2ni\zeta)C_n\delta_{mn} + \frac{\mu}{2}(C_n\delta_{m,n+1} + C_n\delta_{m,n-1}) = 0 \qquad (3.1.11)$$

We proceed similarly for T_2, substituting Eq. 3.1.7 in Eq. 2.1.8 ultimately gives:

$$(\delta + (2n-1)i\zeta - n^2 + n - \frac{1}{4})C_n\delta_{mn} + \frac{\mu}{2}(C_n\delta_{m,n+1} + C_n\delta_{m,n-1}) = 0 \qquad (3.1.12)$$

Finally, Eqs. 3.1.11 and 3.1.12 are truncated up to $N = 25$, whereafter the determinant (not shown here or in the appendix, as the determinant itself is superfluous information) is taken equal to zero such that the characteristic equation is obtained.

3.1.2.2 Solving the characteristic equations

The characteristic equation from the section above will be solved numerically with an arbitrary damping value $\zeta = 0.05$. This leads to the results as shown in fig. 3.2.

As one can see, especially with the help of Fig. 3.3, the instability zones leave the δ-axis and become more narrow, as is confirmed by Nayfeh [49]. We also see that this effect is more pronounced for the higher instability zones, which makes sense considering that the effect of viscous damping increases for higher frequencies.
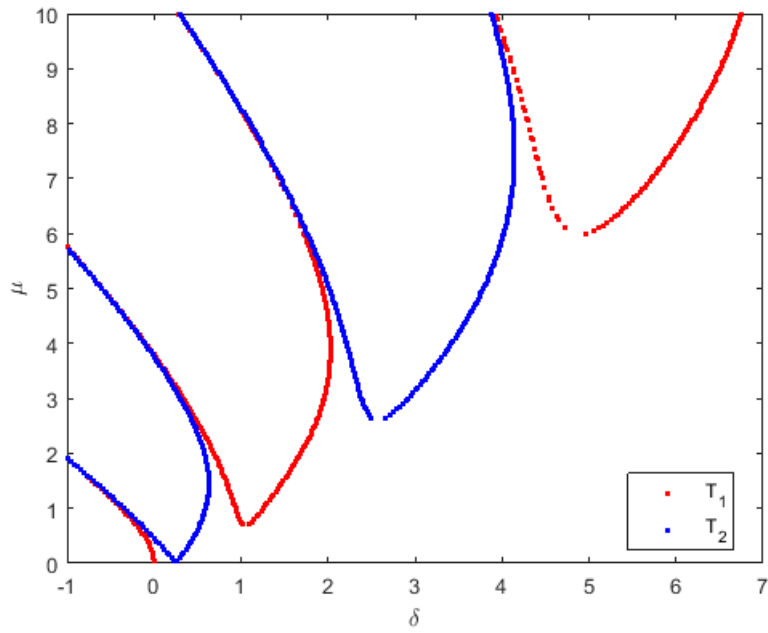
Figure 3.2: Transition curves for the damped Mathieu equation for $\zeta = 0.05$
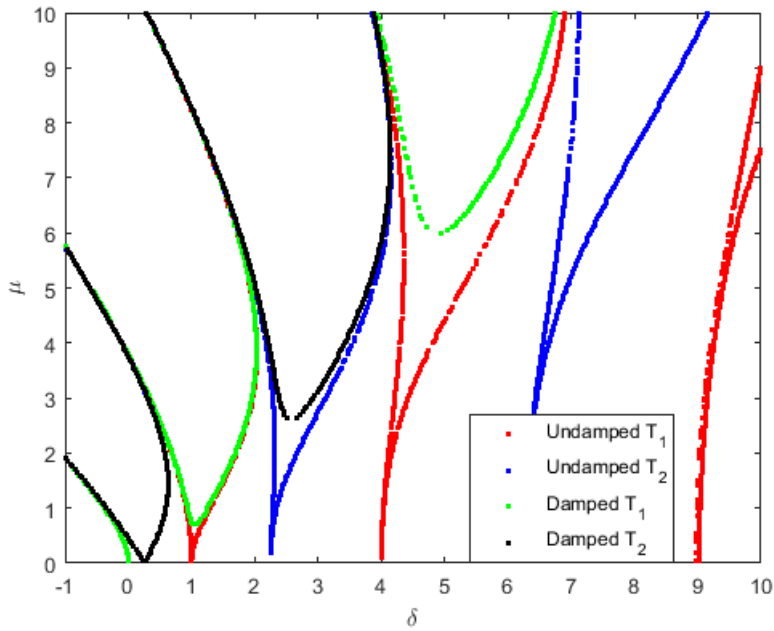
Figure 3.3: Transition curves for the undamped and damped Mathieu equation for $\zeta = 0.05$

It is illustrative to show a comparison between the results from using $\zeta = 0.01$ and $\zeta = 0.05$ as well. As can be seen from Fig. 3.4, a higher damping ratio leads to the instability zones being more narrow and more lifted of the δ-axis. Thus, increasing damping will reduce the parameter space in which instability might occur. The exact effect of damping will be quantified in section 3.2.2.2.
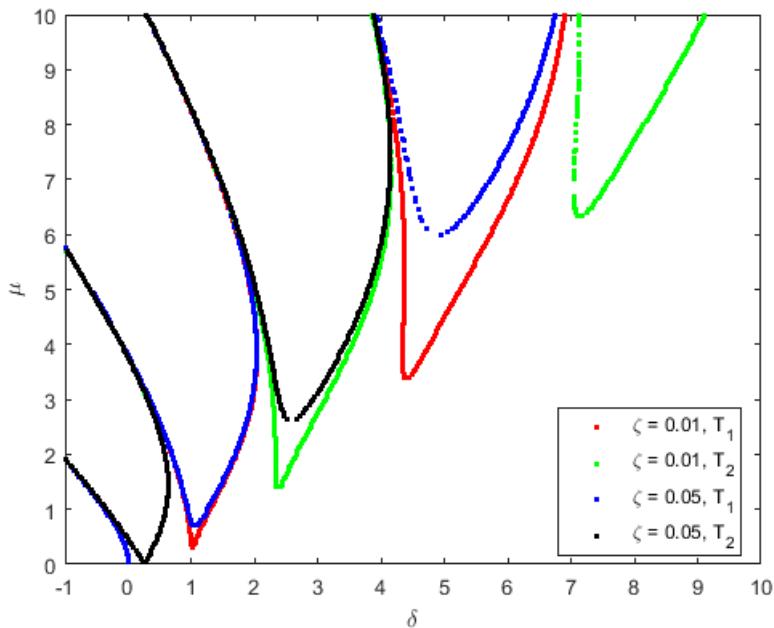
Figure 3.4: Transition curves for the damped Mathieu equation for $\zeta = 0.01, 0.05$

3.2 Floquet exponents of the Mathieu equation

In this section we will calculate the Floquet exponents for the undamped and damped Mathieu equation. In order to calculate these, the general solution from Floquet theory (i.e. Eq. 2.1.3) will be used. Moreover, the method will be checked against the derived transition curves as to confirm the correctness of this approach.

3.2.1 Floquet exponents of the undamped Mathieu equation

As before, we will start by focusing on the undamped Mathieu equation.

3.2.1.1 Derivation of the characteristic equation for periods T_1 and T_2

We start with rewriting Eq. 2.1.3 by applying a complex Fourier series on the periodic function $\phi(t)$ (with period $T = 2\pi$):

$$x(t) = \mathrm{e}^{\lambda t} \sum_{n=-\infty}^{\infty} C_n \mathrm{e}^{int} \tag{3.2.1}$$

Substituting in Eq. 2.1.1 and following similar steps as before ultimately leads to:

$$\left(\lambda^2 + 2\mathrm{i}\lambda n - n^2 + \delta\right) C_n \delta_{mn} + \frac{\mu}{2} \left(C_n \delta_{m,n-1} + C_n \delta_{m,n+1}\right) = 0 \tag{3.2.2}$$

Upon inspection of Eq. 3.2.2 one may recognise Eq. 3.1.4 if λ is taken equal to zero in the former equation. The correspondence is due to the fact that $\phi(t)$ was represented by a Fourier series with fundamental period $T = 2\pi$. It can thus be questioned whether this representation will be able to solve the full equation. However, for periodic motion with T_1, λ must be equal to zero, which transforms Eq. 3.2.2 into Eq. 3.1.4. The same holds for periodic motion with $T_2 = 4\pi$, which is the case for $\lambda = \frac{\mathrm{i}}{2}$, which transforms Eq. 3.2.2 into Eq. 3.1.9. Thus we can conclude that in the end one determinant indeed will be enough.

Solving the determinant as determined by Eq. 3.2.2 will lead to a characteristic equation with λ^n up to $n = 2N$, so there are $2N$ solution for λ. Only two of these are actually necessary for our results, we may find these by realising that the solution of λ are related to each other via [64]:

$$\lambda = \lambda + \frac{2\pi in}{T} \quad \text{for any integer } n \tag{3.2.3}$$

We may see this as well by substituting Eq. 3.2.3 in the general solution Eq. 2.1.3:

$$x(t) = \mathrm{e}^{\lambda t}\phi(t) \rightarrow x(t) = \mathrm{e}^{\lambda t}\phi(t)\mathrm{e}^{\frac{2\pi in}{T}} = \mathrm{e}^{\lambda t}\phi(t + nT) \rightarrow \mathrm{e}^{\lambda t}\phi(t) \tag{3.2.4}$$

Since $\phi(t)$ is periodic with T, shifting with $\frac{2\pi in}{T}$ merely results in the same value. The relation given in Eq. 3.2.3 may be exploited to choose the correct exponents in the numerical calculation.

3.2.1.2 Solving the characteristic equation

In this section two numerical calculations are performed: firstly, the Floquet exponents are calculated by using Eq. 2.1.6 which are then compared with the results from Fig. 3.1, and secondly the exponential growth is quantified by calculating the absolute values of the real part of the Floquet exponents and plotting this. The results for the first item are shown in Fig. 3.5, and the 2nd item in Fig. 3.6.
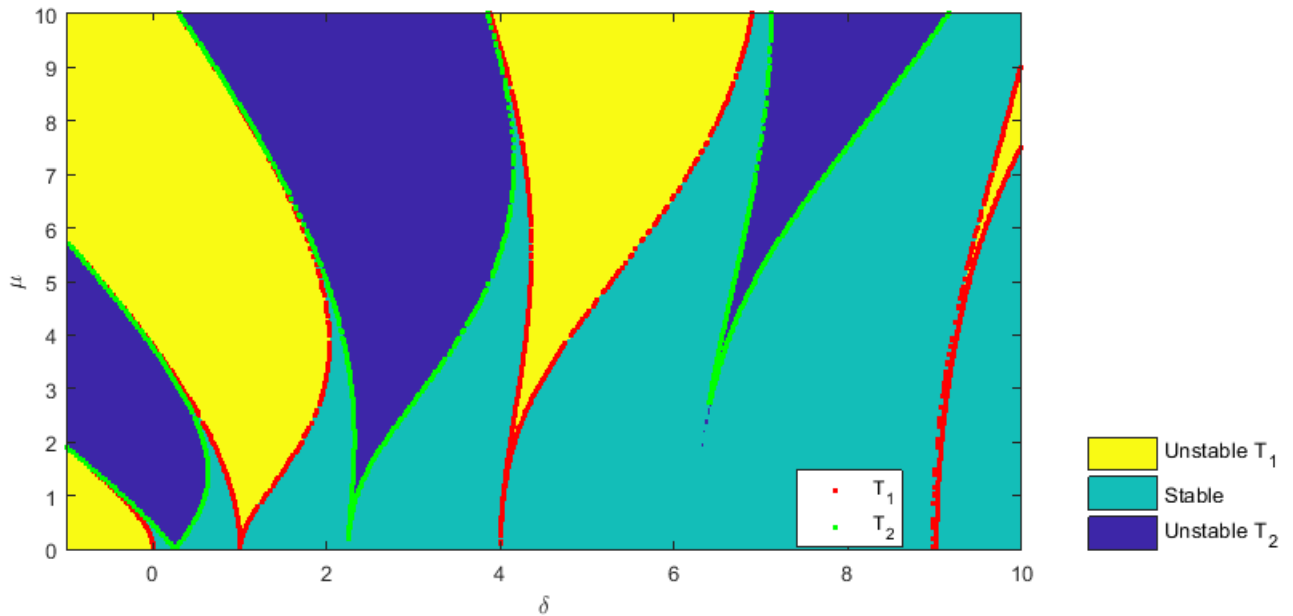
Figure 3.5: Instability and stability plotted with the transition curves

The figure denoting the stable and unstable zones (i.e. Fig 3.5) is graphed such that the regions $|\phi| < 1$ and $|\phi| \geq 1$ are separated. This way, the zones (and transitions) where periodic motion (bounded or unbounded) with either period T_1 or T_2 dominate are recognised. As can be observed these results comply very well with the transition curves calculated in section 3.1.1.3. The higher instability zones emanating from the zero μ axis don't fully 'touch' this axis though, however this is merely a result from the truncation of the value δ: a smaller stepsize would have led to more accurate results. This in contrast with the calculation of the transition curves, where either the root finding programme or the truncation of the determinant led to the same problem.

All the instability zones are clearly shown in Figure 3.6 as well. The same 'error' as mentioned above occurs, the higher instability zones don't fully 'touch' the zero μ axis. We can also see that at the boundaries the real part of the Floquet exponents indeed turn larger than zero, giving instability. Do note that only one of the two exponents is used in the plot, as the other one is the same but of opposite sign. Interesting to see is that regarding the instability, the higher zones are less pronounced.

It is also interesting to see how the imaginary part of λ_1 behaves, as this value dictates the various frequencies occuring in the response. Where a value of 0 constitutes to a periodic solution with T, and a value of 0.5 to one with $2T$.
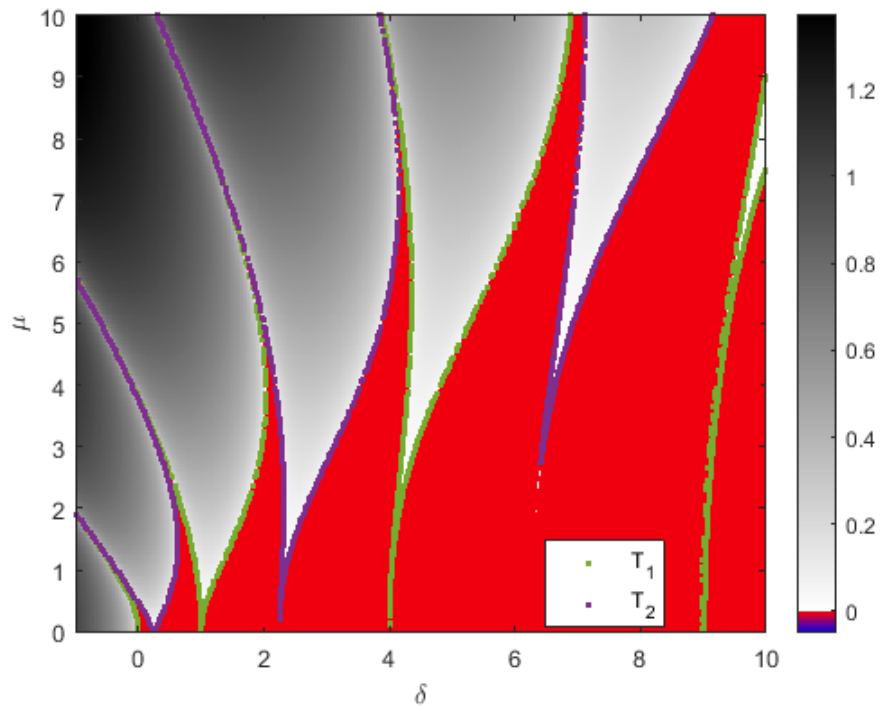
Figure 3.6: Undamped values of $\mathrm{Re}\{\lambda_1\}$ with the transition curves
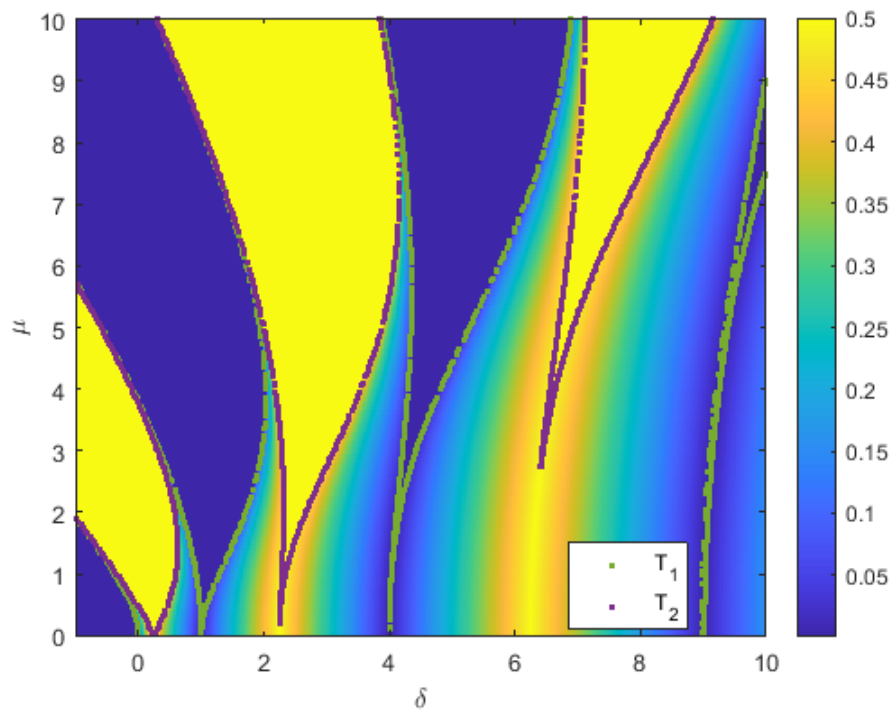
Figure 3.7: Undamped values of $\mathrm{Im}\{\lambda_1\}$ with the transition curves

As can be seen in Fig. 3.7 the values of $\text{Im}\{\lambda_1\}$ attain either 0 or $\frac{1}{2}$ corresponding to the correct instability zones. In the zones with stable motion the values vary between these two ultimates (note that the absolute values have been used, losing information regarding shifting positively or negatively), thus resulting in vibration with different periods.

3.2.2   Floquet exponents of the damped Mathieu equation

3.2.2.1   Derivation of the characteristic equation for periods T_1 and T_2

To derive the characteristic equation, we substitute Eq. 3.2.1 in the damped Mathieu equation (i.e. Eq. 2.1.8) and by following similar steps before we ultimately get:

$$\left(\lambda^2 + 2\mathrm{i}\lambda n - n^2 + 2\zeta\lambda + 2\mathrm{i}\zeta n + \delta\right) C_n \delta_{mn} + \frac{\mu}{2}\left(C_n\delta_{m,n-1} + C_n\delta_{m,n+1}\right) = 0 \qquad (3.2.5)$$

As was the case for the undamped Mathieu equation, more than 2 roots of the characteristic equation will be found. These will have the same relation as defined in Eq. 3.2.3.

3.2.2.2   Solving the characteristic equation

As in section 3.2.1.2, two calculations have been made. The results of the first may be seen in Fig. 3.8 and the second in Fig. 3.9. Note: the calculations have been made using $\zeta = 0.05$.
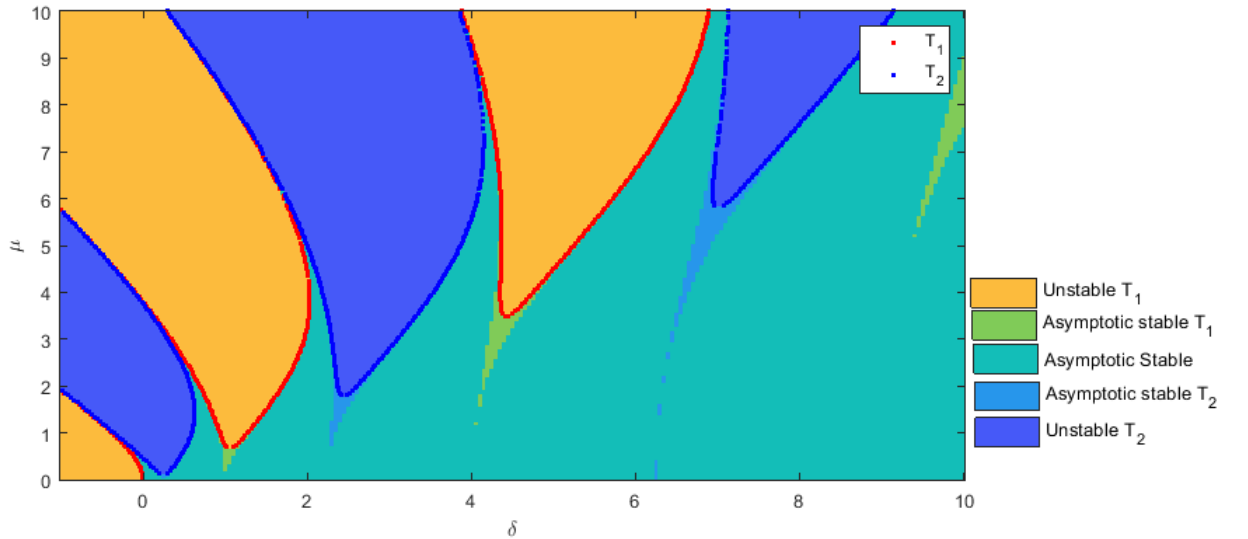
Figure 3.8: Damped instability and stability zones with the transition curves

In Fig. 3.8 the various zones as well as the transition curves are plotted, which agree very well. The new zones where asypmtotic stability with period T_1 or T_2 occurs are observed as well. Thus it may be concluded that the method is able to find the instability zones of the damped Mathieu equation.
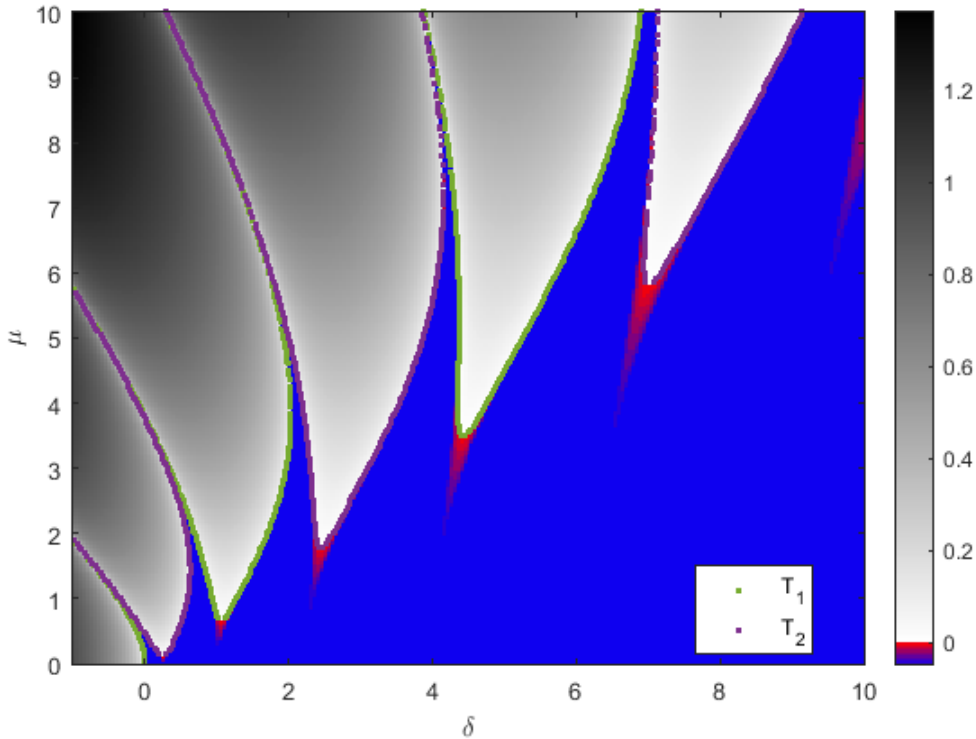
Figure 3.9: Damped values of $\text{Re}\{\lambda_1\}$ with the transition curves

From Fig. 3.8 it is clearly seen that within the instability regions one Floquet exponent is larger than zero, whilst in the stability regions all Floquet exponents are smaller than zero. Note that only one of the two solutions is shown here, as showing the other exponent is not needed since that one does not influence the stability (see Fig. 2.1b why this is the case).

Due to the addition of damping, in all blue regions the motion will die out proportional to $e^{-\zeta t}$. Within the next region (red areas) the absolute values of the real part becomes larger until the transition curve is reached, here one of the real parts of the exponents will be larger than zero and thus lead to instability. If we compare the damped values of $\lambda_{1,2}$ with the undamped ones, there is a consistent (within numerical precision) difference of ζ.

Turning ourselves to the imaginary part of $\lambda_{1,2}$ again, and comparing Fig. 3.10 with Fig. 3.7, we can see that adding damping only influences the real part of $\lambda_{1,2}$. Though this is based on a visual inspection, comparing the numerical values for the damped and undamped case reveal the same.
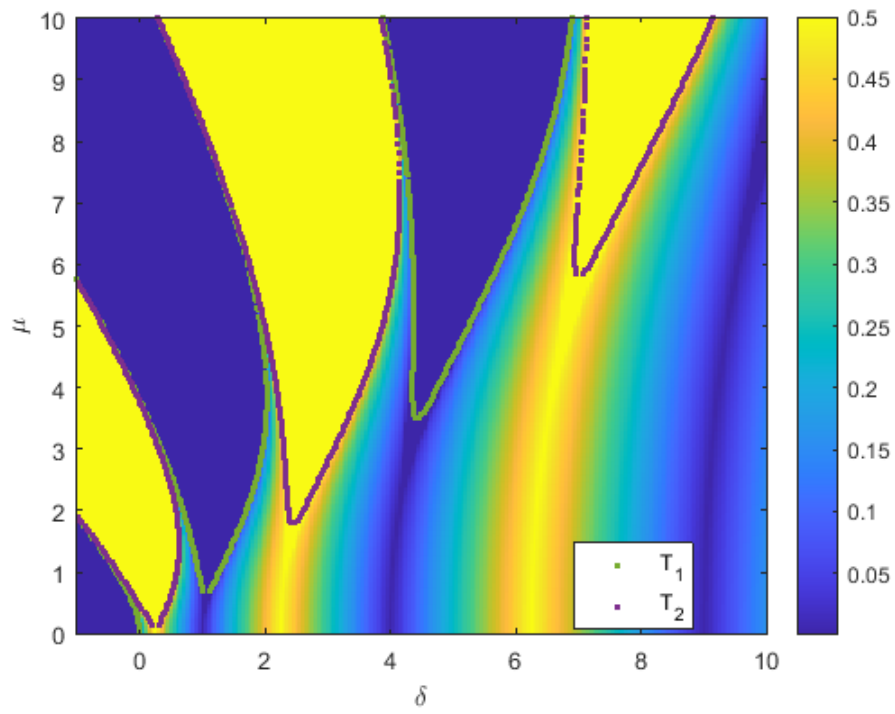
Figure 3.10: Damped values of $\mathrm{Im}\{\lambda_1\}$ with the transition curves

Chapter 4

Parametric Instability of a moving mass / oscillator on a periodically spring supported Euler-Bernoulli beam
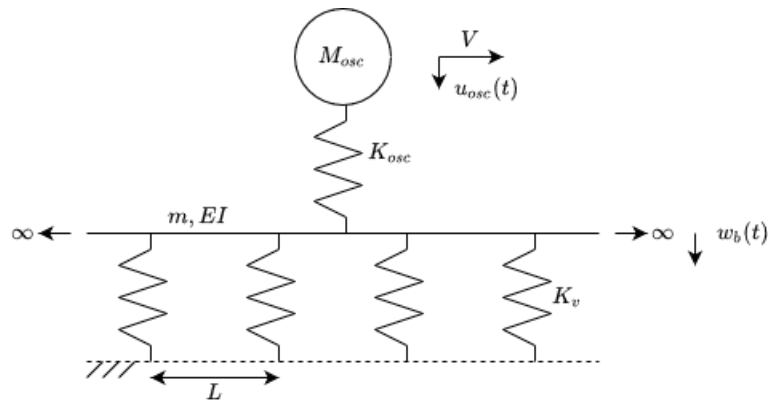
Figure 4.1: Periodic beam on discrete spring supports model

In this section we will treat the periodic beam on discrete spring supports (see Fig. 4.1). First, we will compare the results of our method with previous literature. Furthermore we will perform a parametric analysis based on parameters from literature [51, 20], although altered with various (perhaps unrealistic) values. This is done such that the qualitative differences between parameters are visible. We will also analyse both qualitative and quantitative the instability for the Hyperloop case [1].

---

[1]see also Braak [12] for more information regarding the Hyperloop

4.1   Verification of the method with previous literature

In this section we will verify our method as derived in Section 2.2.4 by comparing with the
results from Oostrum [56]. Note that the method by v. Oostrum [56] was based on a system
with a periodically inhomogeneous continuous foundation, whilst our method is based upon the
use of discrete supports. Nonetheless, such a comparison has been successfully made before by
Abe [1] (whom compared with the results from Verichev [57]) and we will thus use his approach
in order to make the comparison. The variables as used by Oostrum are as follows:

parameter	value
m [kg/m]	60.33
EI [Nm^2]	$6.11 * 10^6$
k_f [N/m^2]	$1 * 10^8$
L [m]	0.6

Table 4.1: Parameters from Oostrum [56]

As the value k_f is the mean foundation stiffness in the continuous model found in [56], we
will now follow [1] by calculating the stiffness of our discrete supports as the mean foundation
stiffness over one period: $K_r = L * k_f = 6 * 10^7$ N/m. Furthermore, no damping of either the
beams or supports is present. Plotting the results from [56] and our method in the same graph
(see Fig. 4.2), we can see a good overall correspondence between the two methods. Note that
the present method allows for directly deriving the boundaries of the instability domains as
opposed to the center line and width of the domains as was done by v. Oostrum [56].
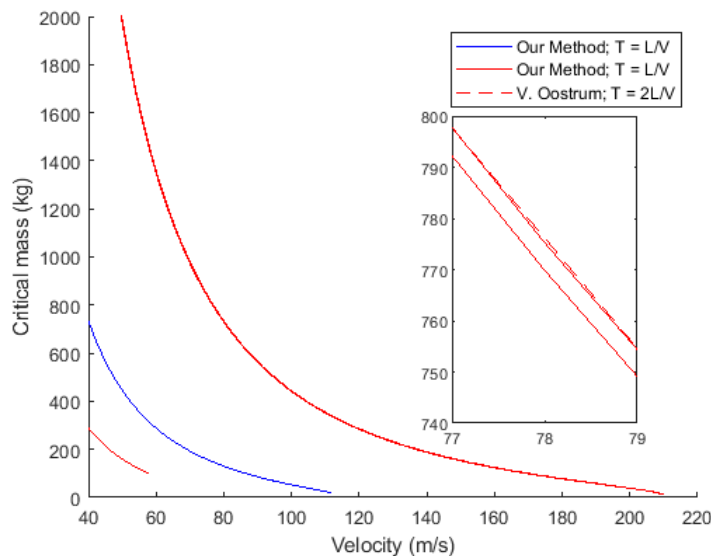
Figure 4.2: Comparison of our method with V. Oostrum [56]

With the approach of v. Oostrum, namely a perturbation method, one is confined to the use
of small values for the periodic stiffness variation of the continuous foundation. The use of a
perturbation method inevitably leads to narrow instability domains, which is an aspect also
shown by our present method that is build upon a model that is discretely supported. The
reason for the similarities may be explained by the periodic inhomogeneity that is introduced by

the discrete supports, which can be expressed by the non-dimensional value α_v. From Appendix F this non-dimensional ratio is defined as follows:

$$\alpha_v = \frac{K_v L^3}{EI} \tag{4.1.1}$$

From Eq. 4.1.1 we can conclude that a high value will correspond to a case where the spring supports are relatively more stiff and thus lead to a greater periodic inhomogeneity. A greater periodic inhomogeneity means that the variation stiffness as felt by the moving mass / oscillator will be greater. In this present case $\alpha_v = 2.12$, which is relatively small (see Section 4.2) and thus the reason for the good correspondence between the two different methods.

We can conclude that the method agrees with the results from previous literature which verifies this method. A more thorough numerical verification will follow in Chapter 7.

4.2 Parametric analysis of the instability

In this section we will perform a parametric analysis of the instability by using some base parameters (as shown in Table 4.2) and varying those as to see what the impacts are on the instability domains.

parameter	base value
m [kg/m]	60.33
EI [Nm^2]	$6.11 * 10^6$
η_r [s]	$1 * 10^{-7}$
K_v [N/m^2]	$5 * 10^8$
η_v [s]	0
L [m]	0.6
K_{osc} [N/m]	∞

Table 4.2: Base parameters spring support

The base parameters are based on V. Oostrom [56] and Verichev [57], albeit with a support stiffness similar to the one used by De Oliveira Barbosa [20]. The reason for this is that otherwise the instability domains would have been too narrow to allow us to qualitatively make any observations. Regarding damping, as the model uses stiffness proportional damping we use parameters similar to what is used by De Oliveira Barbosa [19]. This leads to a ratio of $\eta_i = 0.001s$, here 'i' denotes it can be either damping of the rail ('r') or of the spring ('v'). The combined use of the values mentioned above, might lead to an unrealistic model (with regard to the real world) as we have combined parameters from different literature. However, it suffices perfect to show the impact the parameters might have. Hence throughout the rest of this thesis the sections with a parametric analysis have been kept separately from those representing a real world application.

4.2.1 The effect of the support stiffness on Parametric Instability

We start by analysing the influence of the support stiffness, or rather the ratio of the support stiffness to the beam stiffness without changing the intrinsic properties of the beam. With 'intrinsic' properties we mean the mass, stiffness, and length of one generic cell.
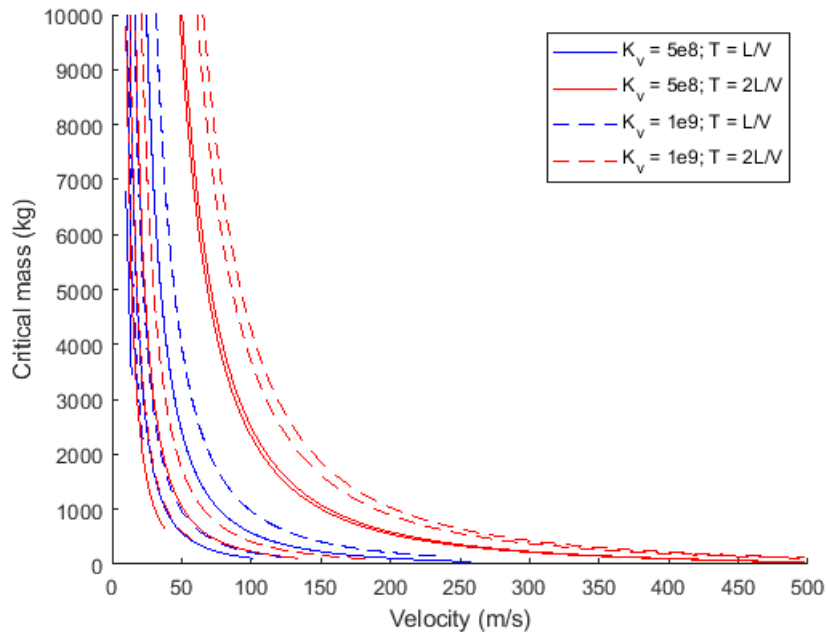
Figure 4.3: Instability domains undamped spring support

As can be seen from Fig. 4.3 by increasing the support stiffness, and thus the ratio of $\alpha_v = 17.7$ to $\alpha_v = 35.5$, the instability zones become both wider and shift to the right. Thus, for an equal value of the mass, the system needs a higher velocity to become unstable. Reasoning physically (and verified numerically in Chapter 7), the velocity is the direct analogy with the value μ in Chapter 3. However, in this case a higher velocity corresponds to a lower value of μ. Whilst traversing the periodic beam at a higher velocity the mass experiences a smaller variation of the stiffness between the beam and the support. Hence by increasing the difference in stiffness, a higher velocity (lower μ) is needed for the system to become unstable. The widening of the instability zones for higher mass and larger value of α_v has been observed before by Vesnitskii [61].

4.2.2 The effect of the support distance on Parametric Instability

Another way of changing the value of α_s is by increasing or decreasing the distance L between supports. This is a change in the intrinsic properties of the periodic beam as well though, hence the positions of the stop- and propagation bands will change.

Looking at Fig. 4.4 we can see that for an increase of support distance the instability zones shift to the right and widen. In the case of a smaller support distance the zones shift to the left and become more narrow. Which is also confirmed by V. Oostrum [56]. The values of α_v are 35.35, 53.13, and 20.45 respectively as according to the graph. Reasoning similarly as in the previous
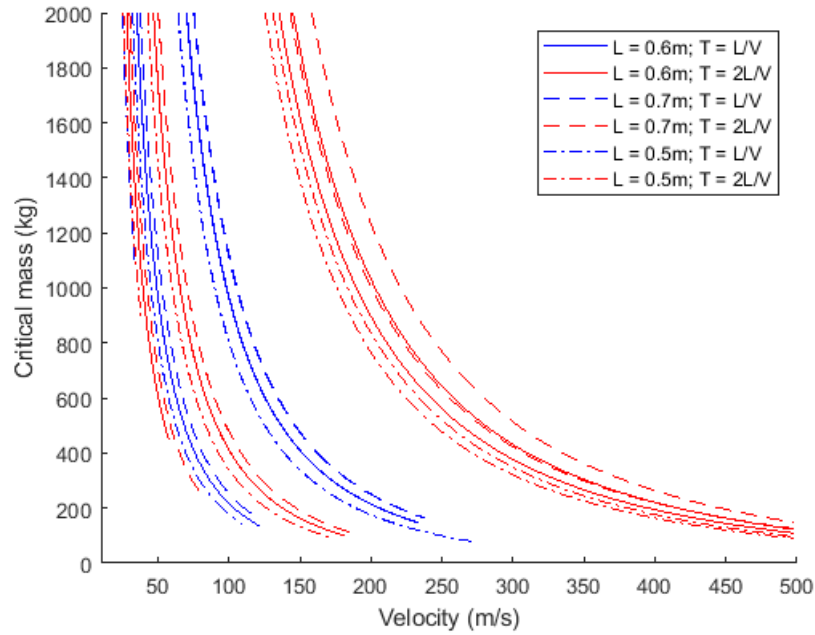
Figure 4.4: Instability domains for $L = 0.5, 0.6, 0.7$ m

section, increasing the support distance will relatively have the same effect as increasing the support distance.

If we compare the widths of the instability domains, we see that for an increased support distance the zones widen as well.

4.2.3   The effect of the beam stiffness on Parametric Instability

The next question is whether decreasing the beam stiffness will have a similar effect as well, hereby we are effectively increasing α_v. For example, if we change the beam stiffness to a value of $6.11 * 10^5$ Nm^2, we will have a value of $\alpha_v = 353$.

From Fig. 4.5 we can see the main instability zone for the latter case has changed significantly, instead of one whole 'tongue' it has opened up and created zones where there is no instability. We will denote these areas as 'islands' of instability.

To explain the origins of the instability islands, the first thing that now should come to mind is the existence of the propagation- and stop-bands for periodic structures, dictating the characteristics for propagating waves. As we have seen in Chapter 2.2.3.2 the waves that are excited are governed by the intersections of the dispersion curve with the kinematic invariants. The first natural frequency defining the boundary between the first stop- and propagation band of the case with $EI = 6.11 * 10^5$ Nm^2 (i.e. $\omega_1 = 2759$ rad/s) is much lower than in the case of $EI = 6.11 * 10^6$ Nm^2 (i.e. $\omega_1 = 5129$ rad/s), see also Fig. 4.6. The existence of propagating waves are dictated by the crossings of the kinematic invariants with the dispersion curve, which is only possible in a propagation band. Therefore, in the former case propagating waves can exist in a lower frequency range. Now, although denoted undamped the model still includes a small amount of viscous damping, which results in higher frequencies being damped more effec-
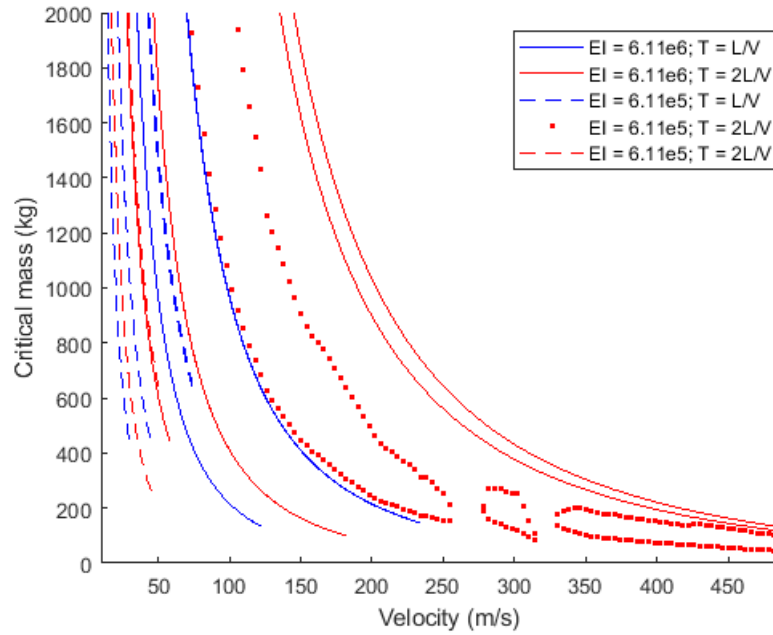
Figure 4.5: Instability domains for $EI = 6.11 * 10^6$ Nm^2 and $6.11 * 10^5$ Nm^2

tively. Due to this, the propagating waves that are present in the former case will be damped less. Now if we assume that the instability itself indeed is caused by the internal battle between Anomalous Doppler waves adding energy to the moving mass / oscillator and normal Doppler waves extracting energy, it makes sense that whenever these types of waves are damped less their invidiual contribution to this battle will increase. Furthermore, the locations of the individual kinematic invariants, as determined by the value $\pm\frac{2\pi m}{L}V$ (see Eq. 2.2.33), may fall within either a propagation- or stop-band leading to more or less propagating waves contributing to this battle. Therefore, a possible explanation of the islands of instability as observed in Fig. 4.5 is that for certain velocities some kinematic invariants that would cause Anomalous Doppler waves whenever in a propagation-band are shifted to a stop-band which leads to a decrease of the energy that contributes to the motion becoming unstable. Whether this is true, remains a question to the author but could be a point of interest for future research.

4.2.4   The effect of damping on Parametric Instability

Of course, in a real structure there is always some sort of damping present. This has been analysed in the case of an infinite string before [41], from which an important conclusion was drawn: increasing the support viscosity "removes the smaller instability zone but widens the main instability zone" [41]. Naturally, we want to check whether this is also the case for an Euler-Bernoulli beam. Therefore four cases will be presented in the next figure (see Fig. 4.7), where we will alter the amount of damping of the rails and the support. Note that the base parameters from Table 4.2 have been used with a support stiffness of $1 * 10^9$ N/m, the reason for this is the complete disappearance of the instability zones in the case where α_v is too low (or rather when the periodic inhomogeneity is too small).
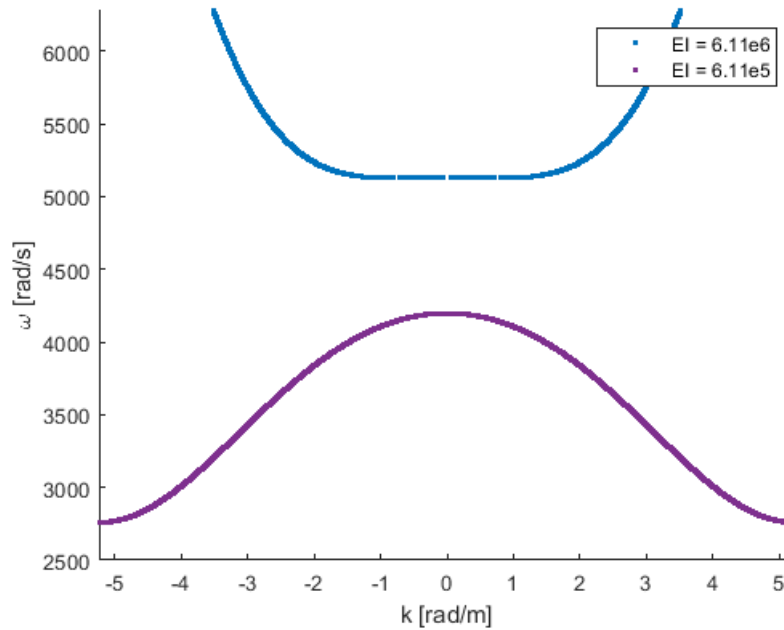
Figure 4.6: Dispersion curves $EI = 6.11 * 10^6$ Nm^2 and $6.11 * 10^5$ Nm^2

As can be seen from the figure, indeed the higher[2] instability zones disappear. However, the first instability zone does not widen, it actually decreases in width and is closed at a lower velocity. Comparing this with the damped Mathieu equation in Chapter 3 we can clearly see the analogy: with increased damping the value of μ (V) must be higher (lower) to be able to induce instability. A possible reason explaining this difference is the fact that although the dynamic stiffness will increase for an increase in frequency (and thus velocity), the frequency (velocity) is just too low in this case to affect the width. As we will see later this is indeed the case.

Important to note here is that although it seems as if the damping of the supports has the greatest effect, we must remember that the damping in our model is stiffness proportional ($C_i = K_i(1 + \mathrm{i}\eta_i\omega)$) and will have a different value for either beam and support.

4.2.5   The effect of an oscillator on Parametric Instability

Now, what changes if we have a moving oscillator as opposed to a moving mass? As the beam can be seen as a spring with its stiffness varying in time and dependent on velocity, adding a spring between the mass and rails just results in them being in series. As a spring in series is always more flexible (lower stiffness) it would make sense that to attain the same periodic motion on the boundaries (either T_1 or T_2) the mass should be lower. That is if one thinks about the eigenfrequency of the moving oscillator, if stiffness goes down, mass should go down as well in order to keep the same eigenfrequency. This is actually the same reasoning as for instability for supercritical velocities [56], but is also confirmed by Metrikine [41]. In the latter paper a simplified derivation considering a 'smeared' model (i.e. discrete support stiffness converted to a continuous foundation) is used to calculate the mass that balances with the period of vibration

---

[2]We will use 'higher' instability zones instead of 'smaller' as was done by Metrikine [41]. This is because of the analogy with the Mathieu equation where we also speak of higher instability zones.
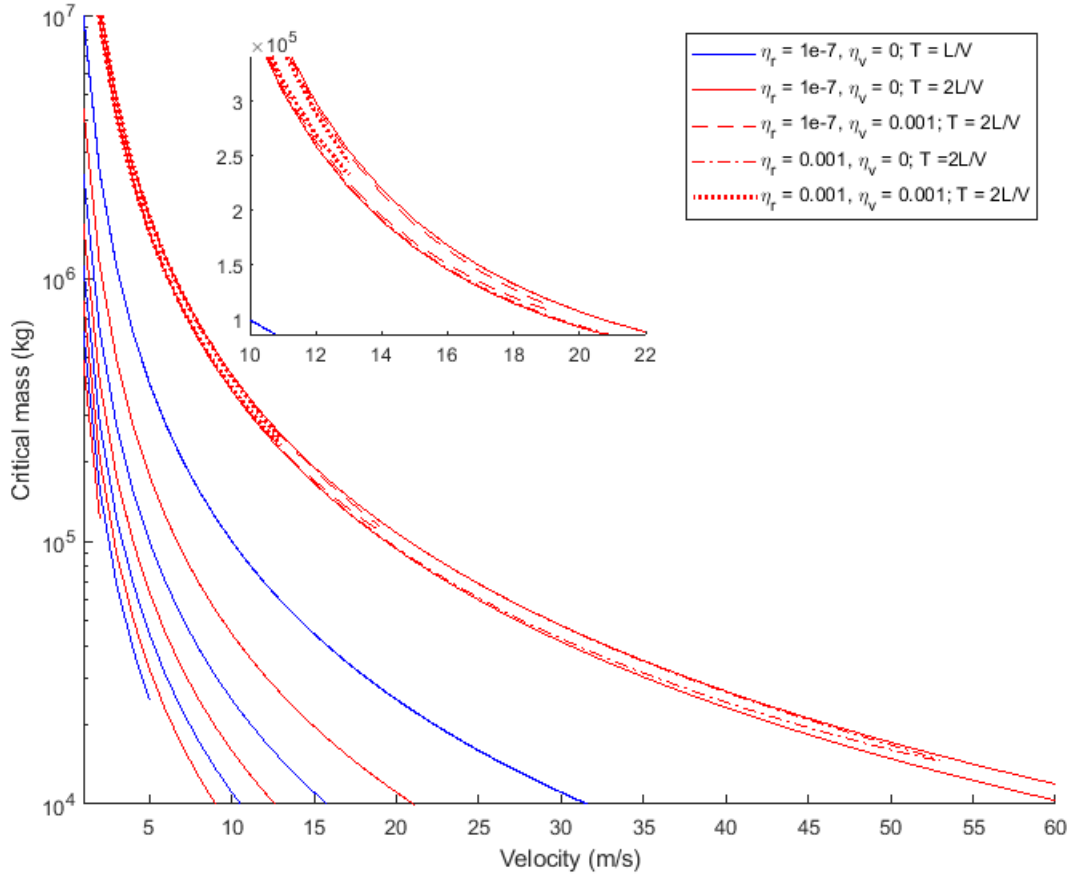
Figure 4.7: Instability domains for various damped cases

related to a certain speed, which shows the same trend as for the semi-analytical version. The reasoning above is confirmed in Fig. 4.8 where two calculations have been shown: for $K_{osc} = \infty$ N/m and $K_{osc} = 1 * 10^8$ N/m. The structure was undamped in this calculation, which explains the occurance of multiple higher instability domains.

Important to note is that, just as is the case for instability in the critical regime, adding a finite spring between the mass and beam merely shifts the instability domain downward. This may be explained by the fact that adding a spring does not change the properties of the structure the oscillator traverses. This may be seen from Fig. 4.9, where for an decreasing value of the spring stiffness the tip of the tongue remains at the same velocity. Note that in this calculation the structure was damped but the oscillator was not. Furthermore, the zones tend to become more narrow for decreasing spring stiffness as well. For which a possible explanation goes as follows: at every crossing of a discrete support energy will be added to the mass, which may cause unstable motion. In the case of an oscillator that energy must spread over both the mass and the spring, hence decreasing the total energy received by the mass. This decrease in energy will then result in a shift of the threshold of energy after which unstable motion may occur, i.e., more input energy is needed to induce unstable motion.
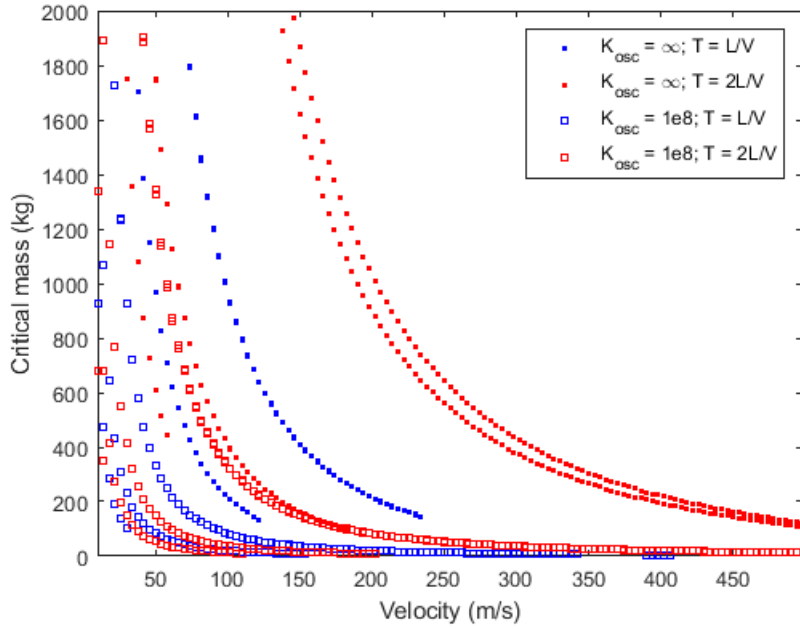
Figure 4.8: Instability domains moving mass and oscillator, undamped
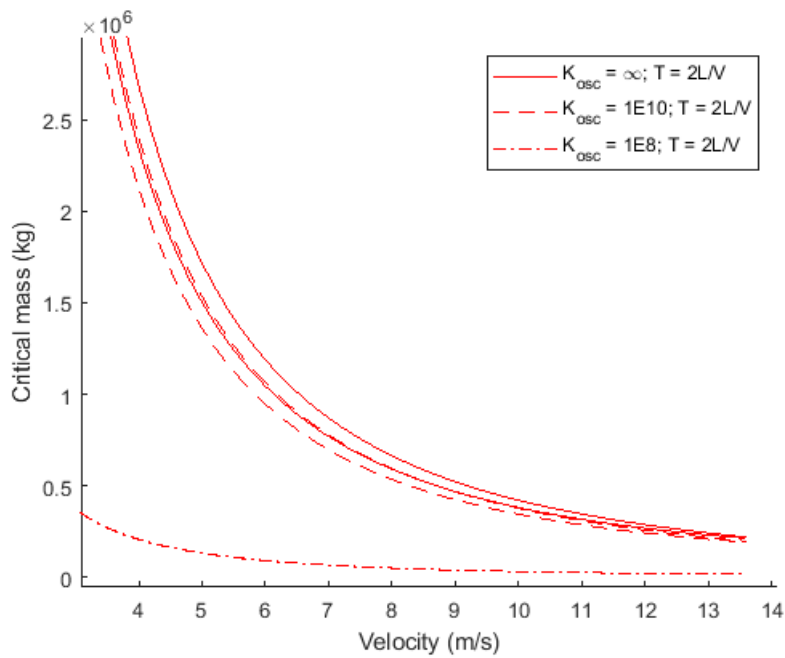
Figure 4.9: Instability domains moving mass and oscillator, damped

4.2.6 The effect of the relative beam-support stiffness on Parametric Instability

As we have seen in the previous sections, the value of α_v and the locations of the stop- and propagation bands have an effect on the instability domains. In Appendix F it is shown that α_v has a pronounced effect on the dynamic characteristics of the periodic system. An increased value will for example increase the cut-off frequency, increase the width of the stop bands and decrease the group velocities of the propagation bands affected. In sections 4.2.1 and 4.2.2 we have seen that increasing this non-dimensional value shifts the instability domains to the right and increases their width. In section 4.2.3 the increase shifts the instability domains leftward, increases their width, and shows the appearance of instability islands. Thus, overall, we can say that an increase in α_v will increase the width of the instability domains. However, the intrinsic properties determining the natural frequencies of the beam are important as well and might lead to other effects. For example, in Fig. 4.10 all values of α_v are equal and the first natural frequencies are $\omega_1 = 5129$, $\omega_1 = 3766$, and $\omega_1 = 1622$ rad/s respectively. The results are obviously different from each other, signifying the importance of the intrinsic properties of the beam.
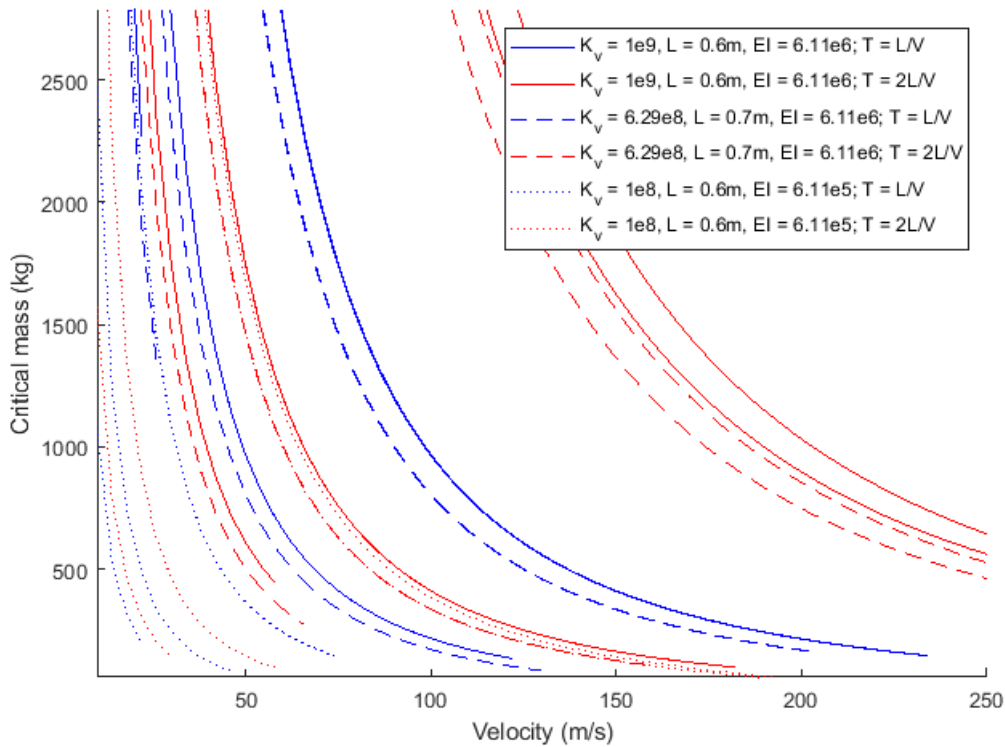
Figure 4.10: Instability domains for similar α_v

4.3 Parametric instability in case of the Hyperloop

Although the aim for this thesis project is related to the parametric instability concerning trains, the hyperloop is an interesting example where parametric instability could also play an

important role. We have already seen that increasing the support distance has a major effect on the instability domain, mainly by significantly increasing the stifness difference between the support and the beam. Which obviously will have an important role regarding the dimensions of such a structure.

Two types of tube systems will be analysed, the first one being a concrete tube which has been studied in a previous thesis by Braak [12]. The parameters of the concrete system will be taken from this thesis. Furthermore a steel tube will be analysed, parameters for this case have been provided by Hardt Hyperloop. The parameters of these two variants may be found in Table 4.3. It must be noted that these calculations are based upon a moving mass, hence the results will not be useful in a realistic case but will provide insight in whether instability might be a problem. To that end, we will also show the results for a realistic case where data of the pod has been provided by Hardt Hyperloop as well.

parameter	steel variant	concrete variant
m [kg/m]	$3.92 * 10^3$	$4.98 * 10^3$
EI [Nm^2]	$6.93 * 10^{10}$	$1.506 * 10^{11}$
η_r [s]	0.001	0.001
K_v [N/m^2]	$3.3 * 10^{10}$	$2.7 * 10^{10}$
η_v [s]	0.001	0.001
L [m]	30	30

Table 4.3: Paremeters for the Hyperloop variant

4.3.1 Effect of using either a steel or concrete tube on Parametric Instability

The results for the undamped case are shown in Fig. 4.11. A stark difference in contrast to the other results is the overal trend of the boundaries, it is full with peaks and throughs. Overall, these are only visible for the first instability domain and are more pronounced for the upper boundary (see the zoomed in part of Fig. 4.11a). Multiple islands of instability are shown as well for both types of tube material, although more pronounced for the steel tube.

(a) Steel tube

(b) Concrete tube
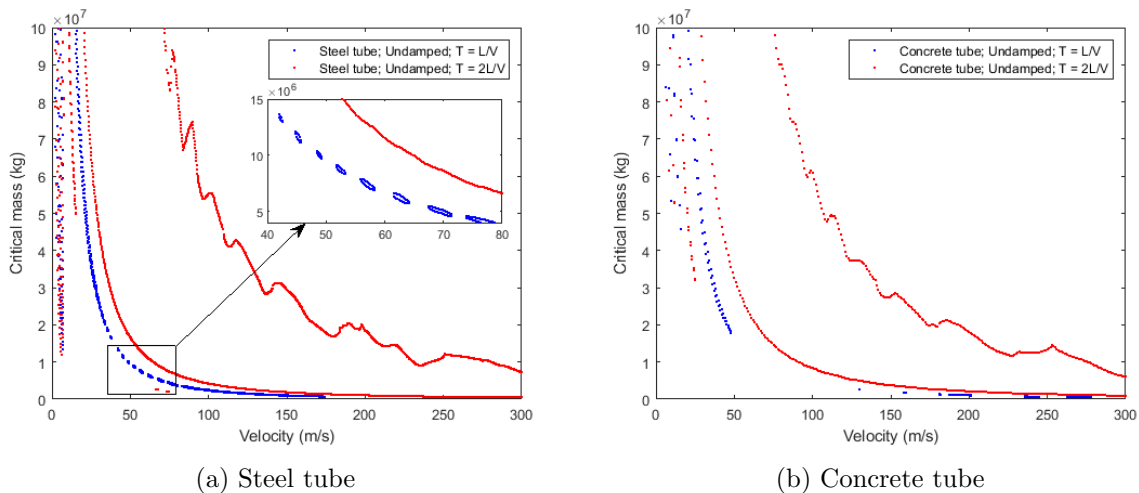
Figure 4.11: Instability domains Hyperloop; Undamped

For the two cases above, the values $\alpha_v = 1.3 * 10^4$, $\alpha_v = 4.8 * 10^3$, $\omega_1 = 46.61$ rad/s, and $\omega_1 = 61.05$ rad/s apply respectively. From which we see a clear difference with the cases we have discussed in Section 4.2. The very low values of the first natural frequencies indicate that already for relatively low frequencies there will be pass-bands in which waves will propagate, which thus will lead to more both normal and Anomalous Doppler waves that contribute to either the extraction or addition of energy to the moving mass. We can also see from the Dispersion curves in Fig. 4.12 that the number of pass- and stop-bands in e.g. $\omega = 0 - 1000$ rad/s as compared to Fig. ?? has increased drastically. If we follow the same reasoning as in Section 4.2.3 we are able to explain the occurence of both the peaks and throughs and instability islands. Once more, whether this is true remains to be proven.
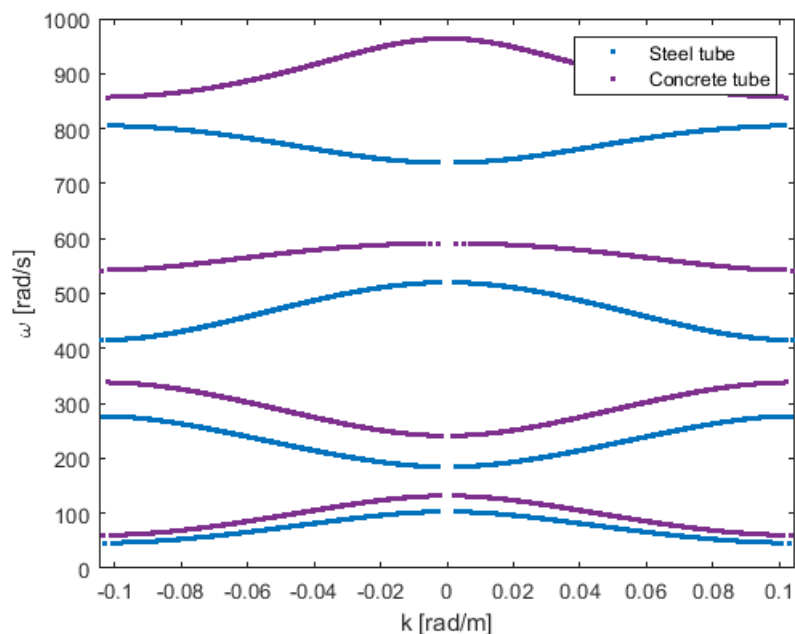
Figure 4.12: Dispersion curves Steel and Concrete Hyperloop tube

In Fig. 4.13 the results are shown for both tube systems which are now damped. The islands of instability have disappeared and the peaks and throughs have been flattened, alternately widening and thinning the main instability zone. In the case of the concrete tube there is still a significant peak shown.

Although the amount of damping might not be realistic, as the value of $\eta = 0.001$ will lead to exceptionally high values of the damping coefficient as well. This does not negate the fact that for a structure similar to a Hyperloop parametric instability will definitely be an important factor. A sidenote to this is the effect of an oscillator, which will lower and narrow the instability zones. An example of this will be shown in the following section.
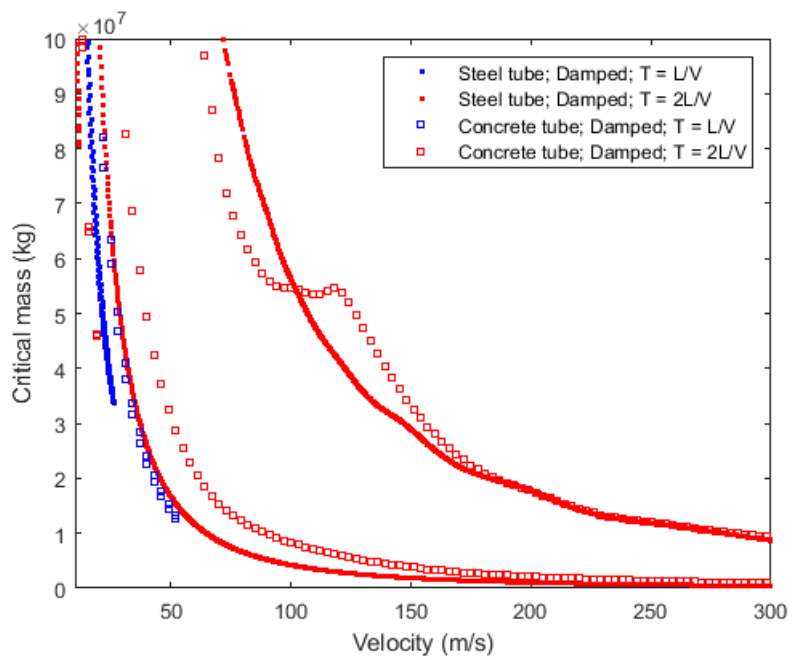
Figure 4.13: Instability domains Steel and Concrete Hyperloop tube; Damped case

4.3.2 Parametric Instability in case of a realistic Hyperloop

As the title says we will treat a realistic case for the Hyperloop. To that end, we have been
provided with the vehicle specifications regarding a small test pod that would be able to move
goods. As these parameters have been provided by Hardt Hyperloop we will not show these.
Although the given parameters include damping for the oscillator spring, this is not included as
the model is not able to incorporate a damped oscillator[3].

As mentioned in the previous section, the amount of damping used in the calculations is a point
of attention. Therefore two calculations have been made: the first will be 'lightly damped' as
the damping value has a value $C_i \approx 1*10^4$, the second we will call 'damped' as it will have the
same amount of damping as the damped case in the previous section (i.e. $C_i \approx 1*10^7$). The
results of the calculations may be found in Figs. 4.14a and 4.14b.

(a) Lightly Damped   (b) Damped
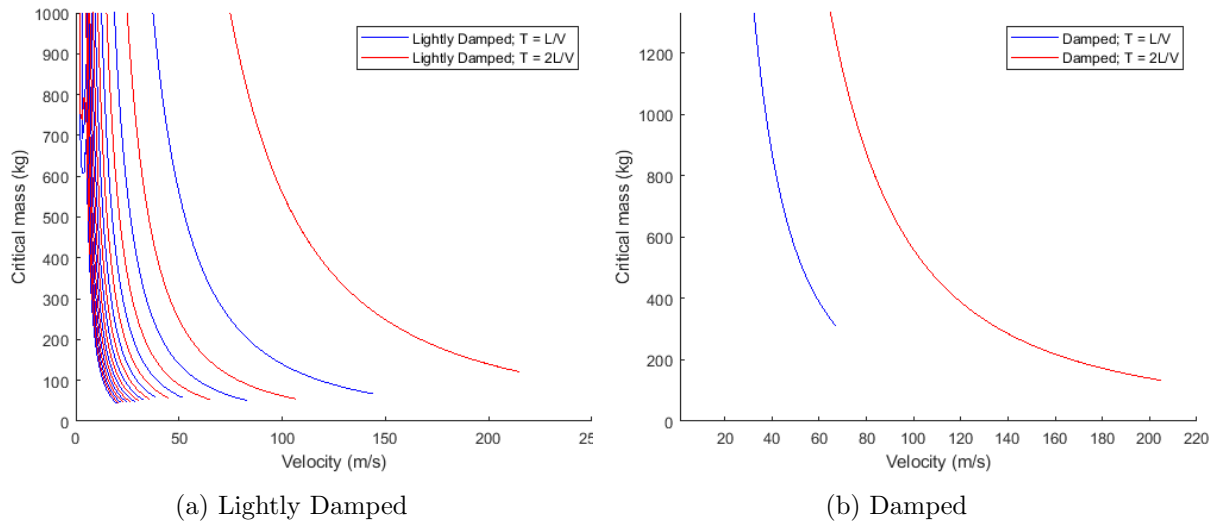
Figure 4.14: Instability domains Hardt Hyperloop Pod

Introducing the total stiffness of the pod has had a significant effect on the instability domains.
We can see that the critical mass values are much lower and the width of the domains have been
reduced dramatically. Although not visible these widths are approximately 0.05 kg in either
case, thus rendering the instability zone practically negligible in the sense that most likely the
instability will not occur in real life. Furthermore the maximum velocity of the instability
domain has been reduced significantly as well, an effect we did not see in our discussion from
Chapter 4.2. We may thus conclude that for extreme differences between the stiffness of the
oscillator and the system itself, the tip of the instability zones will shift leftward as well.

A final remark regarding this 'realistic' case: the vehicle is merely a test pod, not suited for use
of large amounts of goods or people. We can but only expect that for a vehicle that is able to
do so, both the mass and stiffnesses change significantly which will lead to the the instability
zones shifting upward and becoming more wide. That may or may not result in the parametric
instability being important after all.

---

[3]For all we know it might be possible to include damping of the oscillator as well, however this has neither
been tried nor verified.

Chapter 5

Parametric Instability of a moving mass / oscillator on a periodically supported Euler-Bernoulli beam with complex supports

Figure 5.1: Periodic beam on complex support model

In this chapter we will analyse the parametric instability occurring on a periodic beam with complex support, which basically means that we have a movable mass in between two springs (see also Fig. 5.1). As before, we shall first perform a similar parametric analysis as in the previous chapter. Finally we will consider a realistic case of a railroad where the underlying ballast has been modelled as an equivalent spring stiffness, with values taken from [50] and [20].

5.1 Parametric analysis of the instability

In this section we will perform the parametric analysis of the instability by using some base parameters (as shown in Table 5.1) and varying those as to see what the impacts are on the instability domains.

m [kg/m]	60.33
EI [Nm^2]	$6.11 * 10^6$
η_r [s]	$1 * 10^{-7}$
K_v [N/m]	$1 * 10^8$
η_v [s]	0
K_r [N/m]	$42 * 10^6$
η_v [s]	0
M_s [kg]	250
L [m]	0.6
K_{osc} [N/m]	∞

Table 5.1: Base parameters complex support

Note that the base value of K_v has changed to a somewhat lower value, this has been done because the individual effects of the parameters would have been harder to discern in the coming few chapters.

5.1.1 The effect of the stiffnesses of the springs on Parametric Instability

Once more we start the analysis by altering the values of the spring supports. The results can be seen in Fig. 5.2, of which only the boundaries belonging to the T_2 case are shown to avoid unnecessary cluttering of the graph. These results belong to the undamped case. In our discussion the 1st transition curve will correspond to the 1st occurence in the legend of Fig. 5.2, whereas the 2nd boundary will correspond to the 2nd, and so on.

Both the 1st and 3rd boundaries show one island of instability that we have seen before. Increasing support stiffness of either spring has the effect of shifting the boundaries to the right and widening them, similar as what we have observed for the single spring. However, we do see that the lower spring has the most pronounced effect of them. This can be explained by the order of the springs and mass. Imagine a very stiff upper spring, although this increase will certainly be felt, the lower laying mass and spring will still be governing for the total response of the structure (they are in series after all). This observation also explains why the difference between the 1st and 3rd boundaries is smaller than that between the 2nd and 4th: the relative influence of each spring on the equivalent spring stiffness is different. This is confirmed by the dispersion curves in Fig. 5.3 as well, where we can make similar observations.

Overall we see a similar trend of the transition curves as for the model with only a simple spring support, however we also see a change of this trend for certain velocities (see the 1st, 3rd and 4th boundaries). The easiest and most obvious reason for this would be the effect of the mass on the dynamic stiffness, which can easily be investigated as well. To do so, we use the formulation of the equivalent stiffness of the support system as given by Eq. 32 in [1]:
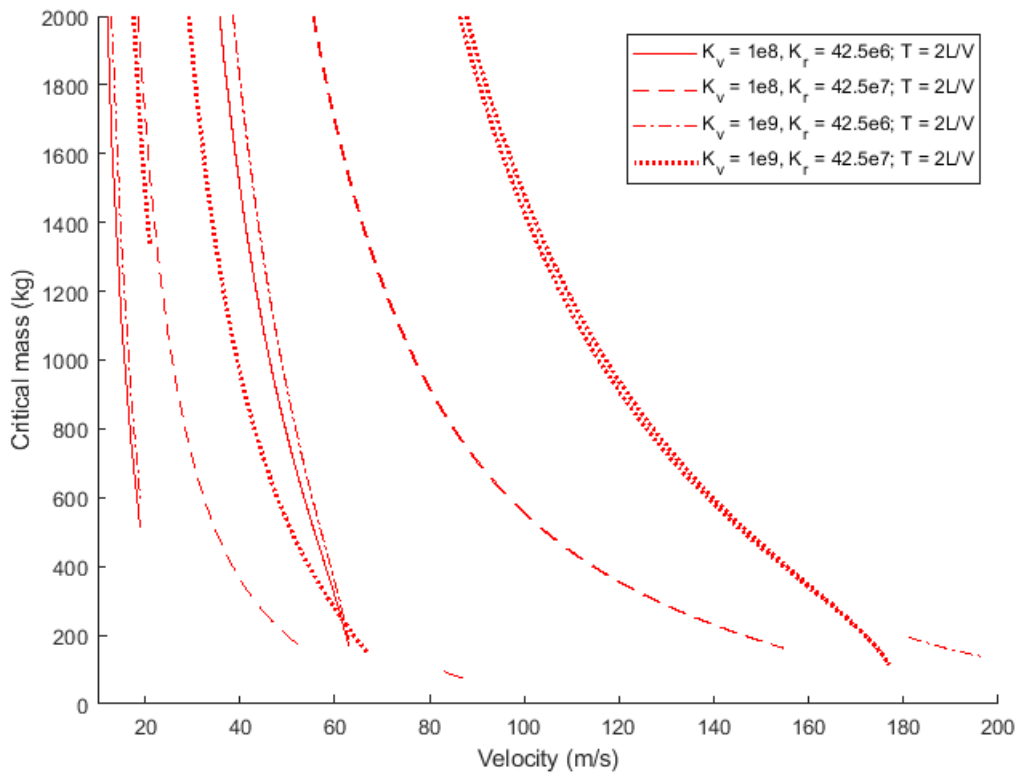
Figure 5.2: Instability domains undamped complex support, varying spring stiffness
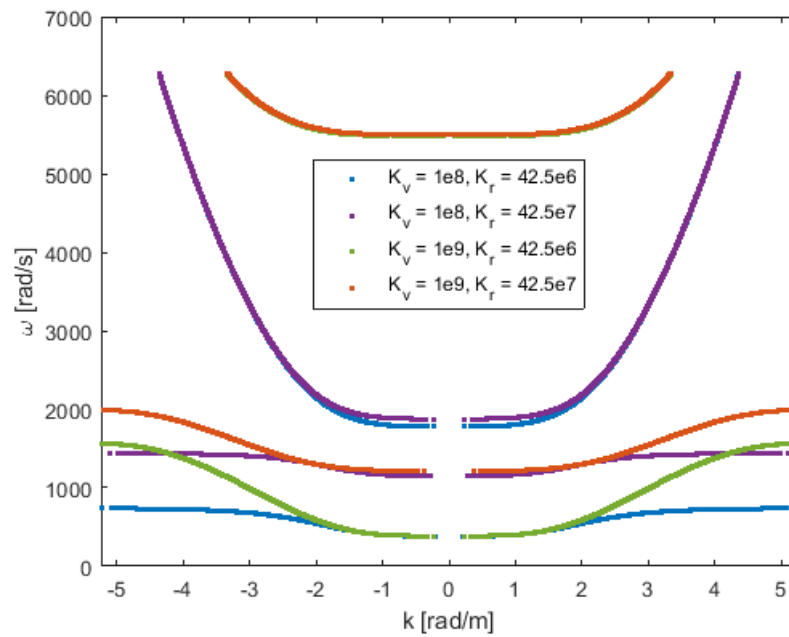
Figure 5.3: normalised equivalent dynamic stiffness

$$K_v = \frac{K_r(K_v - M_s\omega_R^2)}{K_v + K_r - M_s\omega_R^2} \tag{5.1.1}$$

and assuming similarly that the dominant frequency will be given by the resonant frequency as determined by the transition curve: $\omega_R = \frac{\pi V_R}{L}$ [1].
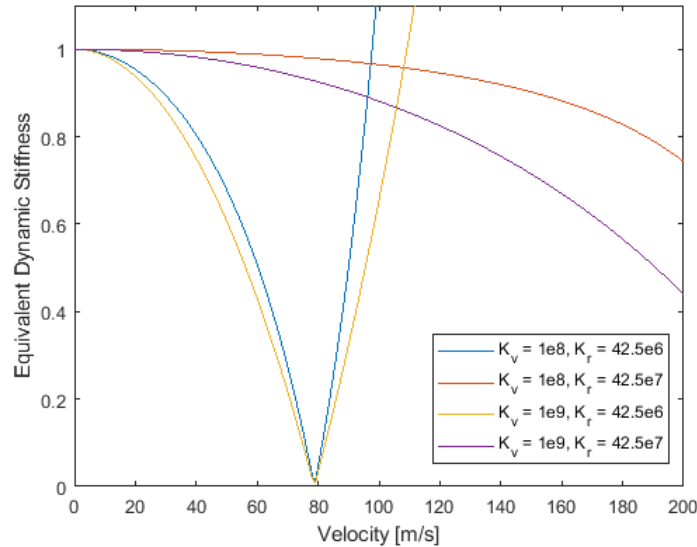
Figure 5.4: normalised equivalent dynamic stiffness

The normalised (w.r.t. the stiffness at zero velocity) equivalent dynamic stiffnesses of all four cases are shown in Fig. 5.4. There we can see that our expectations are met that indeed there is a relation between the dynamic stiffness and the transition curves. The overall trend of the transition curves are affected by the decrease of the dynamic stiffness by inducing a left/downward shift of these curves. We have seen this shift of the transition curves before in Fig. 4.3 in section 4.2.1, however in this case the dynamic stiffness is dependent on frequency (and thus on velocity) such that its effect will increase for increasing velocity.

5.1.2 The effect of the support mass on Parametric Instability

The following parameter that is subjected to a change is the value of the mass of the support, as we have seen in the previous section the dynamic stiffness has a pronounced effect on the transition curves. The results are shown in Fig. 5.5.

For an increased value of the support mass, the transition curves will shift leftward. Furthermore, we see that the downward trend of the boundaries is heavily influenced by the mass. Do note that this influence will also be relative to the stifness of the surrounding springs (as we have seen in the previous section as well). The cause of the change in the trend of the transition curve is easily explained: for a decrease in support stiffness we have seen in sections 4.2.1 and 5.1.1 a left/downward shift of the transition curves. When the support mass is increased it will affect the dynamic stiffness by decreasing its value and thus increase this effect of shifting the transition curves.
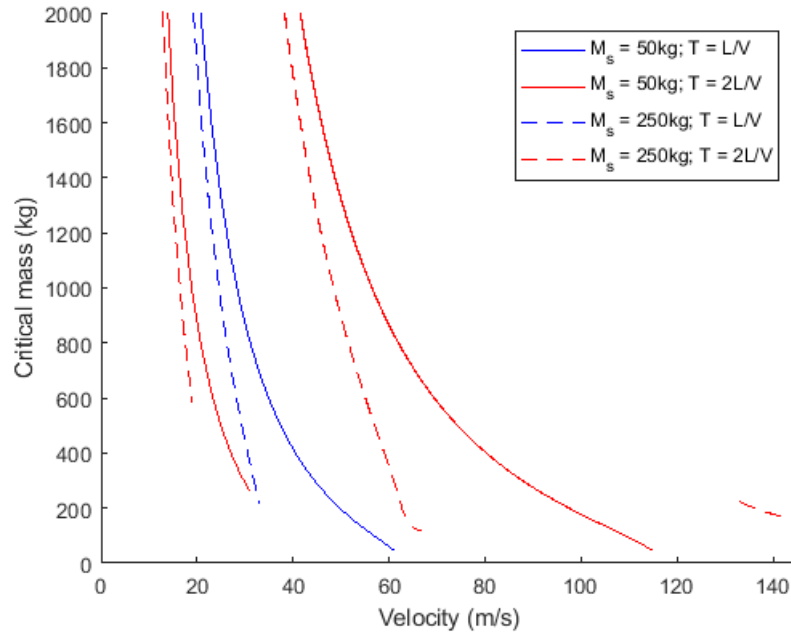
Figure 5.5: Instability domains undamped complex support, varying mass

From Appendix F we know that the natural frequency of the support (it is an oscillator after all) will introduce a LR band (see section 2.2.1) into the dispersion curves. If we were to model a column with its appropriate dynamic stiffness, having infinite natural frequencies, we will thus introduce multiple LR bands. These will thus heavily influence the dispersion curves and the dynamic stiffness of the supports. We can therefore conclude that for complex systems (e.g. the Hyperloop) it is of interest to properly model the complete structure as to incorporate this effect.

5.1.3   The effect of an oscillator on Parametric Instability

Although we have already discussed the difference in results between a moving mass and an oscillator in the previous chapter, we will shortly discuss it here as well due to an interesting result.

Perhaps one can already spot it from Fig. 5.6: for an oscillator several islands of instability appear whilst that was not the case for the moving mass. Whether these are numerical artefacts and therefore wrongly recognised as instability zones cannot be verified as they disappear with the addition of a small amount of damping (which is necessary for numerical stability of such a verification).

5.2   Parametric Instability in case of a regular railway track

In this section we will show the results from an instability analysis for which we have used more realistic values as taken from Nordborg and Barbosa [51, 20]. This is done to be able to assess the importance of parametric instability for railroads. The parameters used may be found in
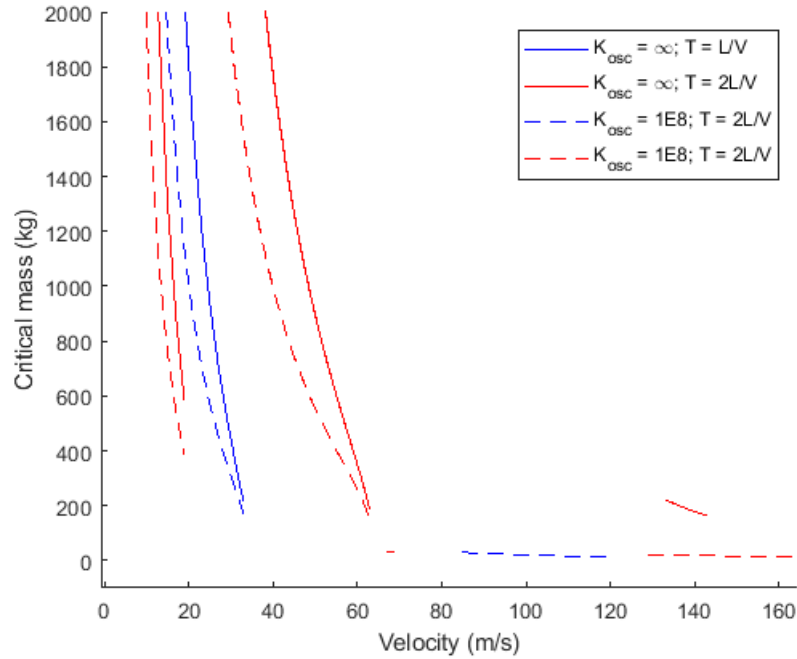
Figure 5.6: Instability domains undamped complex support, Oscillator

Table 5.2.

parameter	base value
m [kg/m]	60.33
EI [Nm^2]	$6.11 * 10^6$
η_r [s]	0.001
K_v [N/m]	$5 * 10^8$
η_v [s]	0.001
K_r [N/m]	$42.5 * 10^6$
η_r [s]	0.001
M_s [kg]	250
L [m]	0.6
K_{osc} [N/m]	∞

Table 5.2: Realistic parameters regular track

Here we introduced more 'realistic' damping in the form of 1% stiffness proportional, which constitutes to the damping values C_i being proportional to $1 * 10^3$ Ns/m, $1 * 10^5$ Ns/m, and $1 * 10^3$ Ns/m respectively speaking (w.r.t. to Table 5.2), which is still far less than the values used by Barbosa [20]. However, the results showed no instability zones! The system simply loses more energy than that can be fed into the motion of the mass.

Although the amount of damping is still a point of discussion and the effect of adding a lattice must still be investigated, it seems that parametric instability for a regular track is not present at all. Of course, to be certain of this one should perform a more rigorous parametric analysis with parameters taken from several real case scenarios.

Chapter 6

Parametric Instability of a periodically supported Euler-Bernoulli beam founded on a 2-D lattice

In this chapter, we will add the ballast layer in the form of a 2D-lattice to the model. First we will analyse the effect of adding the ballast layer as a single waveguide only. To do so, a model without lattice is tuned such that it closely represents the response of the model with lattice for several velocities. Afterwards we will choose parameters corresponding to the complex support from Chapter 5 and add both a ballast and soil layer as to represent a realistic case. Finally we will analyse the case for a slab track which is often used for high-speed railways, which are able to attain speeds of 300-350 km/h ($\approx$ 97 m/s).

6.1   Creating a tuned model for the analysis

In this section we will investigate the effects of adding a 2D lattice to the model. In order to make a comparison valid, we will tune the lower spring of the model with complex support such that it matches the response of the model with lattice excited by a moving load. This will be done for various speeds as to make their correspondence better. The lattice parameters that are used will be similar to those used in [20] and can be found in Table 6.1.

Note that we will only add a ballast layer, and no soil layer yet, as this would obscure the impact of the lattice on the instability zones. We will include no damping such that we get a 'raw' picture without extra energy dissipation not related to any internal mechanisms asociated with the lattice. To keep the analysis simple we restrict ourselves to the speeds related to regular trains in the Netherlands. Therefore we will tune the model to the following speeds: $V = 15, 30, 45$ m/s. Furthermore, the base parameters as given in Table 5.1 apply for both models, although a sleeper mass of 100 kg and upper spring value of $5 * 10^8$ N/m are used. The lower value of the support mass was chosen to decrease the effect it has on the transition curves. Finally, the lower spring in the model with lattice is set to a high value as to ensure that the upper particles move together with the sleeper.

ρ [kg/m^3]	1800
ν [$-$]	0.2
K_{axi}^n [N/m]	$3.03 * 10^7$
K_{axi}^s [N/m]	$5 * 10^8$
η_B [s]	$1 * 10^{-5}$
Width [m]	2
Depth [m]	0.6
Diameter [m]	0.03

Table 6.1: Ballast parameters

The tuning of the lower spring of the model without lattice was done iteratively. First, a calculation of the displacement in case of the model with lattice was made. Second, the static spring stiffness K_r from Table 5.1 was used as starting point, which would iteratively be changed until the mass displacements of both models were satisfactory equal.

(a) Tuning for V = 15 m/s

(b) Tuning for V = 30 m/s

(c) Tuning for V = 45 m/s
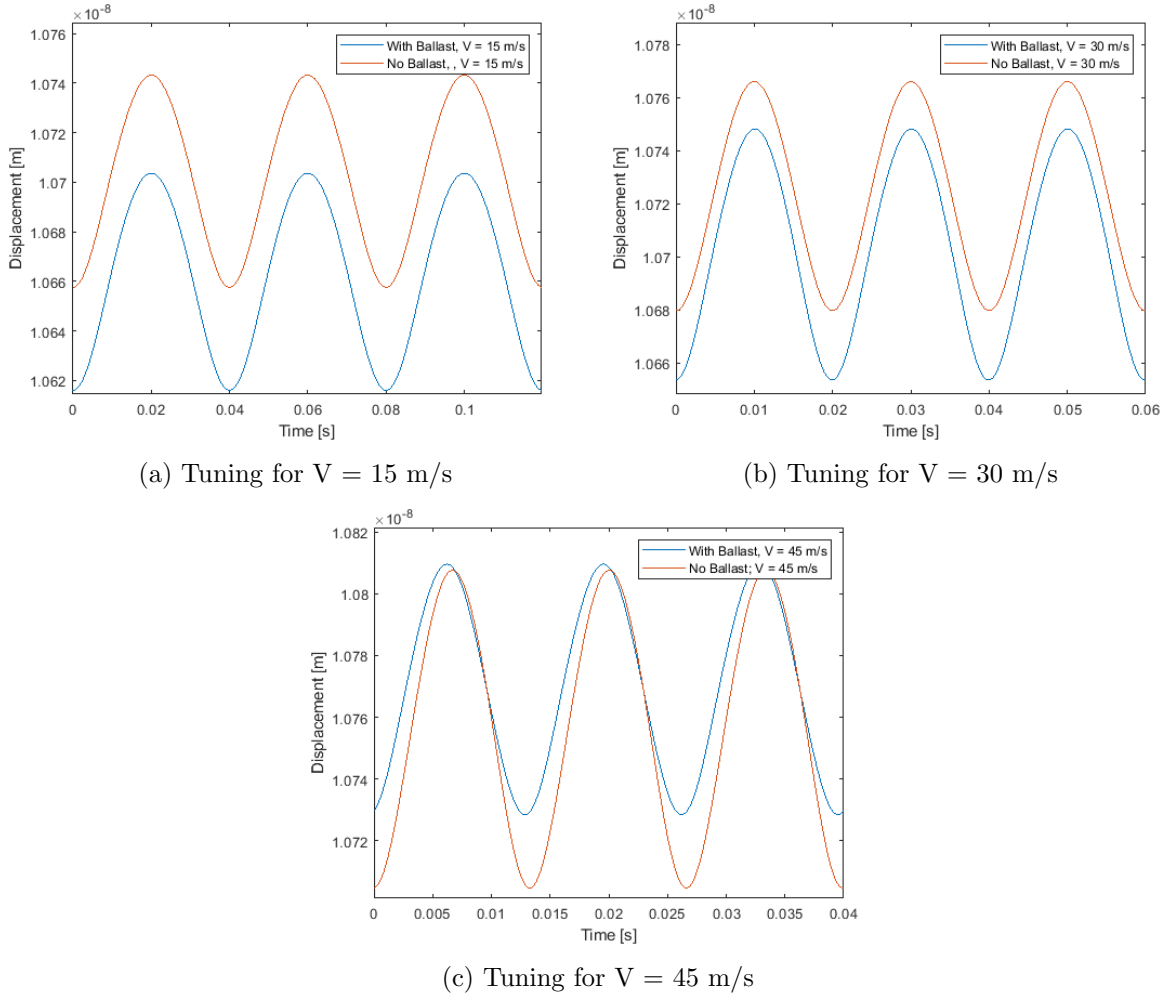
Figure 6.1: Tuning for several speeds

From Figs. 6.1a, 6.1b, and 6.1c we see that regarding order of magnitude the results match very well, although we also can see that for increasing velocity the tuned model tends to behave less

74

stiff. We will neglect these small differences as long as the results from the instability analysis don't show too many discrepancies that cannot be explained. These results are shown in Fig. 6.2.
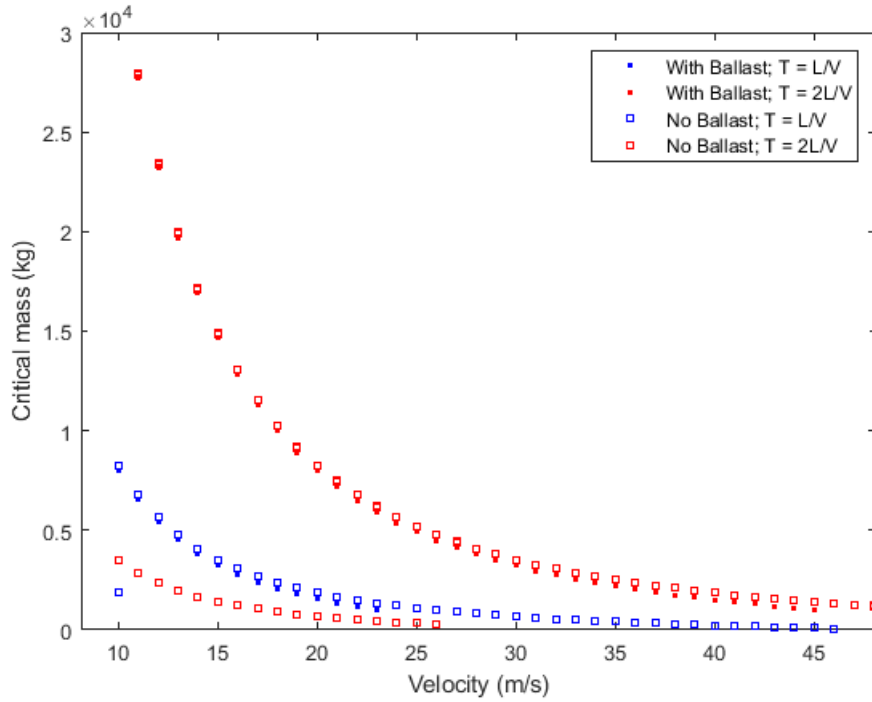
Figure 6.2: Comparison of model with lattice and tuned model

We can see that the model with lattice actually behaves as if damping was added, which can simply be explained by the radiation damping caused by the addition of a lattice. Every time the mass passes a support it will radiate waves into the lattice which of course need energy to be generated, which will be taken from the energy that keeps the motion of the mass constant. The results do show some differences in the values of the critical mass, which are most likely caused by the imperfect tuning and thus may be ignored.

6.2 Parametric Instability of a regular railway track founded on a lattice

In a realistic case both ballast and soil would be present, together with some damping. To realise a realistic case, similar ballast properties as given by Table 6.1 are used. In case of the soil, we will use similar parameters as used in [19]. The most important information regarding the soil parameters are the p-wave and s-wave velocities, these are 242 m/s and 140 m/s respectively.

The calculations showed that for this combination of parameters no instability zones are present at all. This is something we have been expecting because of the result from chapter 5.2 and what what we have seen in the previous section (6.1). The inclusion of both damping and an extra layer where energy may radiate away only decreased the possibility of parametric instability even further.

6.3 Parametric Instability of a high-speed railway slab track

As we have seen in the last section, the inclusion of both ballast and soil layer with damping causes the instability domains to fully disappear for a regular train track. As there also exists high-speed trains which often travel along a slab-track resting on the soil it would be interesting to analyse whether the increased stiffness caused by the slab track itself might lead to instability zones. The parameters used for the slab track are taken from Marolt [30], whilst the soil itself is similar as in the last chapter. Although the slab track from that paper is also founded on another concrete layer, that layer is not taken into account for simplicity of the calculation. See Table 6.2 for the parameters of the slab track. Since there are no sleepers present in a slab track, the calculation model is changed such that the rails are connected with the lattice via one spring only.

E [GPa]	36
ν [$-$]	0.2
ρ [kg/m^3]	2300
$K_{\mathrm{axi}}^{\mathrm{n}}$ [N/m]	$2.75 * 10^{10}$
$K_{\mathrm{axi}}^{\mathrm{s}}$ [N/m]	$2.5 * 10^{9}$
η_{B} [s]	$1 * 10^{-4}$
Width [m]	2
Depth [m]	0.2

Table 6.2: Slab track parameters

Subsequently two types of models were used: in the first we consider an infinite layer of soil and in the second we use similar soil parameters as in the last section. On top of that, for each type of model we perform both an undamped and damped calculation. The values of damping are either similar to those in previous sections or equal to the values in the mentioned papers. The reason to include a model with infinite soil is based on the suggestion that coupling of the supports in this model might influence the results. This mechanism is described as follows: with the crossing of each support, energy will be radiated within the lattice. When this energy, in the form of waves, reaches the next support it might add to the total energy of the moving mass. By which instability might be induced as well. Now, in the first model this mechanism is less

likely to happen due to the fact that waves will not reflect within the soil layer. Overall, less energy should be able to reach the next support. Of course, Rayleigh waves may still be present in both cases, contributing to the transfer of energy from one support to the next as well.
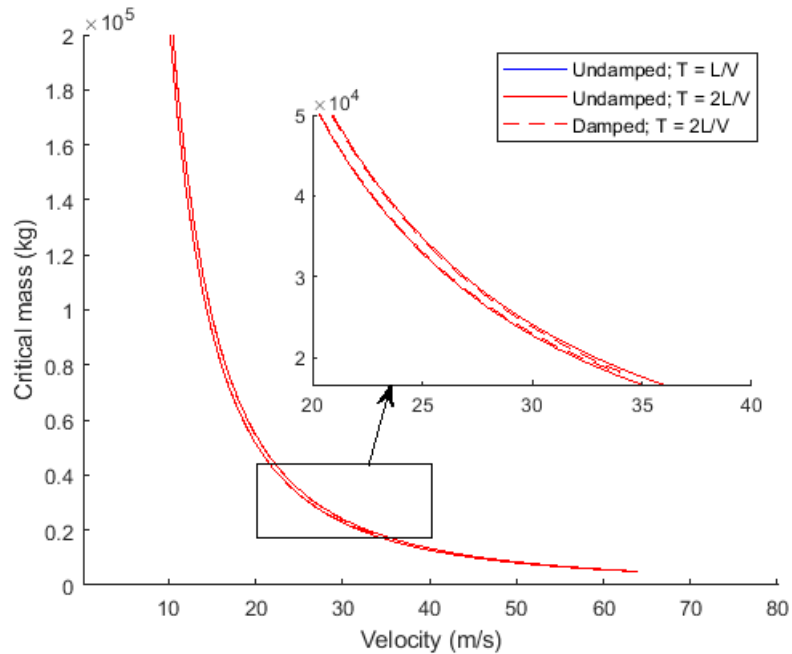
Figure 6.3: Instability domains slab-track with an infinite layer of soil

From Fig. 6.3 we see that even for the damped case, there are still instability domains. Note that the undamped instability domain governed by T_1 lies outside the domain shown. The same conclusion may be drawn from the second calculation, of which the results are shown in Fig. 6.4. Furthermore, in Fig. 6.4 we see that several islands of instability show up in the undamped case. Also, the main instability domain is, although broken up by a stable velocity range, elongated. Overall, there is a stark difference between the two undamped calculations. As mentioned above, the coupling of the supports could be an explanation. One can imagine that in the model with infinite soil there will be more energy being radiated away due to the fact that no waves will be reflected from the soil layer, which is partly confirmed by the existence and visibility of more and higher instability zones in the second model. We must stress here 'partly' confirmed due to the fact that it is unknown whether Rayleigh waves contribute as well, a more thorough investigation to the flow of energy through the whole model might be able to answer that question.
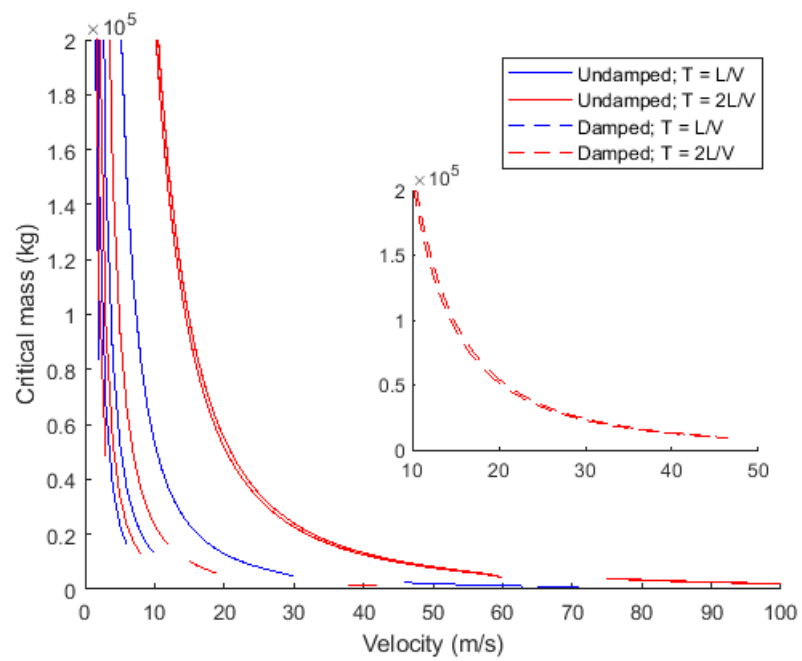
Figure 6.4: Instability domains slab-track with a non-infinite layer of soil

Chapter 7

Numerical verification of Parametric Instability of a moving mass / oscillator

In this section we will verify the results of the preceding chapters by performing numerical time-domain calculations using a finite element model of the periodic structure. These calculations will consist of calculating the time-domain response of the motion of a moving mass / oscillator over a periodic guideway. Furthermore, we will look into the magnitude of the exponential growth per period of oscillation and its dependency on mass and velocity. The growth per period of oscillation will be given by the value λ as defined by $e^{\lambda \omega_{osc} t}$. Two different structures will be calculated: the Regular Railroad Track and the Hyperloop with a steel tube. The difference between these structures lies with the fact that their dispersion curves are significantly different (see section 4). For the latter case we will also consider an oscillator.

7.1 Numerical verification of a regular railway track

In the case of the regular railroad track we will be using most parameters from Table 4.2, although with $K_v = 1 * 10^9$ N/m and $\eta_v = 0.001$ s. As we have not given the specific transition curves ascociated with this set of parameters, we will give those here. The upper and lower boundary values for two different values of V are plotted in Fig. 7.1, where the red line indicates the transition curves associated with T_2.

First we will look at the second velocity denoted in Fig. 7.1 which is equal to 17 m/s. Four locations have been chosen, two that are within the instability domain (139300 kg, 141000 kg) and two that are outside and above the domain(145800 kg, 150000 kg). The results of the calculations are shown in Figs. 7.2 where, if appliccable, the value of λ will be given as well as the period of oscillation that is observed.

As we can see from Figs. 7.2a and 7.2b, inside the instability domain the period of oscillation is similar to the period that dictates the boundary, in this case $T_2 = 2L/V = 2 * 0.6/17 = 0.07$s. This result is in perfect analogy with the Mathieu equation (see Fig. 3.10), where inside the instability domains the period of oscillation is also dictated by the boundaries and remains constant throughout the whole instability domain. Outside the domain we observe a mixed
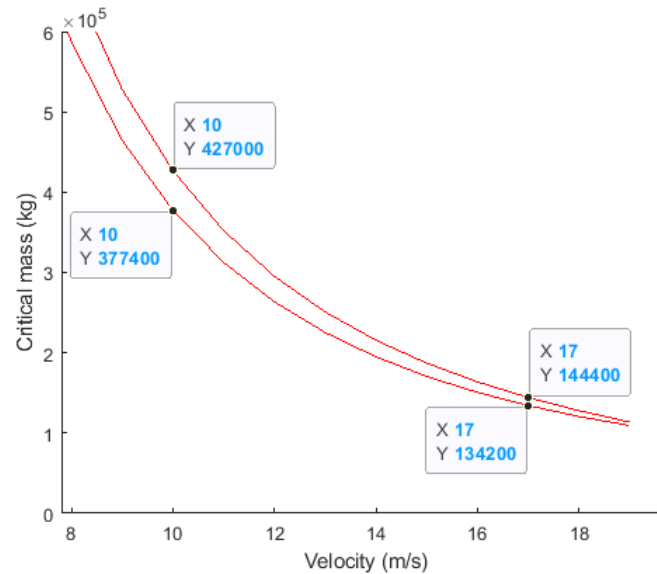
Figure 7.1: Instability domain regular railroad track for T_2

periodic signal with both T_1 and T_2 (Fig. 7.2c), that is if we are close to the boundary. Now it must be noted that in the third case, where we observe mixed periodic motion, the steady state has not been reached yet. We merely observe T_2 periods because at the start of the Finite Element calculation there will be transient vibrations (induced by the 'sudden' start of the calculation), which are affected by the mechanism responsible for the instability itself. In the steady-state and outside the instability domain, the displacement will always be periodic with T_1. This has been an observation throughout several calculations made that were nearby the transition curve. Where it was observed that the unstable vibrations induced by the 'start-up' would be periodic with T_2, which immediately start to dampen out and finally are completely taken over by stable vibrations with period T_1. When we are well outside the instability domain the period of oscillation is dictated by the sleeper distance defined by T_1 (Fig. 7.2d).

If the mass is increased well away of the instability domain, for example 750000kg, the period of oscillation increases as would be expected from an increasing mass. In that case, the mass will be too great in order for the periodic inhomogeneity to have an effect and thus it would resort more or less to its natural frequency. In the stable cases, we also observe that the periodic motion is almost perfectly harmonic, which explains the low amount of harmonics that were needed in the calculation of the transition curves. If we compare the values of λ we see that further inside the instability domain the exponential growth is larger, other calculations have shown that if we would move towards the lower boundary this value would decrease again. Once more, the results are in perfect analogy with the Mathieu equation.

For the case $V = 10$ m/s we have chosen the following three location: inside the domain (402200kg), on the boundary (427000kg), and well outside the instability domain (450000kg). The graphed results from the mentioned calculations are shown in Figs. 7.3. Regarding the periods, similar behaviour as before is observed. Except for the fact that nearby the boundary the motion periodic with T_2 is much less damped. The value of λ inside the instability domain has a value of 0.0175, from which we may conclude that per oscillation period the instability is more significant for lower velocities. A physical explanation of this has been given in Chapter 4.2.1, which is now proven with these numerical calculations. Furthermore we may conclude

(a) Unstable

(b) Unstable
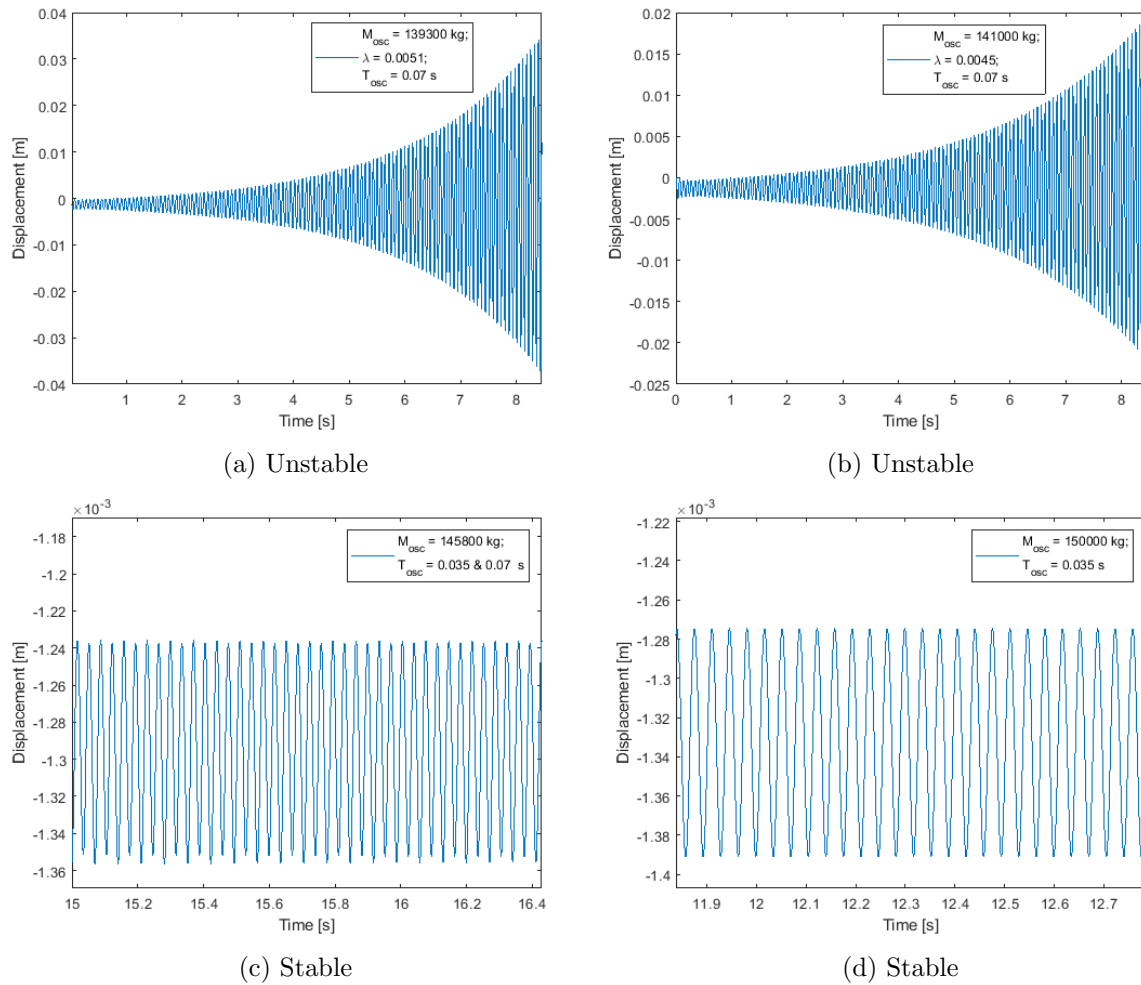
(c) Stable

(d) Stable

Figure 7.2: Numerical simulations for V = 17 m/s

that either one or both of the calculations (i.e. the time-domain response and transition curve calculations) do not have a perfect accuracy, as one can see from Fig. 7.3b that we have stable motion 'on' the boundary.

7.2 Numerical verification of the Hyperloop with a steel tube

In this section we will continue to verify the transition curves as calculated for the Hyperloop steel tube case and investigate any differences with the regular railroad case. As the instability domain governed by T_1 does not disappear in the case of the Hyperloop, we will verify that domain as well. We will cover the instability domains of both a moving mass and oscillator.

7.2.1 Numerical verification for a moving mass

First, we will start with a moving mass. To that end, four calculations have been made of either the T_1 and T_2 instability domains. The chosen velocities are 24.2 and 70 m/s respectively. The

(a) Unstable

(b) Stable

(c) Stable
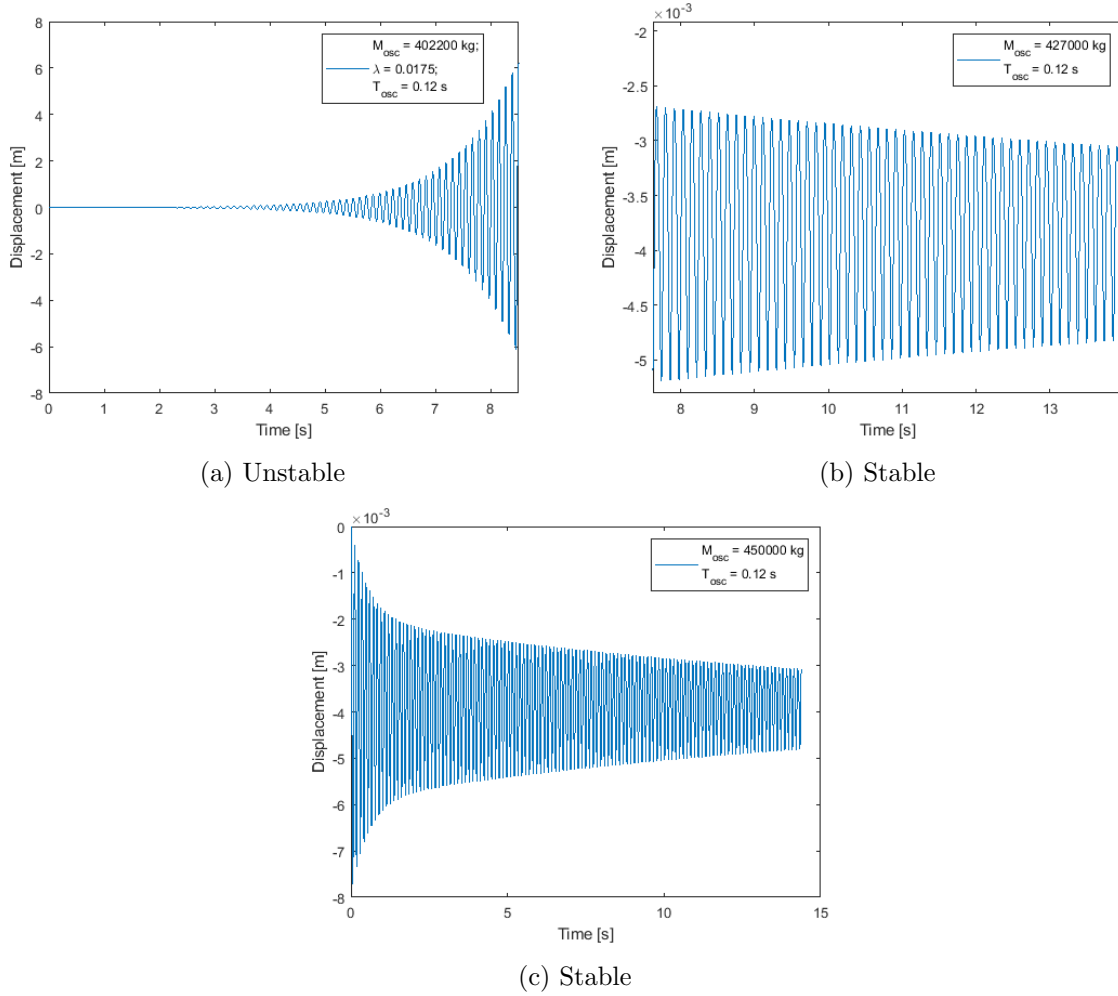
Figure 7.3: Numerical simulations for V = 10 m/s

four points are respectively below the boundary (37460000 kg), inside the domain (39000000 kg), below the lower boundary (7828000 kg), and once again inside the domain (9000000 kg). The choice to choose locations at the lower boundary comes down to the fact that for larger values of the mass the FEM calculations are numerically unstable. One is referred to Fig. 4.13 in Section 4.3.1 for the instability domain on which these values are based.

From Fig. 7.4a we observe stable periodic motion with T_1, although highly asymmetric. Which explains the high number of harmonics that were needed in the calculation of the instablity boundaries. The asymmetry itself is caused by the large ratio between the beam and support stiffness (see Chapter 4.3.1). In the unstable case (see Fig. 7.4b) we observe that the instability is much greater than the instabilities observed in the previous section, with a value of $\lambda = 0.175$. Furthermore, the observed motion is once more periodic with T_2, as dictated by the type of instability (i.e. T_1 or T_2).

As can be seen from Fig. 7.5a the motion outside the first T_1 instability domain is once again dictated by the support distance. Inside the instability domain, see Fig. 7.5b, the oscillations are now also periodic with T_1. Furthermore, the magnitude of exponential growth is much less severe as is expected from higher instability zones (see also Section 3.2.2.2 where we concluded

(a) Stable

(b) Unstable
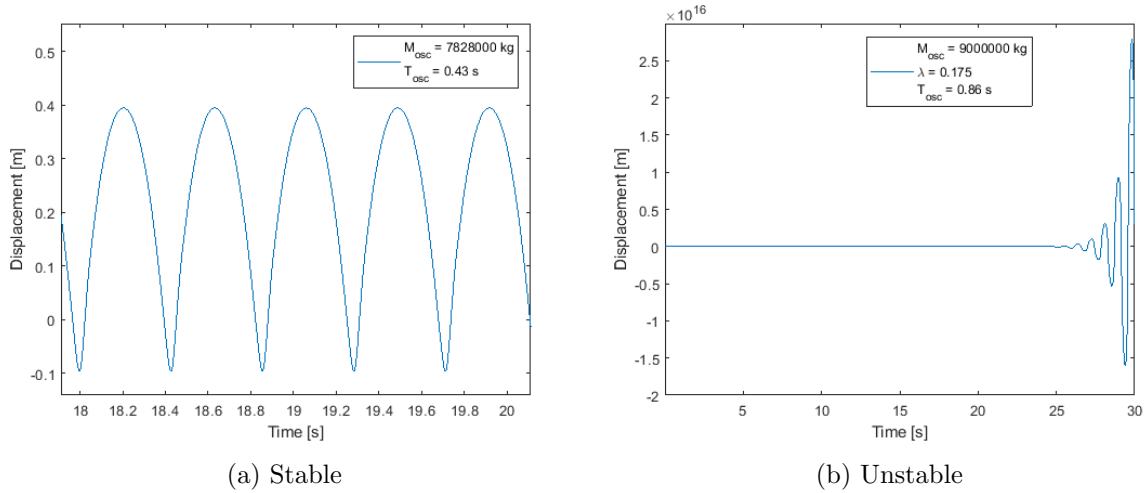
Figure 7.4: Numerical simulations Hyperloop steel tube

(a) Stable

(b) Unstable
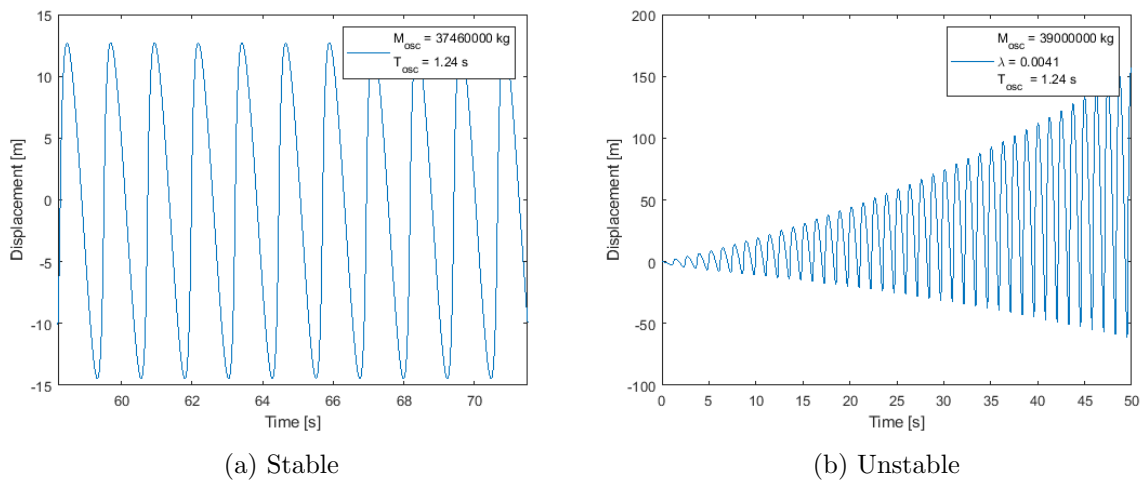
Figure 7.5: Numerical simulations Hyperloop steel tube

similarly).

We may thus conclude that in both cases, i.e. Hyperloop and Regular Track, the calculated transition curves are correct and indeed for Mass-Velocity combinations inside the instability domains we will see instability. By far the most interesting conclusion is the near perfect analogy between the Mathieu equation and the instability of a moving mass.

7.2.2 Numerical verification for a moving oscillator

In this section we will perform numerical calculations where the moving mass has been replaced by an oscillator. The set of parameters we use are similar to those in Chapter 4.2.5, where we will use an oscillator stiffness of $1 * 10^{10}$ N/m for two calculations and the value of $1 * 10^8$ N/m for one calculation. All three cases are calculated for $V = 8$ m/s and are respectively speaking below the lower boundary (500000 kg), inside the instability domain (564200 kg), and once again

inside the instability domain (52220 kg).

(a) Stable (b) Unstable
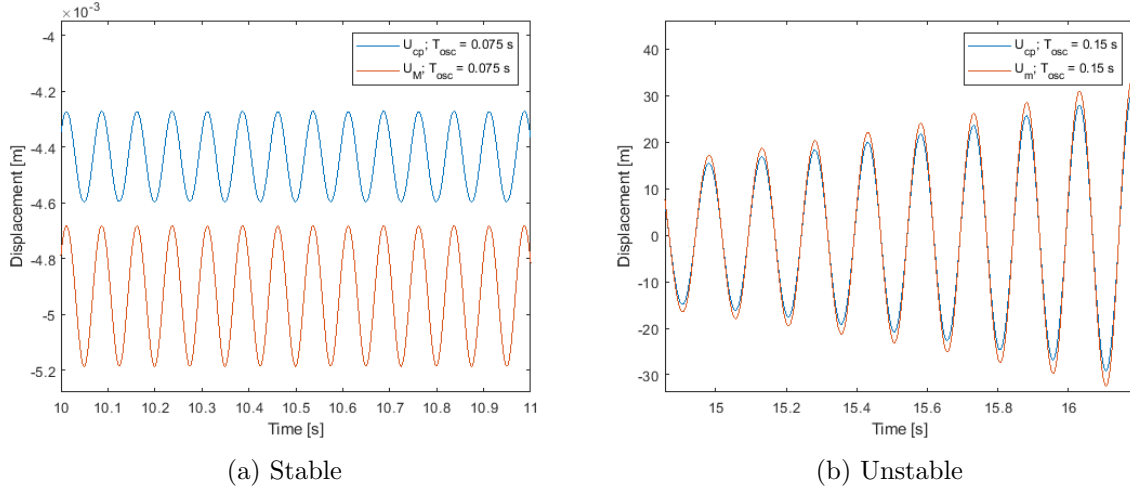
Figure 7.6: Numerical simulations Oscillator; $K_{osc} = 1e10$ N/m

The first two cases are shown in Fig. 7.6, from which we can see that the displacement of the Contact Point (i.e. U_{cp}) closely follows the displacement of the Mass (i.e. U_{m}). Once again, outside the instability domain we observe steady-state oscillations dictated by T_1 whilst inside the instability they obey T_2. Similar conclusions may be drawn from Fig. 7.7. Although the displacement of the contact point is not equal to that of the oscillator and is influenced by a higher harmonic, the fundamental frequency is still equal to T_2.

(a) Stable (b) Unstable
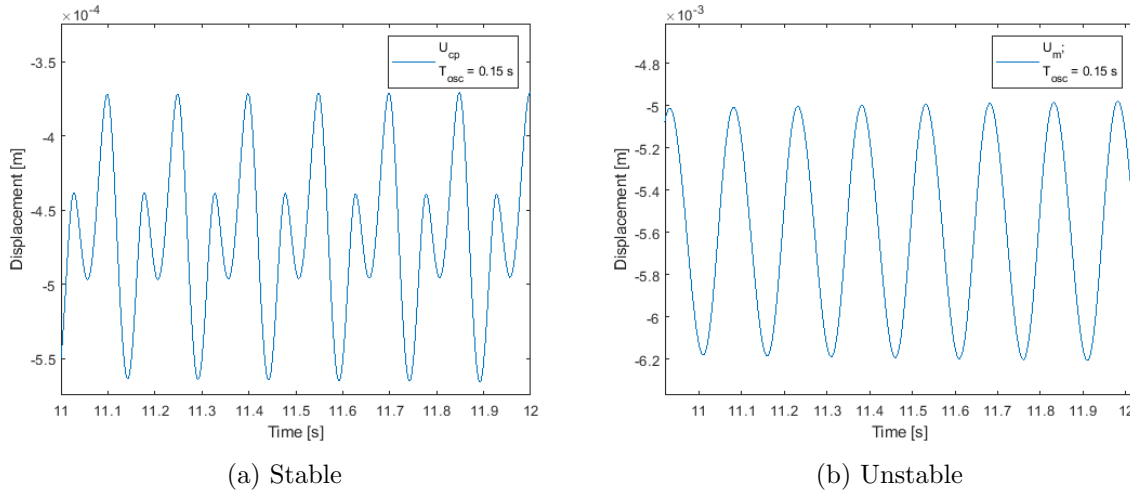
Figure 7.7: Numerical simulation Oscillator; $K_{osc} = 1e8$ N/m

By this we can conclude that also in the case of an oscillator the transition curves are calculated correctly. Furthermore, the analogy with the Mathieu equation is appliccable for an oscillator as well.

Chapter 8

Conclusions and recommendations

8.1 Conclusions

As stated in the introduction, our first goal of this thesis was to extend on the present study of the Floquet exponents of the Mathieu equation. We have applied Floquet theory to derive the transition curves of the instability domains and the Floquet exponents in order to gain insight in the dynamic behaviour of the solutions both within and outside these domains. The main conclusions that may be drawn are as follows:

1. The exponential growth of the solution will be larger for larger values of μ, which signifies the increase of the parametric forcing. We have also seen that the higher instability domains show a smaller exponential increase, i.e. for a larger value of δ.

2. If damping is introduced in the system this will decrease the Floquet exponents exactly with that value, and therefore shift the transition curves upwards. Also, it will not affect the ascociated periods of oscillation in the stable domains.

Our second goal was to conduct a parametric study of Parametric Instability on a variety of different models regarding either a moving mass or an oscillator. We have derived methods to calculate the transition curves of those models and investigated the effects of their properties on those curves. We may conclude the following:

1. It was shown that the constant Fourier series component is not necessary for the calculations of the moving mass/oscillator;

2. The instability zones are influenced by the ratio between the stiffness of the supports and that of the beam inbetween. This has been encapsulated within the value α_v. Increasing this value will generally lead to the widening of the instability domains and in most cases will shift rightward. However, the direction of this shift will depend on the intrinsic properties of the beam;

3. Depending on the intrinsic properties (i.e. mass, stiffness, and length) of the periodic beam, and thus dependent on the locations of the stop- and propagation bands, the transition curves will show different trends. For example, islands of instability may appear that create ranges of velocities inbetween these islands where the motion will be stable.

4. The velocity parameter V is a near direct analogy with the parameter μ from the Mathieu equation. The latter parameter indicates the strength of the periodic variation of stiffness. A decrease (increase) of the parameter V (μ) will generally lead to a greater instability;

5. For low velocities, damping will have a stabilising effect. It will move the 'tongues' of the instability domains leftward and decrease their width. For large velocities however, damping might as well increase the width of the instability domains.

6. An oscillator will generally decrease the widths of the domains and will shift them to lower values of the mass;

7. A support with an oscillator will heavily influence the trend of the boundaries. Of course, this depends on the relative differences between beam stiffness, support stiffnesses, and support mass. Nonetheless, this indicates that models having boundary conditions with complex dynamic properties will significantly affect the instability domains. Accurately representing the structure is thus a must when Parametric Instability is deemed to be important;

8. If a 2-dimensional lattice layer is added to the model, energy can radiate away in that layer. This will lead to a similar effect as that of adding damping;

9. Although uncertain, it seems as if the coupling of the supports through a 2-dimensional lattice layer indeed has an effect on the instability domains. Whether this is through body- or Rayleigh-waves is unknown.

Belonging to the second goal as well, were the real world applications. From which we may conclude the following:

1. In case of a Hyperloop system, the instability domains for a moving mass were significantly larger as compared with the other applications;

2. The test pod from Hardt Hyperloop however does not have any significant parametric instability zones;

3. In a real case scenario of a regular railway track founded on a layer of ballast and soil, no Parametric Instability domains are shown at all;

4. In the case of a High-speed slab track parametric instability does play a role. However, its exact significance is unknown.

Finally, our third goal covered the numerical calculations performed as to verify the calculated transition curves and investigate the analogy between the Mathieu equation and the moving mass / oscillator. The following conclusions may be drawn:

1. The existence of the instability zones were proved with the time-domain calculations;

2. Although clearly a different system, governed by a different partial differential equation, there is also a clear analogy between the results from the Mathieu equation and that of a moving mass/oscillator. We may thus conclude that the use of that analogy for solving the transition curves is correct.

8.2   Recommendations

Anytime a study of a certain subject is performed, it is natural that new questions arise. These will be given in the form of the following recommendations:

1. Although it is clear that supports with an oscillator affect the transition curves by its natural frequency, it is so far unknown how far-reaching the effect is if one is to model a complex support in the form of a continuous beam representing a column. By increasing the complexity of the support condition one will be able to expand on the mechanisms affecting the boundary conditions;

2. It is the idea of the author that Anomalous Dispersion might play a role in Parametric Instability as well. A suggestion would thus be to analyse whether it has any influence on the radiation of anomalous Doppler waves;

3. Although we have seen a clear relation between the dispersion curves and the instability, the real mechanism behind Parametric Instability remains a question. Although the suggestion of anomalous Doppler waves is likely, it has not been proven. To that end, an analysis to the flow of energy throughout the system in the form of the energy spectral density has unsuccesfully been performed (hence it has been omitted from this thesis). Therefore, if one is to find a relation between the instability and anomalous Doppler waves, they should propose a solid method to analyse the energy flow within the system;

4. In Chapter 6 we concluded that parametric instability will not be present in the case of a regular railway track. To further strengthen this conclusion, one should perform a more extensive parametric study based on several real world applications;

5. We have also seen that in the case of a slab track parametric instability will be present. A similar conclusion as above may be drawn here: whether the role of parametric instability indeed is important must be further investigated by using models that are more realistic;

6. Especially for a structure like the Hyperloop parametric instability may be an important factor. Proper modelling of the complete structure is a prerequisite for this matter and thus should be investigated;

7. The method by de Oliveira Barbosa [20] is very computationally expensive if one includes a lattice. This problem only increases if the support distance is increased (e.g. 30 m for the Hyperloop), and by that the amount of lattice particles. Finding a faster method to calculate the Fourier coefficients would greatly speed up the process. Minor improvements had been made by the author by altering the integration scheme. However, finding other ways could prove profitable. During the thesis process the suggestion of using contour integration was made, although unsure of its applicability, it could be worth a try;

Bibliography

[1] K. Abe, Y. Chida, P. E. Balde Quinay, and K. Koro. Dynamic instability of a wheel moving on a discretely supported infinite rail. *Journal of Sound and Vibration*, 333(15):3413–3427, 2014.

[2] G. Acar and B. F. Feeny. Floquet-Based Analysis of General Responses of the Mathieu Equation. *Journal of Vibration and Acoustics, Transactions of the ASME*, 138(4), 2016.

[3] F. Afzali, G. D. Acar, and B. F. Feeny. Analysis of the periodic damping coefficient equation based on floquet theory. *Proceedings of the ASME Design Engineering Technical Conference*, 8(3):1–7, 2017.

[4] G. Allaire, C. Conca, and M. Vanninathan. The Bloch transform and applications. *ESAIM: Proceedings*, 3:65–84, 1998.

[5] M. Amrein and T. P. Wihler. An adaptive Newton-method based on a dynamical systems approach. *Communications in Nonlinear Science and Numerical Simulation*, 19(9):2958–2973, 2014.

[6] S. A. Asiri and Y. Z. AL-Zahrani. Theoretical Analysis of Mechanical Vibration for Offshore Platform Structures. *World Journal of Mechanics*, 04(01):1–11, 2014.

[7] A. Banerjee. Non-dimensional analysis of the elastic beam having periodic linear spring mass resonators. *Meccanica*, 55(5):1181–1191, 2020.

[8] B. Barth. *The Bloch Transform on L p -Spaces*. PhD thesis, 2013.

[9] P. M. Belotserkovskiy. On the oscillations of infinite periodic beams subjected to a moving concentrated force. *Journal of Sound and Vibration*, 193(3):705–712, 1996.

[10] F. Bloch. Über die Quantenmechanik der Elektronen in Kristallgittern (About the quantum mechanics of electrons in crystal lattices). *Zeitschrift fur Physik*, 1928.

[11] M. Botshekan, M. Tootkaboni, and A. Louhghalam. On the dynamics of periodically restrained flexural structures under moving loads. *International Journal of Solids and Structures*, 180-181:62–71, 2019.

[12] D. G. Braak. Concrete Hyperloop. Master's thesis.

[13] C. E. Bradley. Acoustic Bloch Wave Propagation in a Periodic Waveguide. *The Journal of the Acoustical Society of America*, 96(3):1844–1853, 1994.

[14] L. Brillouin. Wave Propagation in Periodic Structures: electric filters and crystal lattices. *Nature*, 158(4026):926–926, 1946.

[15] L. Cabras, A. Movchan, and A. Piccolroaz. Floquet-Bloch waves in periodic networks of the Rayleigh beams: honeycomb systems, dispersion degeneracies and structured interfaces. (July), 2017.

[16] H. Chebli, D. Clouteau, and L. Schmitt. Dynamic response of high-speed ballasted railway tracks: 3D periodic model and in situ measurements. *Soil Dynamics and Earthquake Engineering*, 28(2):118–131, 2008.

[17] H. Chebli, R. Othman, and D. Clouteau. Response of periodic structures due to moving loads. *Comptes Rendus - Mecanique*, 334(6):347–352, 2006.

[18] D. Clouteau, M. L. Elhabre, and D. Aubry. Periodic BEM and FEM-BEM coupling. Application to seismic behaviour of very long structures. *Computational Mechanics*, 25(6):567–577, 2000.

[19] J. M. de Oliveira Barbosa, A. B. Fărăgău, and K. N. van Dalen. A lattice model for transition zones in ballasted railway tracks.

[20] J. M. de Oliveira Barbosa and K. N. van Dalen. Dynamic response of an infinite beam periodically supported by sleepers resting on a regular and infinite lattice: Semi-analytical solution. *Journal of Sound and Vibration*, 458:276–302, 2019.

[21] P. Gómez García and J. P. Fernández-Álvarez. Floquet-bloch theory and its application to the dispersion curves of nonperiodic layered systems. *Mathematical Problems in Engineering*, 2015, 2015.

[22] V. K. Ingle and J. G. Proakis. *Digital Signal Processing Using MATLAB , 3rd Edition*, volume 5. 2012.

[23] L. Jezequel and M. Exposition. Response of Periodic Systems to a Moving Load. 48(SEPTEMBER 1981):613–618, 2016.

[24] I. Kovacic, R. Rand, and S. M. Sah. Mathieu's equation and its generalizations: Overview of stability charts and their features. *Applied Mechanics Reviews*, 70(2), 2018.

[25] V. Kumar and O. Ridge. Vibration Characteristics of Periodically Supported Beam Vibration Characteristics of Periodically Supported Beam Master of Technology. (June 2012), 2016.

[26] R. Lassoued, M. Lecheheb, and G. Bonnet. Green's function and Bloch theory for the analysis of the dynamic response of a periodically supported beam to a moving load. *Journal of Physics: Conference Series*, 382(1), 2012.

[27] J. F. Lu, Q. S. Feng, and D. D. Jin. A dynamic model for the response of a periodic viaduct under a moving mass. *European Journal of Mechanics, A/Solids*, 73(October 2018):394–406, 2019.

[28] J. F. Lu, H. Mei, and L. Zhong. Dynamic response of a periodic viaduct to a moving loading with consideration of the pile–soil–structure interaction. *Acta Mechanica*, 226(6):2013–2034, 2015.

[29] J. F. Lu, L. Zhong, and R. Zhang. Dynamic response of a periodic viaduct to a moving point loading. *Archive of Applied Mechanics*, 85(1):149–169, 2015.

[30] T. Marolt Čebašek, A. F. Esen, P. K. Woodward, O. Laghrouche, and D. P. Connolly. Full scale laboratory testing of ballast and concrete slab tracks under phased cyclic loading. *Transportation Geotechnics*, 17(June):33–40, 2018.

[31] E. Mathieu. Journal de Mathematiques Pures et Appliques. *Journal de Mathématiques Pures et Appliquées*, 13:137–203, 1868.

[32] D. J. Mead. Free wave propagation in periodically supported, infinite beams. *Journal of Sound and Vibration*, 11(2):181–197, 1970.

[33] D. J. Mead. A general theory of harmonic wave propagation in linear periodic systems with multiple coupling. *Journal of Sound and Vibration*, 27(2):235–260, 1973.

[34] D. J. Mead. Wave propagation and natural modes in periodic systems: I. Mono-coupled systems. *Journal of Sound and Vibration*, 40(1):1–18, 1975.

[35] D. J. Mead. Wave propagation and natural modes in periodic systems: II. Multi-coupled systems, with and without damping. *Journal of Sound and Vibration*, 40(1):19–39, 1975.

[36] D. J. Mead. A new method of analyzing wave propagation in periodic structures; Applications to periodic timoshenko beams and stiffened plates. *Journal of Sound and Vibration*, 104(1):9–27, 1986.

[37] D. J. Mead and Š. Markuš. Coupled flexural-longitudinal wave motion in a periodic beam. *Journal of Sound and Vibration*, 90(1):1–24, 1983.

[38] D. J. Mead and Y. Yaman. The Harmonic Response of Uniform Beams on Multiple Linear Supports: A Flexural Wave Analysis. *Journal of Sound and Vibration*, 141(3):465–484, 1990.

[39] D. J. Mead and Y. Yaman. The response of infinite periodic beams to point harmonic forces: A flexural wave analysis. *Journal of Sound and Vibration*, 144(3):507–529, 1991.

[40] A. V. Metrikin. Unstable transverse oscillations of an object moving uniformly along an elastic guide as a result of the anomalous Doppler effect. *Akusticheskij Zhurnal*, 40(1):99–103, 1994.

[41] A. V. Metrikine. Parametric Instability of a Moving Particle on a Periodically Supported Infinitely Long String. *Journal of Applied Mechanics*, 75(1):0110061–0110068, jan 2008.

[42] A. V. Metrikine and A. L. Bosch. Dynamic response of a two-level catenary to a moving load. *Journal of Sound and Vibration*, 292(3-5):676–693, 2006.

[43] A. V. Metrikine and K. Popp. Vibration of a periodically supported beam on an elastic half-space. *European Journal of Mechanics, A/Solids*, 18(4):679–701, 1999.

[44] A. V. Metrikine and A. C. Vrouwenvelder. Surface ground vibration due to a moving train in a tunnel: two-dimensional model. *Journal of Sound and Vibration*, 234(1):43–66, 2000.

[45] MIT. Bragg scattering vs. local resonances. In *Unknown*, pages 5–9.

[46] T. Muthukumar. Bloch-Floquet transform. 2:1–19, 2014.

[47] A. H. Nayfeh. *Introduction to Perturbation Techniques (Ali Hasan Nayfeh)*, volume 24. 1993.

[48] A. H. Nayfeh. *Perturbation methods.* 2004.

[49] A. H. Nayfeh and D. Mook. Nonlinear oscillations. *Physics Today*, 15(9):63–65, 1962.

[50] A. Nordborg. Vertical Rail Vibrations: Parametric Excitation. *Acustica*, 84(2):280–288, 1998.

[51] A. Nordborg. Vertical Rail Vibrations: Pointforce Excitation. *Acustica*, 84(2):280–288, 1998.

[52] M. Odeh. About the Quantum Mechanics of the Electrons in Crystal Lattices Historical Background : Bloch Wave Theorem :. page 555, 2018.

[53] M. Pirmoradian, M. Keshmiri, and H. Karimpour. Instability and resonance analysis of a beam subjected to moving mass loading via incremental harmonic balance method. *Journal of Vibroengineering*, 16(6):2779–2789, 2014.

[54] A. S. Suiker, A. V. Metrikine, and R. De Borst. Dynamic behaviour of a layer of discrete particles, Part 1: Analysis of body waves and eigenmodes. *Journal of Sound and Vibration*, 240(1):1–18, 2001.

[55] A. S. Suiker, A. V. Metrikine, and R. De Borst. Dynamic behaviour of a layer of discrete particles, Part 2: Response to a uniformly moving, harmonically vibrating load. *Journal of Sound and Vibration*, 240(1):19–39, 2001.

[56] J. van Oostrum. Combination parametric resonance of an oscillator that moves uniformly along a beam on a periodically inhomogeneous foundation. Master's thesis, 2021.

[57] S. N. Verichev and A. V. Metrikine. Instability of vibrations of a mass that moves uniformly along a beam on a periodically inhomogeneous foundation. *Journal of Sound and Vibration*, 260(5):901–925, 2003.

[58] S. N. Veritchev. *Instability of a vehicle moving on an elastic structure.* 2002.

[59] A. I. Vesnitskiĭ and A. V. Mertrikin. Transition radiation in mechanics. *Uspekhi Fizicheskikh Nauk*, 166(10):1068, 1996.

[60] A. Vesnitskii and A. Metrikine. Transient radiation in a periodically non-uniform elastic guide, 1993.

[61] A. I. Vesnitskii and A. V. Metrikin. Parametric instability in the oscillations of a body moving uniformly in a periodically inhomogeneous elastic system. *Journal of Applied Mechanics and Technical Physics*, 34(2):266–271, 1993.

[62] M. Y. Wang and X. Wang. Frequency band structure of locally resonant periodic flexural beams suspended with force-moment resonators. *Journal of Physics D: Applied Physics*, 46(25), 2013.

[63] X. Wang and M. Y. Wang. An analysis of flexural wave band gaps of locally resonant beams with continuum beam resonators. *Meccanica*, 51(1):171–178, 2016.

[64] M. Ward. Basic Floquet Theory. In *None*, volume 1. 2010.

[65] Y. Watanabe and N. Sugimoto. Flexural wave propagation in a spatially periodic structure of articulated beams. *Wave Motion*, 42(2):155–167, 2005.

[66] Y. Xiao, J. Wen, D. Yu, and X. Wen. Flexural wave propagation in beams with periodically attached vibration absorbers: Band-gap behavior and band formation mechanisms. *Journal of Sound and Vibration*, 332(4):867–893, 2013.

Appendix A

Orthogonality of Complex Numbers

In this section the orthogonality of complex numbers to be used in the formulation of Hill's infinite determinant will be derived. It is a short but fun derivation, and helpful in understanding why Hill's infinite determinant may be created.

Let's start with a complex Fourier series with fundamental frequency ω_0:

$$\sum_{n=-\infty}^{\infty} C_n \mathrm{e}^{in\omega_0 t}$$

Multiplying with $\mathrm{e}^{-im\omega_0 t}$, integrating over the period of vibration (T_0), changing the order of summation and integration, and carrying out the integration leads to:

$$\sum_{n=-\infty}^{\infty} C_n \int_0^{T_0} \mathrm{e}^{i(n-m)\omega_0 t} dt = \sum_{n=-\infty}^{\infty} \mathrm{e}^{i(n-m)\omega_p t}\Big|_0^{T_0}$$

an inspection of the lower boundary clearly gives 1 as result. When $n \neq m$, the upper boundary will just be an integer multiple of 2π (due to $T_0 = 2\pi/\omega_0$), hence the result of evaluating both boundaries will be zero. However, when $n = m$, the integral changes to:

$$\int_0^{T_0} 1 dt = T_0$$

Hence, the final result can be written as:

$$\sum_{n=-\infty}^{\infty} C_n \int_0^{T_0} \mathrm{e}^{i(n-m)\omega_p t} dt = C_n T_0 \delta_{mn}$$

Now, as in the derivation of Hill's infinite determinant also exponents like $(n+1)$ or $(n/2+1)$ may appear it is useful to show how in a fast manner the results of orthogonality may be derived. Noticing that in fact only the period of vibration of the original function and the exponent matters, a solution to the latter exponent may be derived as:

$$\frac{n}{2} + 1 - \frac{m}{2} = 0 \rightarrow m = n + 2$$

Where the fact that the period of vibration is equal to $\frac{n}{2}$ has been used, which leads to the following result:

$$\sum_{n=-\infty}^{\infty} C_n \int_0^{T_0} e^{i(\frac{n}{2}+1-\frac{m}{2})t} dt = C_n T_0 \delta_{m,n+2}$$

Appendix B

Green's function Periodic Structure

As mentioned in section 2.2.1 we will cover the derivation of the Greens function for a Periodic Structure by means of the Transfer Matrix Method. Furthermore, we will cover two example that will verify the correctness of the method. The first example will be an infinite similar beam, where 'similar' indicates that we are actually working with a homogeneous beam. The second example is based on what is used by Nordborg [51] and Barbosa [20]. Finally, we will also show that it is possible to analytically derive the Greens function in a much easier fashion than was done by Nordborg [51].

First, write down the full solution for the constant vectors (from Eq. 2.2.15) similar to any eigenvalue problem:

$$\underline{A} = \sum_{i=1}^{4} \alpha_i \underline{A}_i(\lambda_i, \omega) \tag{B.0.1}$$

Where each $\underline{A}_i$ represents the eigenvector and α_i being a constant which should be defined by the B.C.'s for an arbitrary forcing (e.g. the 4 B.C.'s one would obtain when applying a harmonic point load mid-span). Note that the dependence on cell number n has been removed, as the response of an arbitrary cell is linked to the $n = 0$ cell by the Bloch boundary condition. As the full solution, Eq. 2.2.10, can also be written in matrix form: $W(x, \omega) = \underline{E}(x, \omega)\underline{A}(\lambda, \omega)$. The vector $\underline{E}(x, \omega)$ is defined by the general solution as written in Eq. 2.2.10 and reads:

$$\underline{E} = \begin{bmatrix} e^{ikx} \\ e^{-ikx} \\ e^{kx} \\ e^{-kx} \end{bmatrix} \tag{B.0.2}$$

The full solution in the 0th cell can now be written as:

$$W(x, \lambda, \omega) = \sum_{i=1}^{4} \alpha_i \underline{E}(x, \omega)\underline{A}_i(\lambda_i, \omega), \quad \text{for: } x = 0..L \tag{B.0.3}$$

And the solution in an arbitrary cell:

$$W_m(x, \lambda, \omega) = \sum_{i=1}^{4} \alpha_i \mathrm{e}^{\mathrm{i}\lambda_i(\omega)mL} \underline{E}(x, \omega) \underline{A}_i(\lambda_i, \omega), \quad \text{for: } x = 0..L \tag{B.0.4}$$

Interesting to note here that by solving with the Bloch boundary condition, a multitude (i.e. four) of constant vectors are derived, changing the solution from a simple summation of four waves with four constants, to four different solutions with each their own four waves and accompanying constants. A physical interpretation of this would be the fact that at the boundaries of each cell, waves will both be transmitted and reflected, leading to the need of the full solution (i.e. all four waves from the general solution) to be able to fully determine the vibrational behaviour. Much like the case for a single beam on supports, where all four waves contribute to the different modes of vibration. However, in the case of an infinite periodic beam, we will have four Bloch wave numbers, describing the propagation, and/or attenuation, of a single Bloch wave, which itself consists of four waves. Thus one could just say there are four waves in the whole system (instead of a summation of different waves). It is just a matter of language (mathematics in this case) and the physical interpretation itself. This will be elucidated in the next section, where the transfer matrix method will be applied on two examples.

An important remark about Eq. B.0.4 is the fact that when solving for a certain load, one would have to discern the directions of the different Bloch waves. Just as in a non-periodic infinite beam, there will be two waves in each direction. The direction of the waves are defined by the group velocity (i.e. $\frac{d\omega}{d\lambda}$) which can be calculated from the dispersion curve of the periodic structure. With that, the solution in an arbitrary cell will not be the summation over all four waves, just two of them:

$$W_{+m}(x, \lambda, \omega) = \sum_{ir=1r}^{2r} \alpha_{ir}(\omega) \mathrm{e}^{\mathrm{i}\lambda_{ir}(\omega)mL} \underline{E}(x, \omega) \underline{A}_{ir}(\lambda_{ir}, \omega), \quad \text{for: } x = 0..L$$

$$W_{-m}(x, \lambda, \omega) = \sum_{il=1l}^{2l} \alpha_{il}(\omega) \mathrm{e}^{\mathrm{i}\lambda_{il}(\omega)mL} \underline{E}(x, \omega) \underline{A}_{il}(\lambda_{il}, \omega), \quad \text{for: } x = 0..L$$

$$\tag{B.0.5}$$

With Eq. B.0.5, the Green's function is completely determined. Dependent on the type of loading, one is able to solve it analytically by first solving for the propagation constants λ_i, calculating the eigenvectors $\underline{A}_i$, and finally solving for the constants α_i by applying the boundary conditions at the point of loading.

B.1 Infinite similar beam

As mentioned above, our first example will cover an infinite beam that is homogeneous. By which we show that that the Bloch wave function will simplify to the general solution of a homogeneous beam.

Let us start with the infinite similar beam as defined in Fig. B.1. For which the solution in one cell is governed by the following equation of motion:

$$m\ddot{w}_n(x, t) + EI w_n''''(x, t) = 0 \tag{B.1.1}$$

Of which the boundary conditions, in the frequency domain, are dictated by the continuity of displacement, rotation, moment, and shear force:
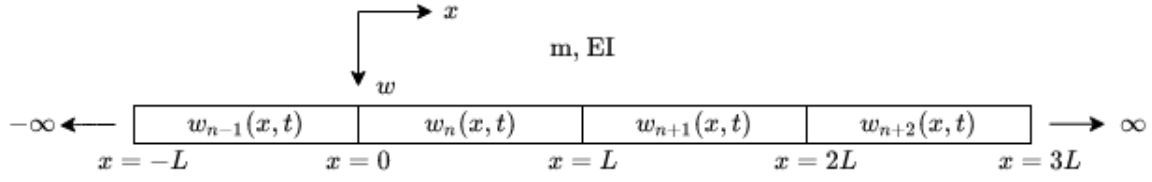
Figure B.1: Infinite similar beam

$$W_n(L, \omega) = W_{n+1}(0, \omega)$$

$$W_n'(x, \omega)|_{x=L} = W_{n+1}'(x, \omega)|_{x=0}$$

$$W_n''(x, \omega)|_{x=L} = W_{n+1}''(x, \omega)|_{x=0} \tag{B.1.2}$$

$$W_n'''(x, \omega)|_{x=L} = W_{n+1}'''(x, \omega)|_{x=0}$$

Writing these boundary conditions in matrix and following the steps from section 2.2.2 gives the following two matrices of **K** and **H**:

$$\mathbf{H} = \begin{bmatrix} e^{ikL} & e^{-ikL} & e^{kL} & e^{-kL} \\ -ike^{ikL} & ike^{-ikL} & -ke^{kL} & ke^{-kL} \\ EIk^2e^{ikL} & EIk^2e^{-ikL} & -EIk^2e^{kL} & -EIk^2e^{-kL} \\ iEIk^3e^{ikL} & -iEIk^3e^{-ikL} & -EIk^3e^{kL} & EIk^3e^{-kL} \end{bmatrix}$$

$$\mathbf{K} = \begin{bmatrix} 1 & 1 & 1 & 1 \\ -ik & ik & -k & k \\ EI^2 & EIk^2 & -EIk^2 & -EIk^2 \\ iEIk^3 & -iEIk^3 & -EIk^3 & EIk^3 \end{bmatrix} \tag{B.1.3}$$

Which gives the following **T** matrix:

$$\mathbf{T} = \begin{bmatrix} e^{ikL} & 0 & 0 & 0 \\ 0 & e^{-ikL} & 0 & 0 \\ 0 & 0 & e^{kL} & 0 \\ 0 & 0 & 0 & e^{-kL} \end{bmatrix} \tag{B.1.4}$$

Which gives the following determinant to be solved:

$$\begin{vmatrix} e^{ikL} - e^{i\lambda L} & 0 & 0 & 0 \\ 0 & e^{-ikL} - e^{i\lambda L} & 0 & 0 \\ 0 & 0 & e^{kL} - e^{i\lambda L} & 0 \\ 0 & 0 & 0 & e^{-kL} - e^{i\lambda L} \end{vmatrix} = \underline{0} \tag{B.1.5}$$

Solving for the determinant gives (note that it is not necessary to do so here, as the equations are all decoupled, but for the sake of completeness the steps are followed):

$$\left(\mathrm{e}^{\mathrm{i}kL} - \mathrm{e}^{\mathrm{i}\lambda L}\right)\left(\mathrm{e}^{-\mathrm{i}kL} - \mathrm{e}^{\mathrm{i}\lambda L}\right)\left(\mathrm{e}^{kL} - \mathrm{e}^{\mathrm{i}\lambda L}\right)\left(\mathrm{e}^{-kL} - \mathrm{e}^{\mathrm{i}\lambda L}\right) = 0 \tag{B.1.6}$$

From which the solutions for λ are evident:

$$\lambda = k, -k, -\mathrm{i}k, \mathrm{i}k \tag{B.1.7}$$

Now, if the eigenvectors are calculated one will see they are as follows:

$$\mathbf{A} = \begin{bmatrix} 1 & 0 & 0 & 0 \\ 0 & 1 & 0 & 0 \\ 0 & 0 & 1 & 0 \\ 0 & 0 & 0 & 1 \end{bmatrix} \tag{B.1.8}$$

Which makes sense, which may be seen by the evaluation of the sum in Eq. B.0.3:

$$W(x,\omega) = \alpha_1 \begin{bmatrix} \mathrm{e}^{-\mathrm{i}kx} \\ \mathrm{e}^{\mathrm{i}kx} \\ \mathrm{e}^{kx} \\ \mathrm{e}^{-kx} \end{bmatrix} \begin{bmatrix} 1 \\ 0 \\ 0 \\ 0 \end{bmatrix} + \sum_{i=2}^{4} \alpha_i \underline{E}(x,\omega)\underline{A}_i(\lambda_i,\omega) \rightarrow \tag{B.1.9}$$

$$W(x,\omega) = \alpha_1 \mathrm{e}^{\mathrm{i}kx} + \alpha_2 \mathrm{e}^{-\mathrm{i}kx} + \alpha_3 \mathrm{e}^{kx} + \alpha_4 \mathrm{e}^{-kx}$$

From which it is evident that the general solution as in Eq. 2.2.10 has been found again. Where the eigenvalues λ_i just denote the phase or amplitude difference if one moves over a length of L. Both of these conclusions make perfectly sense, as this was expected for a periodic elements which are all the same. The result as obtained in this section is often applied in FE-analysis where large periodic structures are analysed, since any evaluation over the whole structure has been reduced to only one element.

B.2 Infinite beam on periodic sleepers

Continuing with the next example, of which the model can be seen in Fig. B.2 and has been taken from Nordborg [51]. Where K_r, M_s, K_s, and C_s denote the pad-stiffness, sleeper mass, stiffness, and damping respectively. Complying with [20] as to have reference, we set the following values:

parameter	value
m [kg/m]	52
EI [Nm^2]	1.234E06
K_r [N/m]	500E06
M_s [kg]	250
K_s [N/m]	42.5E06
C_s [Ns/m]	0

Table B.1: parameters complying with [51] and [20]

We note that the B.C.'s are actually the same as in Eq. 2.2.11, with K defined in [51] as follows:
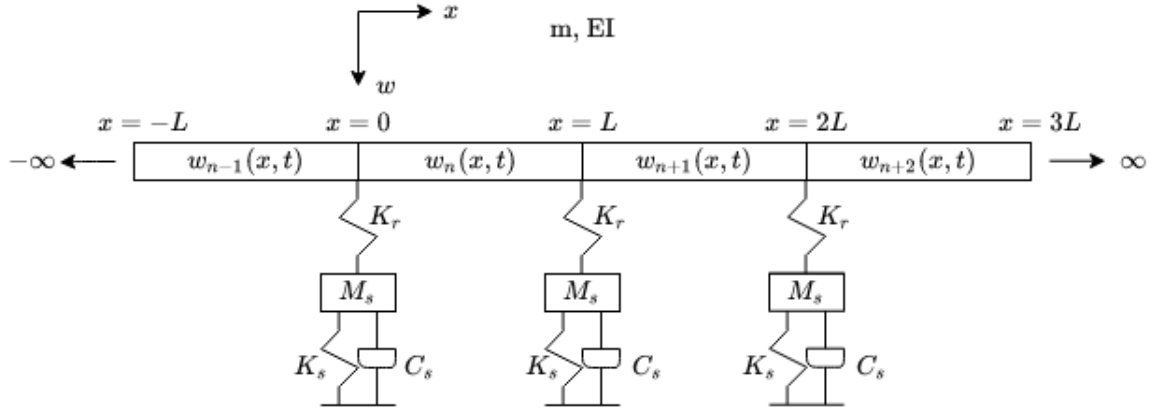
Figure B.2: Beam on periodic sleepers

$$K = \frac{-\omega^2 M_s + \mathrm{i}\omega C_s + K_s}{1 + \frac{-\omega^2 M_s + \mathrm{i}\omega C_s + K_s}{K_r}} \tag{B.2.1}$$

Where any differences come from the fact that Nordborg uses another definition of the temporal Fourier transform. The **K** and **H** matrices are as follows:

$$\mathbf{K} = \begin{bmatrix} 1 & 1 & 1 & 1 \\ -\mathrm{i}k & \mathrm{i}k & -k & k \\ \mathrm{i}EIk^3 & -\mathrm{i}EIk^3 & -EIk^3 & EIk^3 \\ EIk^2 & EIk^2 & -EIk^2 & -EIk^2 \end{bmatrix}$$

$$\mathbf{H} = \begin{bmatrix} \mathrm{e}^{\mathrm{i}kL} & \mathrm{e}^{-\mathrm{i}kL} & \mathrm{e}^{kL} & \mathrm{e}^{-kL} \\ -\mathrm{i}k\mathrm{e}^{\mathrm{i}kL} & \mathrm{i}k\mathrm{e}^{-\mathrm{i}kL} & -k\mathrm{e}^{kL} & k\mathrm{e}^{-kL} \\ \mathrm{i}EIk^3\mathrm{e}^{\mathrm{i}kL} + K\mathrm{e}^{\mathrm{i}kL} & -\mathrm{i}EIk^3\mathrm{e}^{-\mathrm{i}kL} + K\mathrm{e}^{-\mathrm{i}kL} & -EIk^3\mathrm{e}^{kL} + K\mathrm{e}^{kL} & EIk^3\mathrm{e}^{-kL} + K\mathrm{e}^{-kL} \\ EIk^2\mathrm{e}^{\mathrm{i}kL} & EIk^2\mathrm{e}^{-\mathrm{i}kL} & -EIk^2\mathrm{e}^{kL} & -EIk^2\mathrm{e}^{-kL} \end{bmatrix} \tag{B.2.2}$$

Calculating **T** gives:

$$\mathbf{T} = \begin{bmatrix} \frac{3\mathrm{e}^{\mathrm{i}kL}}{4} - \mathrm{i}Z_1 & \frac{\mathrm{e}^{-\mathrm{i}kL}}{4} - \mathrm{i}Z_2 & -\frac{\mathrm{i}\mathrm{e}^{\mathrm{i}kL}}{4} - \mathrm{i}Z_3 & \frac{\mathrm{i}\mathrm{e}^{-\mathrm{i}kL}}{4} - \mathrm{i}Z_4 \\ \frac{\mathrm{e}^{\mathrm{i}kL}}{4} + \mathrm{i}Z_1 & \frac{3\mathrm{e}^{-\mathrm{i}kL}}{4} + \mathrm{i}Z_2 & \frac{\mathrm{i}\mathrm{e}^{\mathrm{i}kL}}{4} + \mathrm{i}Z_3 & -\frac{\mathrm{e}^{-\mathrm{i}kL}}{4} + \mathrm{i}Z_4 \\ \frac{\mathrm{i}\mathrm{e}^{\mathrm{i}kL}}{4} - Z_1 & -\frac{\mathrm{i}\mathrm{e}^{-\mathrm{i}kL}}{4} - Z_2 & \frac{3\mathrm{e}^{\mathrm{i}kL}}{4} - Z_3 & \frac{\mathrm{e}^{-\mathrm{i}kL}}{4} - Z_4 \\ -\frac{\mathrm{i}\mathrm{e}^{\mathrm{i}kL}}{4} + Z_1 & \frac{\mathrm{i}\mathrm{e}^{-\mathrm{i}kL}}{4} + Z_2 & \frac{\mathrm{e}^{\mathrm{i}kL}}{4} + Z_3 & \frac{3\mathrm{e}^{-\mathrm{i}kL}}{4} + Z_4 \end{bmatrix} \tag{B.2.3}$$

With Z_i defined as follows:

$$Z_1 = \frac{\left(\mathrm{i}EIk^3\mathrm{e}^{\mathrm{i}kL} + K\mathrm{e}^{\mathrm{i}kL}\right)}{4EIk^3}, \quad Z_2 = \frac{\left(-\mathrm{i}EIk^3\mathrm{e}^{-\mathrm{i}kL} + K\mathrm{e}^{-\mathrm{i}kL}\right)}{4EIk^3}$$

$$Z_3 = \frac{\left(-Bk^3\mathrm{e}^{kL} + K\mathrm{e}^{kL}\right)}{4EIk^3}, \qquad Z_4 = \frac{\left(Bk^3\mathrm{e}^{-kL} + K\mathrm{e}^{-kL}\right)}{4EIk^3} \tag{B.2.4}$$

With the transfer matrix fully defined, we may continue now with calculating the propagation coefficients and the eigenvectors. First, we will analytically derive the dispersion equation. Calculating $\det\left(\mathbf{T} - e^{\lambda}\mathbf{I}\right)$, where $i\lambda L$ has been replaced with λ as to comply with the form in [51], converting the exponential functions to both hyperbolic and trigonometric functions, simplifying and solving for K gives:

$$K = \frac{4EIk^3(\cosh(\mu) - \cosh(kL))(\cosh(\lambda) - \cos(kL))}{(-\cosh(\lambda) + \cos(kL))\sinh(kL) + (\cosh(\lambda) - \cosh(kL))\sin(kL)} \tag{B.2.5}$$

Eq. B.2.5 may now be inverted, expanded and algebraically simplified:

$$\frac{1}{K} = \frac{(\cos(kL) - \cosh(\lambda))\sinh(kL) + (-\cosh(kL) + \cosh(\lambda))\sin(kL)}{4EIk^3(-\cosh(kL) + \cosh(\lambda))(-\cos(kL) + \cosh(\lambda))} \rightarrow$$

$$\frac{1}{K} = \frac{(\cos(kL) - \cosh(\lambda))\sinh(kL)}{4EIk^3(-\cosh(kL) + \cosh(\lambda))(-\cos(kL) + \cosh(\lambda))} + \frac{\cosh(\lambda))\sin(kL)}{4EIk^3(-\cosh(kL) + \cosh(\lambda))(-\cos(kL) + \cosh(\lambda))} \rightarrow$$

$$\frac{1}{K} = \frac{\sinh(kL)}{4EIk^3(\cosh(kL) - \cosh(\lambda))} - \frac{\sin(kL)}{4EIk^3(\cos(kL) - \cosh(\mu))} \rightarrow$$

$$-\frac{1}{K} = \frac{1}{4EIk^3}\left[\frac{\sin(kL)}{(\cos(kL) - \cosh(\lambda))} - \frac{\sinh(kL)}{(\cosh(kL) - \cosh(\lambda))}\right] \tag{B.2.6}$$

As one can see from Eq. B.2.6d and Eq. 11 from [51], the equations are a perfect match. Giving our first confirmation that the method with the transfer matrix gives correct results.

The roots of the dispersion equation (Eq. B.2.6d), and thus the propagation coefficients, may be found by employing a root-finder. Otherwise, exploiting the fact that the propagation constants are effectively eigenvalues of the matrix $\mathbf{T}$, one can also use an eigenvalue solver from any programme (Matlab in this case). By choosing the latter method, we circumvent any problems related with numerically finding the roots of the equation.
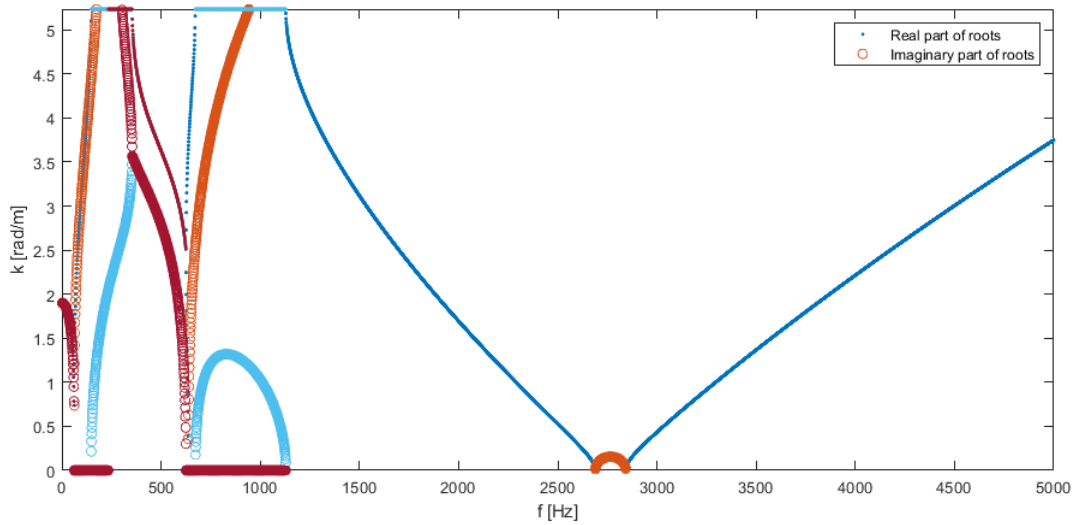
Figure B.3: Propagation coefficients

The results may be found in Fig. B.3, of which only the positive values of k are given. Note that the values of k are actually the propagation constants λ. Furthermore, keep in mind that the imaginary parts may be larger than the limit of $\frac{\pi}{L}$, as those are not limited by the periodicity of the structure.

One can clearly observe a complex band of waves in the frequency range of $f \approx 354 - 625$Hz ascociated with local resonance. Also, between $f \approx 625 - 635$Hz there exists a PP-band, whilst above that there exists a attenuation-band (second stop-band from [20]). We can go further into details of the various bands that exist, however that discussion is abundant in literature and thus will not be repeated here.

Therefore, we continue our discussion with a comparison. If only the propagation constants that dictate free wave propagation are plotted (i.e. with $\text{Im}\{\lambda_i\} = 0$), one can make a comparison with [20]. As those results were exactly matched by those from [51], the latter will be used to make the comparison with our own results (see Fig. B.4).
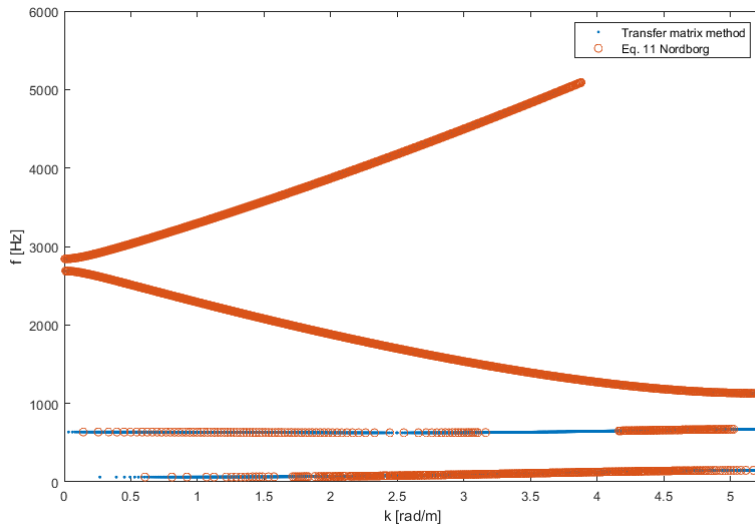
Figure B.4: Comparison results Nordborg and transfer matrix method

As one can see, the results match perfectly. In contrary to Fig. B.3 the attenuation- and propagation bands are now clearly distinghuished as well. Another check is by calculating the propagation coefficients for a certain frequency, say: $f = 1540$ Hz (as is done in [20]), this gives the following:

$$\begin{aligned}
\lambda_1 &= -7.538\text{i} \\
\lambda_2 &= -2.986 \\
\lambda_3 &= +2.986 \\
\lambda_4 &= +7.53\text{i}
\end{aligned} \tag{B.2.7}$$

As one can see from Eq. B.2.7, λ_2 and λ_3 comply very well with the third mode for $k = 3$ as defined in [20]. Thus we have verified the Transfer Matrix Method.

B.3 Analytical Greens function

In this section we will show how to derive Green's function for a periodic structure, with the help of the Bloch wave solution from the start of this Appendix. To the authors knowledge, only Nordborg [51] made a symbolic derivation of Green's function for a periodic system for which the latter then later altered to allow for a moving load [50]. Watanabe [65] also made a symbolic derivation of equation for the Bloch wave functions, for which he derived the eigenvectors of the constants as well. Mead did derive the solution to a pointforce harmonic excitation [39], however with a flexural wave approach. This approach is rather interesting, since it is very intuitive and thus is a recommended read. Others, whom will become clear in Chapter 2.2.3, derived the forced response for a moving load based on the Floquet Transform.

We will go over the complete derivation, as to show every step. Hereby we will derive the eigenvectors of the constants as well as to have a complete solution to the problem. The full mathematical formulation of a periodic beam supported on equidistant springs[1] is as follows:

$$EIw''''(x,t) + m\ddot{w}(x,t) + K_s w(x,t) \sum_{n=-\infty}^{\infty} \delta(x-nL) = \delta(x-x0)\delta(t) \tag{B.3.1}$$

Applying a temporal Fourier transform as defined in Eq. 2.2.9 to the equation above leads to:

$$W''''(x,\omega) - k^4 W(x,\omega) + KW(x,\omega)\sum_{n=-\infty}^{\infty} \delta(x-nL) = \delta(x-x_0),$$

$$k = \sqrt[4]{\frac{m\omega^2}{EI}} \tag{B.3.2}$$

Now, Eq. B.3.2 is a periodic system with period L, where the support conditions are given by the infinite periodic sum. Here, the infinite sum of delta functions will make the structure periodic and thus allows us to use the method of the Transfer Matrix as defined in section 2.2.2. As the transfer matrix of this problem is the same as in Eq. B.2.3, we can use that one and write it as in Eq. 2.2.15 for an arbitrary propagation constant λ_i and eigenvector $\underline{A_i}$:

$$\begin{bmatrix} \frac{3e^{ikL}}{4} - iZ_1 - e^{i\lambda_i L} & \frac{e^{-ikL}}{4} - iZ_2 & -\frac{ie^{ikL}}{4} - iZ_3 & \frac{ie^{-ikL}}{4} - iZ_4 \\ \frac{e^{ikL}}{4} + iZ_1 & \frac{3e^{-ikL}}{4} + iZ_2 - e^{i\lambda_i L} & \frac{ie^{ikL}}{4} + iZ_3 & -\frac{e^{-ikL}}{4} + iZ_4 \\ \frac{ie^{ikL}}{4} - Z_1 & -\frac{ie^{-ikL}}{4} - Z_2 & \frac{3e^{ikL}}{4} - Z_3 - e^{i\lambda_i L} & \frac{e^{-ikL}}{4} - Z_4 \\ -\frac{ie^{ikL}}{4} + Z_1 & \frac{ie^{-ikL}}{4} + Z_2 & \frac{e^{ikL}}{4} + Z_3 & \frac{3e^{-ikL}}{4} + Z_4 - e^{i\lambda_i L} \end{bmatrix} \begin{bmatrix} A_i \\ B_i \\ C_i \\ D_i \end{bmatrix} \tag{B.3.3}$$

Adding the first two rows of Eq. B.3.3 and solving for the constant B_i gives us:

$$B_i e^{-ikL} + (-A_i - B_i)e^{i\lambda_i L} + A_i e^{ikL} \rightarrow$$

$$B_i = \frac{A_i(e^{ikL} - e^{i\lambda_i L})}{-e^{-ikL} + e^{i\lambda_i L}} \tag{B.3.4}$$

Multiplying the first row by i, adding the third row, and solving for C_i leads to:

---

[1]Of course, the spring may be replaced by a dynamic stiffness in the frequency domain as well.

$$(-\mathrm{i}A_i - C_i)\mathrm{e}^{\mathrm{i}\lambda_i L} + \mathrm{i}A_i\mathrm{e}^{\mathrm{i}kL} + C_i\mathrm{e}^{kL} \rightarrow$$

$$C_i = \frac{\mathrm{i}A_i(\mathrm{e}^{\mathrm{i}kL} - \mathrm{e}^{\mathrm{i}\lambda_i L})}{-\mathrm{e}^{kL} + \mathrm{e}^{\mathrm{i}\lambda_i L}}$$

(B.3.5)

Multiplying the fourth row by i, adding the first row and solving for D_i leads to:

$$(-A_i - \mathrm{i}D_i)\mathrm{e}^{\mathrm{i}\lambda_i L} + \mathrm{i}D_i\mathrm{e}^{-kL} + A_i\mathrm{e}^{\mathrm{i}kL} \rightarrow$$

$$D_i = \frac{-\mathrm{i}A_i(\mathrm{e}^{\mathrm{i}kL} - \mathrm{e}^{\mathrm{i}\lambda_i L})}{\mathrm{e}^{\mathrm{i}\lambda_i L} - \mathrm{e}^{-kL}}$$

(B.3.6)

Now, all that is left is to choose a function for the value A_i. In this choice we are free to do whatever we like, though it is useful to choose something that will simplify the equations above. Hence:

$$
\begin{aligned}
A_i &= \mathrm{i}(-\mathrm{e}^{-\mathrm{i}kL} + \mathrm{e}^{\mathrm{i}\lambda_i L})(-\mathrm{e}^{kL} + \mathrm{e}^{\mathrm{i}\lambda_i L})(\mathrm{e}^{\mathrm{i}\lambda_i L} - \mathrm{e}^{-kL}) \rightarrow \\
B_i &= \mathrm{i}\left(-\mathrm{e}^{kL} + \mathrm{e}^{\mathrm{i}\lambda_i L}\right)\left(\mathrm{e}^{\mathrm{i}\lambda_i L} - \mathrm{e}^{-kL}\right)\left(\mathrm{e}^{\mathrm{i}kL} - \mathrm{e}^{\mathrm{i}\lambda_i L}\right) \\
C_i &= -\left(-\mathrm{e}^{-\mathrm{i}kL} + \mathrm{e}^{\mathrm{i}\lambda_i L}\right)\left(\mathrm{e}^{\mathrm{i}\lambda_i L} - \mathrm{e}^{-kL}\right)\left(\mathrm{e}^{\mathrm{i}kL} - \mathrm{e}^{\mathrm{i}\lambda_i L}\right) \\
D_i &= \left(-\mathrm{e}^{-\mathrm{i}kL} + \mathrm{e}^{\mathrm{i}\lambda_i L}\right)\left(-\mathrm{e}^{kL} + \mathrm{e}^{\mathrm{i}\lambda_i L}\right)\left(\mathrm{e}^{\mathrm{i}kL} - \mathrm{e}^{\mathrm{i}\lambda_i L}\right)
\end{aligned}
$$

(B.3.7)

With Eq. B.3.7 we can populate the solution as follows:

$$W_r(x, \lambda, \omega) = \sum_{i=1}^{2} \alpha_{i,r}\underline{E}(x, \omega)\underline{A}_{i,r}(\lambda_i, \omega),$$

$$W_l(x, \lambda, \omega) = \sum_{i=1}^{2} \alpha_{i,l}\underline{E}(x, \omega)\underline{A}_{i,l}(\lambda_i, \omega)$$

(B.3.8)

and thus solve for the constants α_i by writing the boundary conditions at position x_0 in the elementary cell:

$$W_r(x_0, \lambda, \omega) - W_l(x_0, \lambda, \omega) = 0, \qquad W_r'(x_0, \lambda, \omega) - W_l'(x_0, \lambda, \omega) = 0,$$

$$W_r''(x_0, \lambda, \omega) - W_l''(x_0, \lambda, \omega) = 0, \quad W_r'''(x_0, \lambda, \omega) - W_l'''(x_0, \lambda, \omega) = \frac{1}{EI}$$

(B.3.9)

Now, Eq. B.3.9 may be easily solved for the unknown constants α_i with which the solution to Eq. B.3.2 is fully determined. With the Greens function determined one is now able to solve for any type of loading, with the sidenote that it will not always be possible to do so analytically.

Appendix C

Simple derivation Floquet Transform

As [17] and [11] does not give satisfactory results on their own, and it was not clear what was done in the latter paper, we will derive the response based on the former ourselves.

We will start by using Eq. 2.2.19 as before:

$$\hat{U}(x_0, \omega) = \int_\infty^\infty \hat{F}(x,\omega)\hat{G}(x_0, x, \omega)dx$$

For our case, we have a constant load traveling at a velocity V along the structure, its Fourier transform is then given as:

$$\hat{F}(x_0, \omega) = \int_{-\infty}^\infty \delta(x_0 - Vt)e^{-i\omega t}dt = \frac{1}{V}e^{-i\frac{\omega}{V}x_0} \tag{C.0.1}$$

Let us substitute Eq. C.0.1 into Eq. 2.2.19 and rewrite the infinite integral as an infinite sum of integrals:

$$\hat{U}(x, \omega) = \frac{1}{V}\sum_{n=-\infty}^\infty \int_{nL}^{(n+1)L} e^{-i\frac{\omega}{V}x_0}\hat{G}(x, x_0, \omega)dx_0 \tag{C.0.2}$$

Now, due to the reciprocity property of the Green's function, we can also calculate the response at x_0 due to a force at x. Therefore: $\hat{G}(x, x_0, \omega) = \hat{G}(x_0, x, \omega)$ and $\hat{U}(x, \omega) \to \hat{U}(x_0, \omega)$. Therefore, we interchange the variables x, x_0:

$$\hat{U}(x_0, \omega) = \frac{1}{V}\sum_{n=-\infty}^\infty \int_{nL}^{(n+1)L} e^{-i\frac{\omega}{V}x}\hat{G}(x_0, x, \omega)dx \tag{C.0.3}$$

We can make a change of variables by substituting $\tilde{x} = x - nL$:

$$\hat{U}(x_0, \omega) = \frac{1}{V}\sum_{n=-\infty}^\infty \int_0^L e^{-i\frac{\omega}{V}(\tilde{x}+nL)}\hat{G}(x_0, \tilde{x} + nL, \omega)d\tilde{x} \tag{C.0.4}$$

Re-arranging terms gives:

$$\hat{U}(x, x_0, \omega) = \frac{1}{V} \int_0^L e^{-i\frac{\omega}{V}\tilde{x}} \sum_{n=-\infty}^{\infty} e^{-in\frac{\omega}{V}L} \hat{G}(x_0, \tilde{x} + nL, \omega) d\tilde{x} \tag{C.0.5}$$

Realising that the Floquet transform of any function is defined by [17]:

$$\bar{f}(x, \kappa) = \sum_{n=-\infty}^{\infty} f(x + nL) e^{in\kappa L} \tag{C.0.6}$$

Such that Eq. C.0.5 may be rewritten as:

$$\hat{U}(x_0, \omega) = \frac{1}{V} \int_0^L e^{-i\frac{\omega}{V}\tilde{x}} \bar{\hat{G}}(x_0, \tilde{x}, \kappa, \omega) d\tilde{x} \tag{C.0.7}$$

Where $\kappa = -\frac{\omega}{V} - \frac{2\pi m}{L}$, with m any integer such that $\kappa = [-\frac{\pi}{L}, \frac{\pi}{L}]$. To calculate the time-domain response one now simply uses the inverse Fourier transform on Eq. C.0.7.

Appendix D

Accuracy Analysis Numerical Integration

In this appendix we will show the result of the accuracy analysis conducted to find faster ways to perform the numerical integration by which we obtain the Fourier coefficients. In Fig. D.1 one can see the results of this comparison. As can be seen, by the large closed squares, all the results lay on top of each other. Of course, if we zoom in we would see small discrepancies. However, as these discrepancies between the results are very small this will not matter.

All instability domains in Chapters 4, 5, and 6 are thus calculated with the model by Barbosa [20], together with Appendix E.
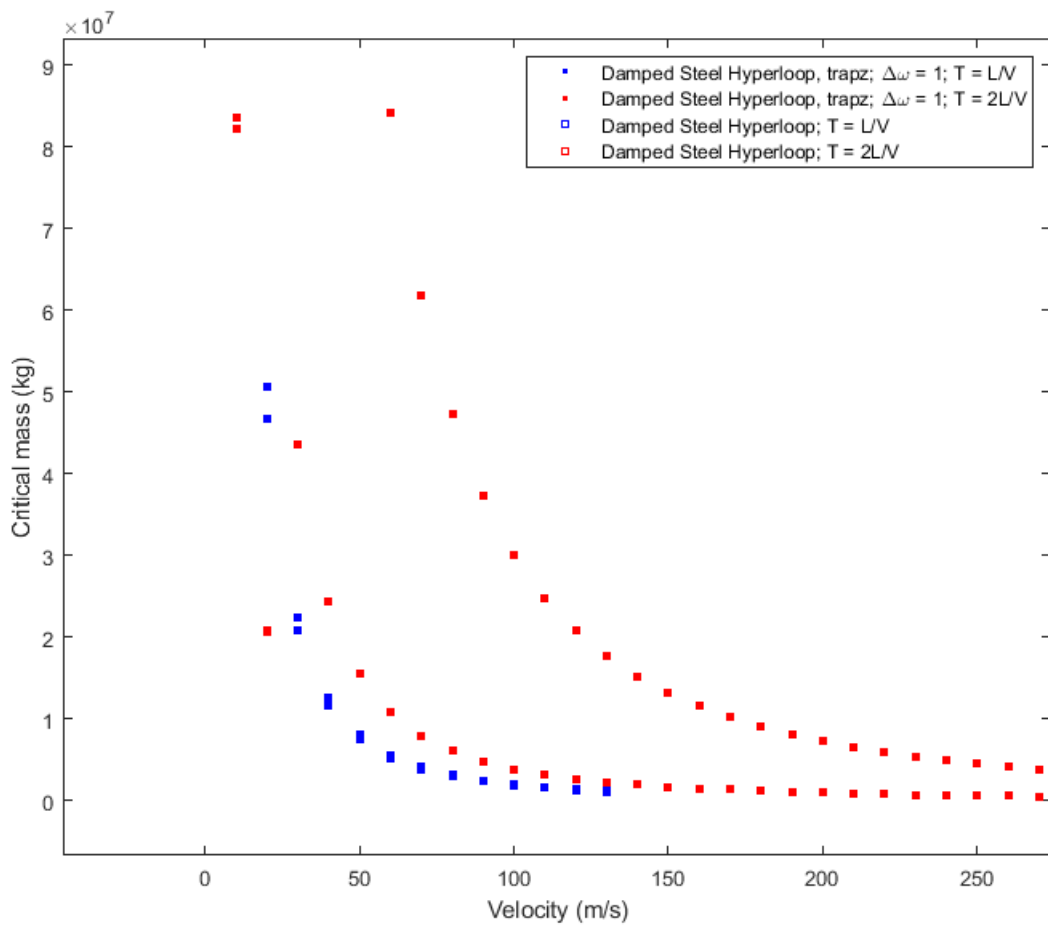
Figure D.1: Accuracy analysis

Appendix E

Derivation time-domain response under the moving load

1. Time domain response of the rail under the load

According to our paper, the response of the rail due to a moving load of the type $f(x,t) = F_0 \delta(x - Vt) e^{i\omega_0 t}$ can be written as

$$\tilde{u}(x, \omega, \omega_0) = \frac{F_0}{V\left[\left(\frac{\omega - \omega_0}{V}\right)^4 EI - \omega^2 m\right]} e^{-i\frac{\omega - \omega_0}{V}x} + \frac{i\, c\left(i\bar{k}, \frac{\omega - \omega_0}{V}, -x\right) + c\left(\bar{k}, \frac{\omega - \omega_0}{V}, -x\right)}{4EI\bar{k}^3} \tilde{f}$$

$$- \frac{d\left(i\bar{k}, \frac{\omega - \omega_0}{V}, -x\right) - d\left(\bar{k}, \frac{\omega - \omega_0}{V}, -x\right)}{4EI\bar{k}^2} \tilde{m}$$

(1)

where $\bar{k} = \sqrt[4]{\omega^2 m / EI}$, the frequency dependent force $\tilde{f}$ and moment $\tilde{m}$ are obtained via the system

$$\begin{bmatrix} \tilde{f} \\ \tilde{m} \end{bmatrix} = \frac{F_0}{V\left[\left(\frac{\omega - \omega_0}{V}\right)^4 EI - \omega^2 m\right]} \begin{bmatrix} \mathbf{O}_{N \times 2} \\ 1 \quad 0 \\ 0 \quad 1 \end{bmatrix}^{\mathrm{T}} \left[\tilde{\mathbf{U}}\left(\frac{\omega - \omega_0}{V}\right) + \mathbf{E}\right]^{-1} \begin{bmatrix} \mathbf{O}_{N \times 1} \\ 1 \\ -i\frac{\omega - \omega_0}{V} \end{bmatrix}$$

(2)

(expressions for $\tilde{\mathbf{U}}\left(\frac{\omega - \omega_0}{V}\right)$ and $\mathbf{E}$ can be found in [1]) and where the variables $c(k_1, k_2, x)$ and $d(k_1, k_2, x)$ are given by

$$c(k_1, k_2, x) = e^{ik_2 L(X+1)} \left(\frac{e^{k_1(x - XL)}}{e^{k_1 L} - e^{ik_2 L}} - \frac{e^{-k_1(x - XL)}}{e^{-k_1 L} - e^{ik_2 L}} \right)$$

(3)

$$d(k_1, k_2, x) = e^{ik_2 L(X+1)} \left(\frac{e^{k_1(x - XL)}}{e^{k_1 L} - e^{ik_2 L}} + \frac{e^{-k_1(x - XL)}}{e^{-k_1 L} - e^{ik_2 L}} \right)$$

(4)

($X = \text{floor}(x/L)$ is the rounding down of x/L towards $-\infty$; L is the distance between sleepers – centre to centre). Eq. (1) can be rewritten in the more convenient form

$$\tilde{u}(x, \omega, \omega_0) = A_0 e^{-i\frac{\omega - \omega_0}{V}x} + \sum_{j=1}^{4} A_j e^{i\frac{\omega - \omega_0}{V}\left(\text{floor}\left(\frac{-x}{L}\right)L + L\right)} e^{i^j \bar{k}\left(-x - \text{floor}\left(\frac{-x}{L}\right)L\right)}$$

(5)

where

$$A_0 = \frac{F_0}{V\left[\left(\frac{\omega - \omega_0}{V}\right)^4 EI - \omega^2 m\right]}$$

(6)

$$A_{j=1,2,3,4} = \frac{i^j \tilde{f} + (-1)^j \bar{k}\tilde{m}}{4EI\bar{k}^3} \frac{1}{e^{i^j \bar{k}L} - e^{i\frac{\omega - \omega_0}{V}L}}$$

The time domain displacement of the rail below the load, i.e., $w(t, \omega_0) = u(x = Vt, t, \omega_0)$ is

$$w(t,\omega_0) = u(x=Vt,t,\omega_0) = \frac{1}{2\pi}\int_{-\infty}^{+\infty}\tilde{u}(Vt,\omega,\omega_0)e^{i\omega t}d\omega =$$

$$\frac{e^{i\omega_0 t}}{2\pi}\int_{-\infty}^{+\infty}A_0 d\omega + \frac{1}{2\pi}\sum_{j=1}^{4}\int_{-\infty}^{+\infty}A_j e^{i\frac{\omega-\omega_0}{V}\left(\text{floor}\left(\frac{-Vt}{L}\right)L+L\right)}e^{i^j\bar{k}\left(-Vt-\text{floor}\left(\frac{-Vt}{L}\right)L\right)}e^{i\omega t}d\omega = \tag{7}$$

$$\frac{e^{i\omega_0 t}}{2\pi}\int_{-\infty}^{+\infty}A_0 d\omega + \frac{1}{2\pi}\sum_{j=1}^{4}\int_{-\infty}^{+\infty}A_j e^{i\frac{\omega-\omega_0}{V}\left(-\text{ceil}\left(\frac{Vt}{L}\right)L+L\right)}e^{i^j\bar{k}\left(\text{ceil}\left(\frac{Vt}{L}\right)L-Vt\right)}e^{i\omega t}d\omega$$

and if we define the integer variable $l = \text{ceil}(Vt/L) = -\text{floor}(-Vt/L)$ (l represents the cell number), then

$$w(t,\omega_0) = \frac{e^{i\omega_0 t}}{2\pi}\int_{-\infty}^{+\infty}A_0 d\omega + \frac{1}{2\pi}\sum_{j=1}^{4}\int_{-\infty}^{+\infty}A_j e^{i\frac{\omega-\omega_0}{V}L(1-l)}e^{i^j\bar{k}(lL-Vt)}e^{i\omega t}d\omega \tag{8}$$

After some manipulation (a lot actually, see appendix), eq. (8) can be rewritten as

$$w(t,\omega_0) = \sum_{k=-\infty}^{+\infty}\tilde{u}_k(\omega_0)e^{i\left(\omega_0 - k\frac{2\pi V}{L}\right)t} \tag{9}$$

where

$$\tilde{u}_k(\omega_0) = \frac{1}{2\pi}\left(\delta_{k0}\int_{-\infty}^{+\infty}A_0 d\omega + \frac{V}{L}\sum_{j=1}^{4}\int_{-\infty}^{+\infty}A_j \frac{e^{i\frac{\omega-\omega_0}{V}L+2\pi ik}-e^{i^j\bar{k}L}}{-i^j\bar{k}V+i\omega-i\left(\omega_0-k\frac{2\pi V}{L}\right)}d\omega\right) \tag{10}$$

(after inserting the values of Aj and some manipulation … should be convergent for real w0, and k; the factor with exponents goes to -1 when $e^{i^j\bar{k}L}$ goes to infinite, and so the integrand decays with w^2 as w goes to infinite)

$$\tilde{u}_k(\omega_0) = \frac{1}{2\pi}\left(\delta_{k0}\int_{-\infty}^{+\infty}\frac{F_0}{V\left[\left(\frac{\omega-\omega_0}{V}\right)^4 EI - \omega^2 m\right]}d\omega + \right.$$

$$\left. \frac{V}{4EIL}\sum_{j=1}^{4}\int_{-\infty}^{+\infty}\frac{i^j\tilde{f}+(-1)^j\bar{k}\tilde{m}}{-i^j\bar{k}^4 V + i\omega\bar{k}^3 - i\omega_0\bar{k}^3 + ik\frac{2\pi V}{L}\bar{k}^3}\frac{e^{\left(i\frac{\omega-\omega_0}{V}L+2\pi ik\right)}-e^{i^j\bar{k}L}}{e^{i^j\bar{k}L}-e^{i\frac{\omega-\omega_0}{V}L}}d\omega\right)$$

2. Interaction with oscillator

Based on eq. (9), if an oscillator is moving at constant speed V on top of the railway structure, and if it is considered that the only external excitation is its own weight, then its response is going to be driven by harmonics whose frequencies are $\omega_j = j\frac{2\pi V}{L}\,(j=-\infty...+\infty)$. If there are other perturbations (in the shape of irregularities between the oscillator and the rail or in the shape of external forces acting on the oscillator), then extra harmonics of the type $\omega_{\alpha l} = \omega_\alpha + l\frac{2\pi V}{L}\,(l=-\infty...+\infty)$ will also show in the response, where ω_α is a fundamental frequency

that can assume any value between 0 and $\frac{2\pi V}{L}$. In any case, from eq. (9) it can be inferred that each fundamental harmonic ω_α will only excite itself and the higher (or lower) harmonics given $\omega_{\alpha l}$, and thus the system can be solved separately for distinct values of ω_α.

Assuming only the self-weight as external excitation, the steady-state displacement of the oscillator $u_{cp}(t)$ (at the contact point) can be given by

$$u_{cp}(t) = \sum_{j=-\infty}^{+\infty} \tilde{F}_j \tilde{h}_j e^{ij\frac{2\pi V}{L}t} \tag{11}$$

where $\tilde{F}_j$ is the amplitude of the contact force for the jth harmonic (for $j=0$, static, $\tilde{F}_j$ is the total weight carried by the oscillator; for the other harmonics, the contact force is unknown for the time being) and $\tilde{h}_j$ is the transfer function for the jth harmonic of the oscillator (displacement at contact point due to force at the contact point). If the oscillator is simply a rigid mass m, then

$$\tilde{h}_j = -L^2 \big/ \left(4 j^2 \pi^2 V^2 m\right) \tag{12}$$

On the other hand, the displacement of the rail at the contact point can be calculating by adding the contribution of all harmonics as well, and so we obtain

$$w(t) = \sum_{j=-\infty}^{+\infty} -F_j w\left(t, j\frac{2\pi V}{L}\right) = \sum_{j=-\infty}^{+\infty} -F_j \sum_{k=-\infty}^{+\infty} \underbrace{\tilde{u}_k\left(j\frac{2\pi V}{L}\right) e^{i\left(j\frac{2\pi V}{L} - k\frac{2\pi V}{L}\right)t}}_{\tilde{u}_{k,j}}$$

$$= \sum_{j=-\infty}^{+\infty} -F_j \sum_{k=-\infty}^{+\infty} \tilde{u}_{k,j} e^{i(j-k)\frac{2\pi V}{L}t} \tag{13}$$

By imposing that the displacement of the oscillator $u_{cp}(t)$ must equal the displacement of the rail $w(t)$, we obtain the equality

$$\sum_{j=-\infty}^{+\infty} \tilde{F}_j \tilde{h}_j e^{ij\frac{2\pi V}{L}t} = \sum_{j=-\infty}^{+\infty} -F_j \sum_{k=-\infty}^{+\infty} \tilde{u}_{k,j} e^{i(j-k)\frac{2\pi V}{L}t} \tag{14}$$

which can be solved by harmonic balance (balance of all the terms containing the lth harmonic):

$$\tilde{F}_l \tilde{h}_l = \sum_{j=-\infty}^{+\infty} -\tilde{F}_j \tilde{u}_{k=j-l,j} \tag{15}$$

After truncating the summation in j (going from −N to N), eq. (15) can be rewritten in the matrix form

$$(\mathbf{H} + \mathbf{U})\mathbf{f} = \mathbf{0} \tag{16}$$

where

$$\mathbf{H} = \begin{bmatrix} \tilde{h}_{-N} & & \\ & \ddots & \\ & & \tilde{h}_{N} \end{bmatrix}, \quad \mathbf{U} = \begin{bmatrix} \tilde{u}_{0,-N} & \cdots & \tilde{u}_{2N,N} \\ \vdots & \ddots & \vdots \\ \tilde{u}_{-2N,-N} & \cdots & \tilde{u}_{0,N} \end{bmatrix} \begin{matrix} \overset{(+1,+1)}{\rightarrow} \\ \downarrow (-1,+0) \end{matrix}, \quad \mathbf{f} = \begin{bmatrix} \tilde{F}_{-N} \\ \vdots \\ \tilde{F}_{N} \end{bmatrix} \tag{17}$$

Since $\tilde{F}_0$ is known, system (16) can be solved for the remaining force components.

Appendix – manipulation of eq. (9)

The Fourier transform of eq. (9) is

$$\tilde{w}(\bar{\omega}, \omega_0) = \int_{-\infty}^{+\infty} w(t, \omega_0) e^{-i\bar{\omega}t} dt =$$

$$\int_{-\infty}^{+\infty} \frac{e^{i(\omega_0 - \bar{\omega})t}}{2\pi} dt \int_{-\infty}^{+\infty} A_0 d\omega + \frac{1}{2\pi} \sum_{j=1}^{4} \int_{-\infty}^{+\infty} \int_{-\infty}^{+\infty} A_j e^{i\frac{\omega - \omega_0}{V}L(1-l)} e^{i^j\bar{k}(lL-Vt)} e^{i\omega t} d\omega e^{-i\bar{\omega}t} dt \tag{18}$$

After the order of integration is changed, it is obtained

$$\tilde{w}(\bar{\omega}, \omega_0) = \int_{-\infty}^{+\infty} \frac{e^{i(\omega_0 - \bar{\omega})t}}{2\pi} dt \int_{-\infty}^{+\infty} A_0 d\omega + \frac{1}{2\pi} \sum_{j=1}^{4} \int_{-\infty}^{+\infty} A_j \int_{-\infty}^{+\infty} e^{i\frac{\omega - \omega_0}{V}L(1-l)} e^{i^j\bar{k}(lL-Vt)} e^{i(\omega - \bar{\omega})t} dt d\omega \tag{19}$$

The integer variable l is time dependent and varies in a stepwise fashion. Thus, it is convenient to divide the time integral into smaller integrals defined by the time intervals $t = (l-1)L/V + \tau$, with $0 < \tau < L/V$. In each of these time intervals, l remains constant. The new equation for $\tilde{u}(Vt, \bar{\omega})$ is

$$\tilde{w}(\bar{\omega}, \omega_0) = \int_{-\infty}^{+\infty} \frac{e^{i(\omega_0 - \bar{\omega})t}}{2\pi} dt \int_{-\infty}^{+\infty} A_0 d\omega +$$

$$\frac{1}{2\pi} \sum_{j=1}^{4} \int_{-\infty}^{+\infty} A_j \sum_{l=-\infty}^{+\infty} e^{i\frac{\omega - \omega_0}{V}L(1-l)} \int_{0}^{L/V} e^{i^j\bar{k}(L-V\tau)} e^{i(\omega - \bar{\omega})(\tau + (l-1)L/V)} d\tau d\omega \tag{20}$$

and because the summation goes from minus infinity to plus infinity, l can be shifted to the left or right, thus obtaining the more convenient expression ($\bar{l} = l - 1$)

$$\tilde{w}(\bar{\omega}, \omega_0) = \int_{-\infty}^{+\infty} \frac{e^{i(\omega_0 - \bar{\omega})t}}{2\pi} dt \int_{-\infty}^{+\infty} A_0 d\omega +$$

$$\frac{1}{2\pi} \sum_{j=1}^{4} \int_{-\infty}^{+\infty} A_j \sum_{\bar{l}=-\infty}^{+\infty} e^{-i\frac{\omega - \omega_0}{V}L\bar{l}} \int_{0}^{L/V} e^{i^j\bar{k}(L-V\tau)} e^{i(\omega - \bar{\omega})(\tau + \bar{l}L/V)} d\tau d\omega \tag{21}$$

The factors that do not depend on τ can be moved outside the integral over that variable:

$$\tilde{w}(\bar{\omega}, \omega_0) = \int\limits_{-\infty}^{+\infty} \frac{e^{i(\omega_0 - \bar{\omega})t}}{2\pi} \, dt \int\limits_{-\infty}^{+\infty} A_0 \, d\omega +$$

$$\frac{1}{2\pi} \sum_{j=1}^{4} \int\limits_{-\infty}^{+\infty} A_j \sum_{\bar{l}=-\infty}^{+\infty} e^{\left(-i\frac{\omega-\omega_0}{V} L\bar{l} + i^j \bar{k} L + i(\omega-\bar{\omega})\bar{l} L/V\right)} \int\limits_{0}^{L/V} e^{\left(-i^j \bar{k} V + i\omega - i\bar{\omega}\right)\tau} \, d\tau \, d\omega \tag{22}$$

the factors that do not depend on $\bar{l}$ can be moved outside the summation over that variable:

$$\tilde{w}(\bar{\omega}, \omega_0) = \int\limits_{-\infty}^{+\infty} \frac{e^{i(\omega_0 - \bar{\omega})t}}{2\pi} \, dt \int\limits_{-\infty}^{+\infty} A_0 \, d\omega +$$

$$\frac{1}{2\pi} \sum_{j=1}^{4} \int\limits_{-\infty}^{+\infty} A_j e^{i^j \bar{k} L} \sum_{\bar{l}=-\infty}^{+\infty} e^{i(\omega_0 - \bar{\omega})\frac{L}{V}\bar{l}} \int\limits_{0}^{L/V} e^{\left(-i^j \bar{k} V + i\omega - i\bar{\omega}\right)\tau} \, d\tau \, d\omega \tag{23}$$

and the factors that do not depend on ω can be moved outside the integral over that variable:

$$\tilde{w}(\bar{\omega}, \omega_0) = \int\limits_{-\infty}^{+\infty} \frac{e^{i(\omega_0 - \bar{\omega})t}}{2\pi} \, dt \int\limits_{-\infty}^{+\infty} A_0 \, d\omega +$$

$$\frac{1}{2\pi} \left(\sum_{\bar{l}=-\infty}^{+\infty} e^{i(\omega_0 - \bar{\omega})\frac{L}{V}\bar{l}} \right) \sum_{j=1}^{4} \int\limits_{-\infty}^{+\infty} A_j e^{i^j \bar{k} L} \int\limits_{0}^{L/V} e^{\left(-i^j \bar{k} V + i\omega - i\bar{\omega}\right)\tau} \, d\tau \, d\omega \tag{24}$$

The integrals over τ only contains an exponential function and so can be evaluated analytically:

$$\tilde{w}(\bar{\omega}, \omega_0) = \delta(\omega_0 - \bar{\omega}) \int\limits_{-\infty}^{+\infty} A_0 \, d\omega +$$

$$\frac{1}{2\pi} \left(\sum_{\bar{l}=-\infty}^{+\infty} e^{i(\omega_0 - \bar{\omega})\frac{L}{V}\bar{l}} \right) \sum_{j=1}^{4} \int\limits_{-\infty}^{+\infty} A_j e^{i^j \bar{k} L} \frac{\left(e^{\left(-i^j \bar{k} V + i\omega - i\bar{\omega}\right)\frac{L}{V}} - 1 \right)}{-i^j \bar{k} V + i\omega - i\bar{\omega}} \, d\omega \tag{25}$$

and so does the summation over l (Dirac comb):

$$\tilde{w}(\bar{\omega}, \omega_0) = \delta(\omega_0 - \bar{\omega}) \int\limits_{-\infty}^{+\infty} A_0 \, d\omega +$$

$$\frac{V}{L} \sum_{k=-\infty}^{+\infty} \delta\left(\omega_0 - \bar{\omega} - k \frac{2\pi V}{L} \right) \sum_{j=1}^{4} \int\limits_{-\infty}^{+\infty} A_j \frac{e^{i\frac{\omega - i\bar{\omega}}{V} L} - e^{i^j \bar{k} L}}{-i^j \bar{k} V + i\omega - i\bar{\omega}} \, d\omega \tag{26}$$

Eq. (26) shows that the response below the load is composed by the harmonics $\omega_0 - k \dfrac{2\pi V}{L}$, and it

time counterpart is written as

$$w(t, \omega_0) = \frac{1}{2\pi} \int\limits_{-\infty}^{+\infty} \tilde{w}(\bar{\omega}) e^{i\bar{\omega}t} d\bar{\omega} =$$

$$\frac{e^{i\omega_0 t}}{2\pi} \int\limits_{-\infty}^{+\infty} A_0 d\omega +$$

$$\sum_{k=-\infty}^{+\infty} \frac{V e^{i\left(\omega_0 - k\frac{2\pi V}{L}\right)t}}{2\pi L} \sum_{j=1}^{4} \int\limits_{-\infty}^{+\infty} A_j \frac{e^{i\frac{\omega-\omega_0}{V}L + 2\pi i k} - e^{i^j \bar{k} L}}{-i^j \bar{k} V + i\omega - i\left(\omega_0 - k\frac{2\pi V}{L}\right)} d\omega$$

(27)

Appendix F

Non-dimensional Dispersion analysis of several periodic structures

F.1 Non-dimensionalisation

In the following two sections we will define and derive the non-dimensional framework we will be working in.

F.1.1 Non-dimensional Euler-Bernoulli beam

Let us first derive the non-dimensional EB equation. Define the following non-dimensional variables:

$$\tilde{w} = \frac{w}{L}, \quad \tilde{x} = \frac{x}{L}, \quad \tilde{t} = \omega_n t \qquad (\text{F.1.1})$$

Substituting F.1.1 into Eq. 2.2.7, leads to:

$$\tilde{w}''''(\tilde{x}, \tilde{t}) + \frac{m\tilde{L}^4}{EI}\omega_n^2 \ddot{\tilde{w}}(\tilde{x}, \tilde{t}) = 0 \qquad (\text{F.1.2})$$

setting $\tilde{L} = L$, with L the length of one periodic element, and $\omega_n^2 = \frac{EI}{mL^4}$ ensures a non-dimensional equation of motion. Where ω_n is recognised as the first natural frequency of a simple supported beam (although without π).

As we will apply a Fourier transform in our derivation, we must also change the variables included in the Fourier transform to their non-dimensional equivalents. Substituting Eq. F.1.1 into Eq. 2.2.9, leads to:

$$\tilde{W}(\tilde{x}, \omega) = \frac{1}{\omega_n} \int_{-\infty}^{\infty} \tilde{w}(\tilde{x}, \tilde{t}) \mathrm{e}^{-\mathrm{i}\frac{\omega}{\omega_n}\tilde{t}} d\tilde{t}$$

$$\tilde{w}(\tilde{x}, \tilde{t}) = \frac{1}{2\pi} \int_{\infty}^{\infty} \tilde{W}(\tilde{x}, \omega) \mathrm{e}^{\mathrm{i}\frac{\omega}{\omega_n}\tilde{t}} d\omega \qquad (\text{F.1.3})$$

We are now ready to apply a forward Fourier transform on Eq. F.1.2, doing so leads to:

$$\frac{1}{\omega_n} \tilde{W}'''' - \frac{\omega^2}{\omega_n^3} \tilde{W} = 0 \rightarrow$$

$$\tilde{W}'''' - \eta^2 \tilde{W} = 0, \ \text{with:} \ \eta^2 = \frac{\omega^2}{\omega_n^2}$$

(F.1.4)

To which the general solution may now be written as:

$$\tilde{W}(\tilde{x}, \omega) = A_1 e^{i\tilde{k}\tilde{x}} + A_2 e^{-i\tilde{k}\tilde{x}} + A_3 e^{\tilde{k}\tilde{x}} + A_4 e^{-\tilde{k}\tilde{x}}, \ \text{with:} \ \tilde{k} = \sqrt{\eta}$$

(F.1.5)

We are now ready to derive the Bloch eigenvalues for various periodic structures.

F.1.2 Non-dimensional dispersion curves

Dispersion curves are commonly plotted within the $\omega - \lambda$ plane (or vice versa). As we want to analyse the different band structures, of which the attenuation- bands are depicted by either local resonance or Bragg scatter and where the latter is governed by the properties of the structure itself, it makes sense to non-dimensionalise by using the Bragg resonance condition. Furthermore, the Bloch eigenvalue λ will be replaced by its non-dimensional variant as well.

The latter variable is easily replaced if we take a look at Eq. 2.2.6, and make the following substitution: $\tilde{\lambda} = L\lambda$:

$$\Psi(x + L) = e^{\lambda L} \Psi(x) \rightarrow$$

$$\tilde{\Psi}(\tilde{x}L + L) = e^{\frac{\tilde{\lambda}}{L}L} \tilde{\Psi}(\tilde{x}L) \rightarrow$$

(F.1.6)

$$\tilde{\Psi}(\tilde{x} + 1) = e^{\tilde{\lambda}} \tilde{\Psi}(\tilde{x})$$

Eq. F.1.6 may be used to derive the Bloch eigenvalues.

To non-dimensionalise the axis with ω, we will use the Bragg resonance condition with the non-dimensional wavenumber $\tilde{k}$, the former is written as [45]:

$$k = \frac{n\pi}{L}$$

(F.1.7)

Making the substitution of $k \rightarrow \tilde{k} = \sqrt{\eta}$ and realising that our length L can be dropped for the value of 1 in the non-dimensional case:

$$\sqrt{\eta} = n\pi \rightarrow$$

$$\sqrt{\frac{\eta}{\pi^2}} = n$$

(F.1.8)

If one plots the dispersion curve with the non-dimensional quantities defined in Eqs. F.1.6 and F.1.8 one will see a periodicity of $\tilde{\lambda}$ with π and Bragg-attenuation bands around integer values of n.

F.2 Non-dimensional dispersion curve analysis

F.2.1 Beam on rigid supports

The first structure to be covered is the one with periodic simple supports, spaced at a distance of L. As mentioned in section 2.2.2 this will result in a 2x2 matrix that may be solved for two eigenvalues, giving one Bloch wave in each direction. The derivation is a little bit different as opposed to arbitrary support conditions, as we must first account for the rigid supports. This may be done by solving for two arbitrary constants by enforcing the following two B.C.'s:

$$w(0,t) = 0, \quad w(L,t) = 0 \rightarrow$$

$$L\tilde{w}(0,\tilde{t}) = 0, \quad L\tilde{w}(1,\tilde{t}) = 0 \rightarrow \qquad \text{(F.2.1)}$$

$$\tilde{W}(0,\omega) = 0, \quad \tilde{W}(1,\omega) = 0$$

Using Eq. F.2.1 to solve the constants A_1 and A_2 gives:

$$\tilde{W}(\tilde{x},\omega) = \frac{\left(A_3 \mathrm{e}^{-\mathrm{i}k} - A_3 \mathrm{e}^{k} + A_4 \mathrm{e}^{-\mathrm{i}k} - A_4 \mathrm{e}^{-k}\right)}{\mathrm{e}^{\mathrm{i}k} - \mathrm{e}^{-\mathrm{i}k}} \mathrm{e}^{\mathrm{i}k\tilde{x}} - \frac{\left(A_3 \mathrm{e}^{\mathrm{i}k} - A_3 \mathrm{e}^{k} + A_4 \mathrm{e}^{\mathrm{i}k} - A_4 \mathrm{e}^{-k}\right)}{\mathrm{e}^{\mathrm{i}k} - \mathrm{e}^{-\mathrm{i}k}} \mathrm{e}^{-\mathrm{i}k\tilde{x}} + A_3 \mathrm{e}^{k\tilde{x}} + A_4 \mathrm{e}^{-k\tilde{x}} \qquad \text{(F.2.2)}$$

Now, to apply the transfer matrix method, we set-up two B.C.'s at the connection of two elements, i.e. continuity of rotations and moments, giving:

$$\tilde{W}'_n = \tilde{W}'_{n+1}, \quad \tilde{W}''_n = \tilde{W}''_{n+1} \qquad \text{(F.2.3)}$$

With Eq. F.2.3 the problem statement is complete and one can follow the steps from section 2.2.2 to derive the Bloch eigenvalues. As this derivation is a bit lengthy regarding the equations, we will only show the final result when the determinant is cast into the same form as Eq. 11i from [51]:

$$\cosh\left(\tilde{\lambda}\right) = -\frac{\cos\left(\tilde{\lambda}\right)\sinh\left(\tilde{\lambda}\right) - \cosh\left(\tilde{\lambda}\right)\sin\left(\tilde{\lambda}\right)}{\sin\left(\tilde{\lambda}\right) - \sinh\left(\tilde{\lambda}\right)} \qquad \text{(F.2.4)}$$

Which is exactly the same.

The results will be given in the form of two graphs. The first will show all the eigenvalues, whereas the second will only show the real parts as to discern the various propagation- and attenuation-bands.

(a) All eigenvalues
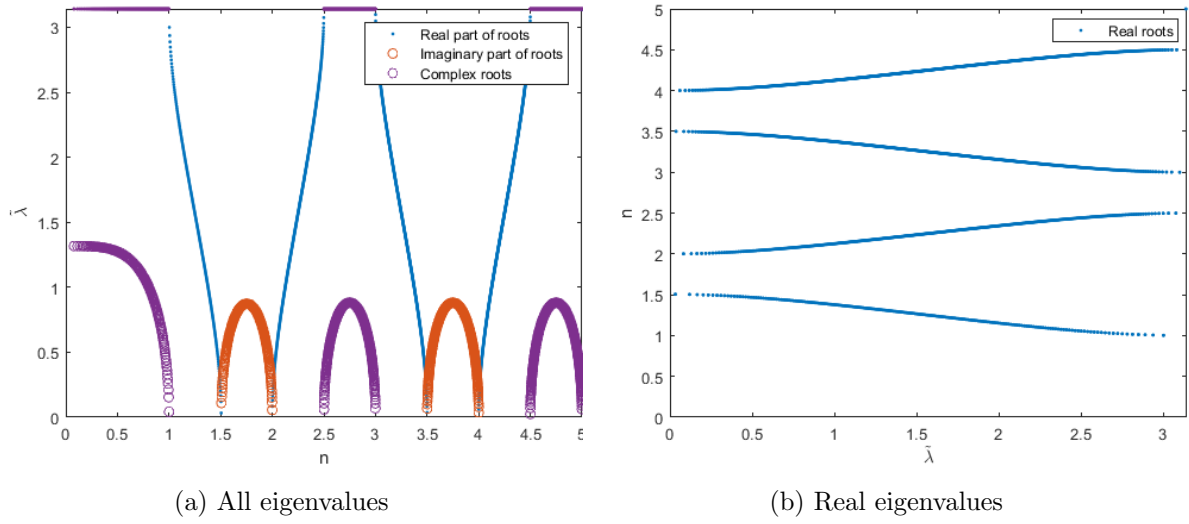
(b) Real eigenvalues

Figure F.1: Bloch eigenvalues for rigid supports

As can be seen from Fig. F.1a we indeed have wave attenuation around the Bragg resonance frequencies, denoted by the integer values of n. However, these zones are also characterised by values of $n = 1.5, 2.5$ etc. As mentioned by Mead [32], the upper bounding frequencies of the attenuation zones are given by the natural frequency of the single element on simple supports (pinned-pinned): $\omega_{n,pp} = (\frac{n\pi}{L})^2\sqrt{\frac{EI}{m}} = (n\pi)^2\omega_n$. Whilst the lower bounding frequencies are given by clamped-clamped frequencies, i.e. $\omega_{n,cc} = (n - \frac{1}{2})^2(\frac{\pi}{L})^2\sqrt{\frac{EI}{m}} = (n - \frac{1}{2})^2\pi^2\omega_n$. When dividing the excitation frequency by either of these bounding frequencies whilst leaving out the part varying with n they can be rewritten as:

$$\frac{\omega}{\omega_{n,pp}}, \qquad \frac{\omega}{\omega_{n,cc}}$$

$$\frac{\omega}{\pi^2\omega_n} = n^2, \quad \frac{\omega}{\pi^2\omega_n} = (n - \tfrac{1}{2})^2 \qquad\qquad \text{(F.2.5)}$$

$$\sqrt{\frac{\eta}{\pi^2}} = n, \quad \sqrt{\frac{\eta}{\pi^2}} = (n - \tfrac{1}{2})$$

From which we can clearly see that the attenuation zones where no wave propagation occurs are bounded by the natural frequencies. This makes sense, as waves with frequencies $\omega_{n,pp}$ or $\omega_{n,cc}$ in a single element add up to form a standing wave, causing the Bragg resonance in a periodic structure. From Fig. F.1b the various propagation bands are clearly observed as well, do note that at the edge of the Brillouin zone $\frac{d\omega}{dk} = 0$, i.e. at the bounding frequencies, giving a zero group-velocity and thus indeed no energy propagation.

F.2.2 Beam on spring supports

The next structure to be analysed is one with spring supports. Although the B.C.'s are practically the same as in Eq. 2.2.11, we should write them in their non-dimensional form. Therefore we will start from scratch again. First, write down the general B.C.'s at the support:

$$w_n(x,t)|_{x=L} = w_{n+1}(x,t)|_{x=0}, \qquad w'_n(x,t)|_{x=L} = w'_{n+1}(x,t)|_{x=0}$$

$$w''_n(x,t)|_{x=L} = w''_{n+1}(x,t)|_{x=0}, \quad w'''_n(x,t)|_{x=L} - k_s w_n(x,t)|_{x=L} = w'''_{n+1}(x,t)|_{x=0} \tag{F.2.6}$$

Replacing the variables with their non-dimensional counterparts gives us:

$$\tilde{w}_n(\tilde{x},\tilde{t})|_{\tilde{x}=1} = \tilde{w}_{n+1}(\tilde{x},\tilde{t})|_{\tilde{x}=0}, \qquad \tilde{w}'_n(\tilde{x},\tilde{t})|_{\tilde{x}=1} = \tilde{w}'_{n+1}(\tilde{x},\tilde{t})|_{\tilde{x}=0}$$

$$\tilde{w}''_n(\tilde{x},\tilde{t})|_{\tilde{x}=1} = \tilde{w}''_{n+1}(\tilde{x},\tilde{t})|_{\tilde{x}=0}, \quad \tilde{w}'''_n(\tilde{x},\tilde{t})|_{\tilde{x}=1} - \alpha_s \tilde{w}_n(\tilde{x},\tilde{t})|_{\tilde{x}=1} = \tilde{w}'''_{n+1}(\tilde{x},\tilde{t})|_{\tilde{x}=0} \tag{F.2.7}$$

Where $\alpha_s = \frac{k_s L^3}{EI}$ denotes the non-dimensional parameter representing the ratio of the stiffness of the support to that of the beam. As there are no time derivatives present in Eqs. F.2.7, we may write their counterparts in the frequency domain without any changes:

$$\tilde{W}_n(\tilde{x},\omega)|_{\tilde{x}=1} = \tilde{W}_{n+1}(\tilde{x},\omega)|_{\tilde{x}=0}, \qquad \tilde{W}'_n(\tilde{x},\omega)|_{\tilde{x}=1} = \tilde{W}'_{n+1}(\tilde{x},\omega)|_{\tilde{x}=0}$$

$$\tilde{W}''_n(\tilde{x},\omega)|_{\tilde{x}=1} = \tilde{W}''_{n+1}(\tilde{x},\omega)|_{\tilde{x}=0}, \quad \tilde{W}'''_n(\tilde{x},\omega)|_{\tilde{x}=1} - \alpha_s \tilde{W}_n(\tilde{x},\omega)|_{\tilde{x}=1} = \tilde{W}'''_{n+1}(\tilde{x},\omega)|_{\tilde{x}=0} \tag{F.2.8}$$

With Eqs. F.2.8 the problem statement is complete and we follow the same steps as before to derive the determinant and with that calculate the Bloch eigenvalues.

To give an idea of the influence of the non-dimensional parameter α_s, the following values will be used to plot the results: $\alpha_s = 0.1, 10, 100, 500, 1000$. These results may be found in the figures below.

(a) All eigenvalues   (b) Real eigenvalues
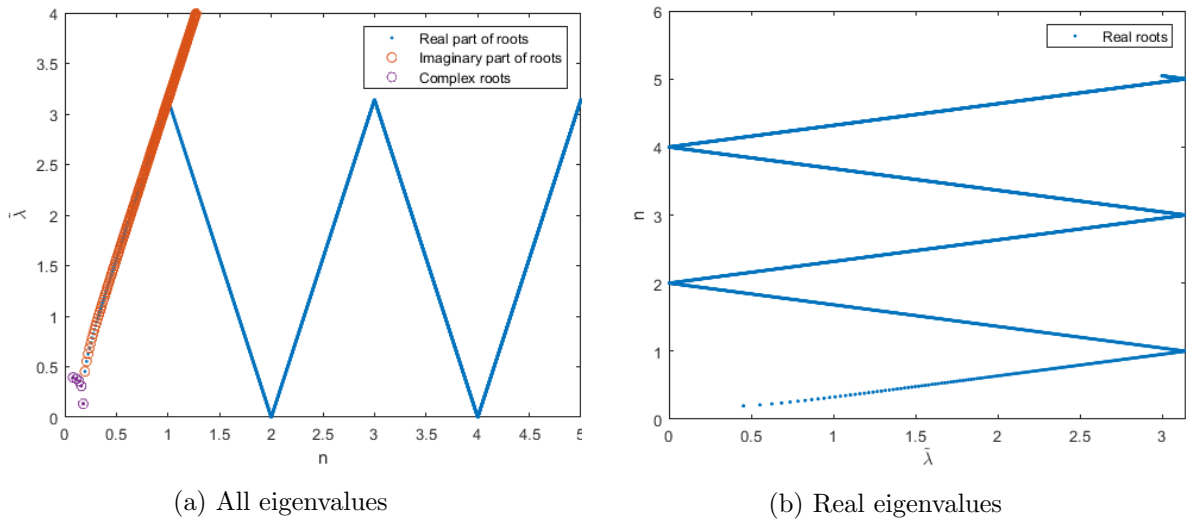
Figure F.2: Bloch eigenvalues for $\alpha_s = 0.1$

(a) All eigenvalues
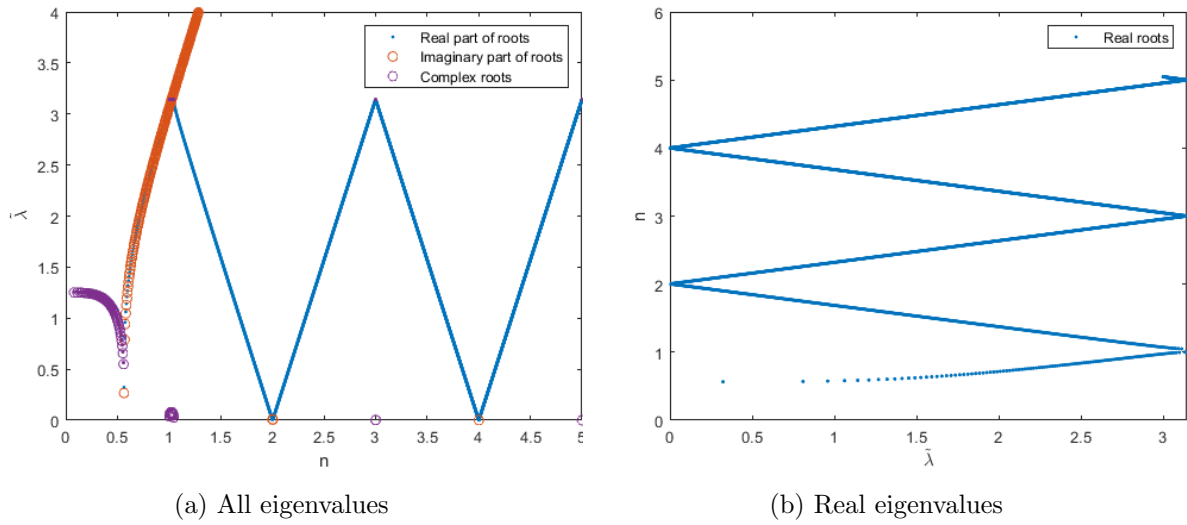
(b) Real eigenvalues

Figure F.3: Bloch eigenvalues for $\alpha_s = 10$

(a) All eigenvalues
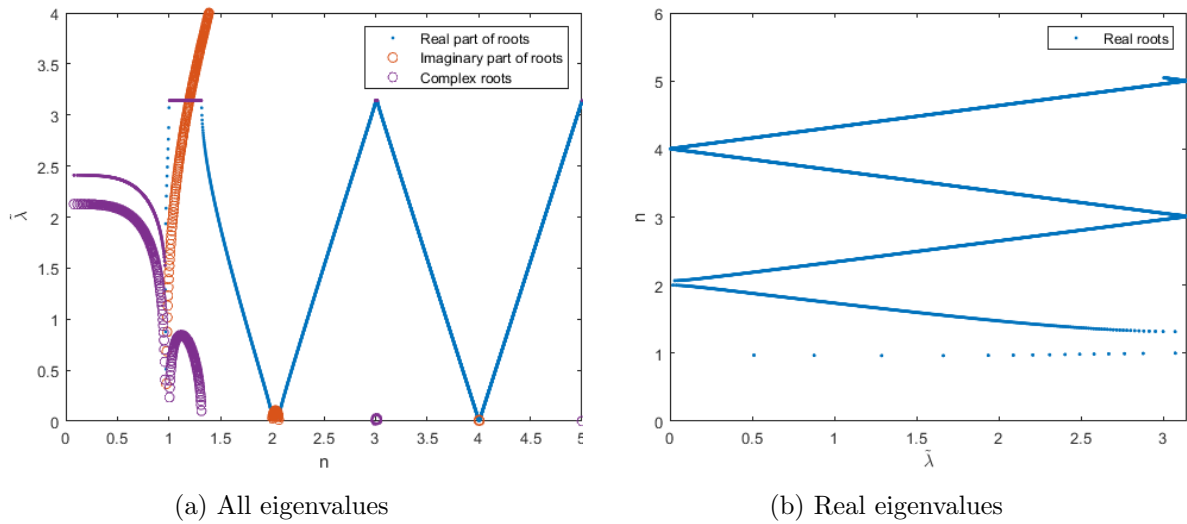
(b) Real eigenvalues

Figure F.4: Bloch eigenvalues for $\alpha_s = 100$

From the figures it becomes apparent that at low values of α_s we will have complex waves without wave propagation at low values of η only. With increasing values this zone, starting from $\eta = 0$, becomes larger whilst also increasing the imaginary part of one of the complex waves. As the imaginary part dictates the wave decay, if we would increase α_s indefinitely (i.e. to ∞) we would regain the results from the beam with rigid supports. Essentially one of the waves would become so weak that it does not participate anymore.

Furthermore, at low values of α_s there are no Bragg resonance bands. Instead the direction of the wave motion reverses at the integer values of n (corresponding to the natural frequencies of a single simple supported beam), without the group velocity going to zero. This behaviour changes with increasing values of α_s as well. First of all, the propagation bands close to the 'touch-down' point of the complex waves get shifted, effectively decreasing the propagation bands within the frequency spectrum. The group-velocity for these propagation bands now also tend to return to

(a) All eigenvalues (b) Real eigenvalues
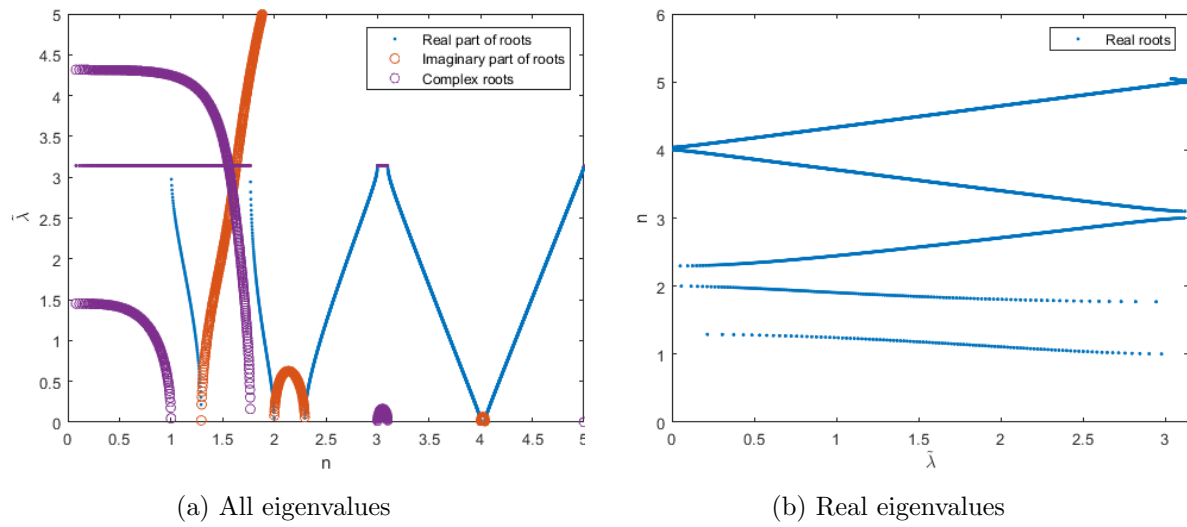
Figure F.5: Bloch eigenvalues for $\alpha_s = 500$

zero near the edge of the first Brillouin zone. Secondly, the Bragg resonance bands also increase in width, although this effect is not that strong and diminishes for higher values of η.

(a) All eigenvalues
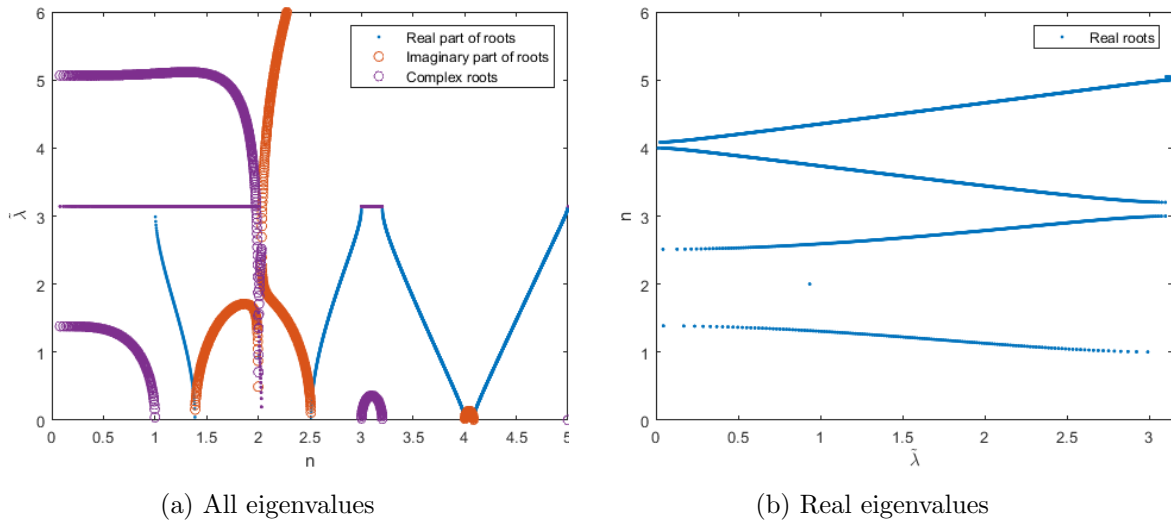
(b) Real eigenvalues

Figure F.6: Bloch eigenvalues for $\alpha_s = 1000$

Physically, this means that it would be beneficial to have stiff supports, as these will prevent most waves from travelling without attenuation, influencing the far field. However, this effect would mainly be felt at values of ω below ω_n since the increase in width of the higher Bragg resonance bands is only small.

F.2.3 Periodic beam on complex supports

The next structure is similar to the one in Fig. B.2, such that we add a DoF in the form of the sleepers between periodic elements. All the B.C.'s from Eq. F.2.8 remain valid except for Eq. F.2.8c. In that case we have to derive the EoM for the sleeper DoF as well.
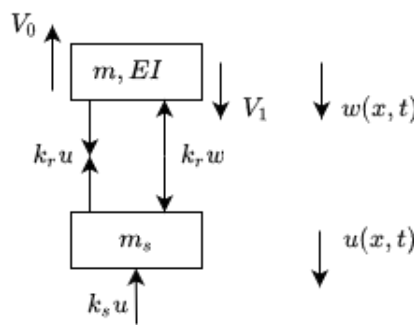
Figure F.7: Shear force equilibrium

To start, write the EoM for the sleeper as governed by Fig. F.7, rewrite in non-dimensional form and transform to the frequency domain:

$$m_s \ddot{u}(x,t) = -(k_r + k_s)u(x,t) + k_r w(x,t)$$

$$m_s \omega_n^2 \ddot{\tilde{u}}(\tilde{x}, \tilde{t}) = -(k_r + k_s)\tilde{u}(\tilde{x}, \tilde{t}) + k_r \tilde{w}(\tilde{x}, \tilde{t})$$

$$-m_s \omega^2 \tilde{U}(\tilde{x}, \omega) = -(k_r + k_s)\tilde{U}(\tilde{x}, \omega) + k_r \tilde{W}(\tilde{x}, \omega)$$

(F.2.9)

$$\tilde{U}(\tilde{x}, \omega) = \frac{k_r}{-m_s \omega^2 + k_r + k_s} \tilde{W}(\tilde{x}, \omega)$$

By introducing the following non-dimensional parameters: $\eta_r = \frac{\omega_r}{\omega_n}$, and $\eta_s = \frac{\omega_s}{\omega_n}$ into Eq. F.2.9d, we can rewrite as follows:

$$\tilde{U}(\tilde{x}, \omega) = \frac{\eta_r^2}{-\eta^2 + \eta_r^2 + \eta_s^2} \tilde{W}(\tilde{x}, \omega) \tag{F.2.10}$$

Next, write the force equilibrium of the beam itself, governed by Fig. F.7 and substitute Eq. F.2.10:

$$-V_0 + k_r u(x,t) - k_r w(x,t) + V_1 = 0$$

$$EI w_n'''(x,t)|_{x=L} + k_r u(x,t) - k_r w_n(x,t)|_{x=L} - EI w_{n+1}''''(x,t)|_{x=0} = 0$$

$$\tilde{w}_n'''(\tilde{x}, \tilde{t})|_{\tilde{x}=1} + \alpha_r \tilde{u}(\tilde{x}, \tilde{t}) - \alpha_r \tilde{w}_n(\tilde{x}, \tilde{t})|_{\tilde{x}=1} - \tilde{w}_{n+1}'''(\tilde{x}, \tilde{t})|_{\tilde{x}=0} = 0$$

(F.2.11)

$$\tilde{W}_n'''(\tilde{x}, \omega)|_{\tilde{x}=1} + \alpha_r \left(\frac{\eta_r^2}{-\eta^2 + \eta_r^2 + \eta_s^2} - 1 \right) \tilde{W}_n(\tilde{x}, \omega)|_{\tilde{x}=1} - \tilde{W}_{n+1}'''(\tilde{x}, \omega)|_{\tilde{x}=0} = 0$$

Where $\alpha_r = \frac{k_r L^3}{EI}$ denoting the ratio of stiffness of the uppermost spring with the beam. Regarding the sleeper modelled as a mass, we expect resonance if the denominator in Eq. F.2.10 goes to zero. This is the case if the following equality is met:

$$\eta = \sqrt{\eta_r^2 + \eta_s^2} \tag{F.2.12}$$

That is, when the excitation frequency is equal to the natural frequency of the mass: $\omega = \omega_s = \sqrt{\frac{k_r + k_s}{m_s}}$. Around this area, depending on the value of both η_r and η_s.

In regard of the qualitative assessment of the influence of the parameters α_s, η_r, and η_s, various values have been (addmittedly arbitrary) chosen. In case of the value of α_s, the values of 0.1 and 100 has been chosen. Such that we can tune resonance to occur either inside or outside the complex wave band. Furthermore, regarding the values of η_r and η_s it was chosen to tune those in order to investigate their influence in relation to each other. As the mathematical format of Eq. F.2.10, and physical interpretation, suggests that the upper spring has a significant influence on the response. In this case, it was chosen to tune them with both η_r and η_s either being equal to one and alternate their values as to attain resonance around $n \approx 1.5$. To this end the value of $\eta_i = 25.26$ has been used and $\eta_i = 17.86$ in the case they are equal to each other, this follows from Eq. F.2.12.

(a) All eigenvalues
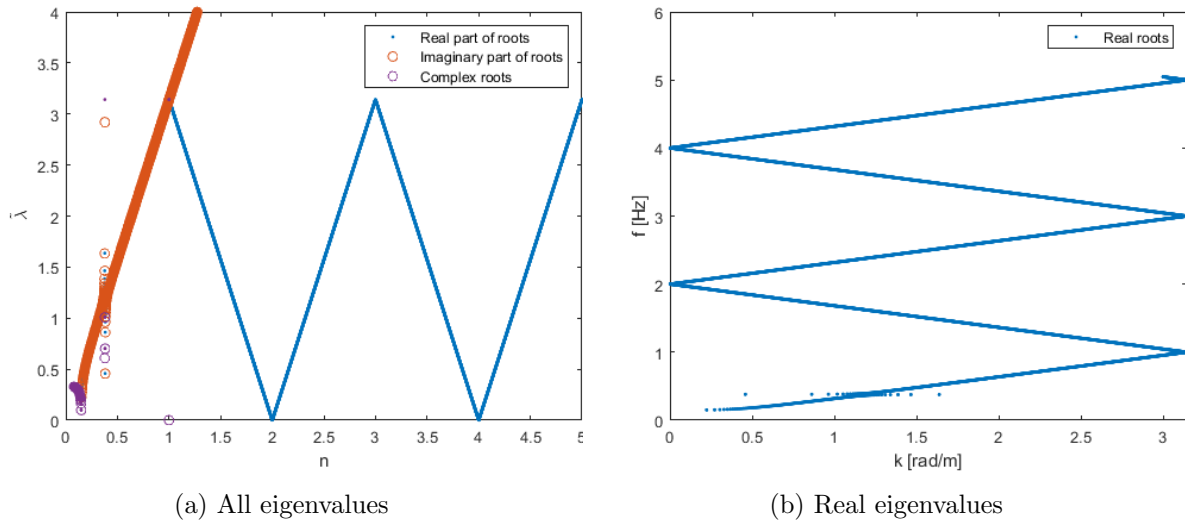
(b) Real eigenvalues

Figure F.8: Bloch eigenvalues for $\alpha_s = 0.1$, $\eta_r = 1$, $\eta_s = 1$

(a) All eigenvalues
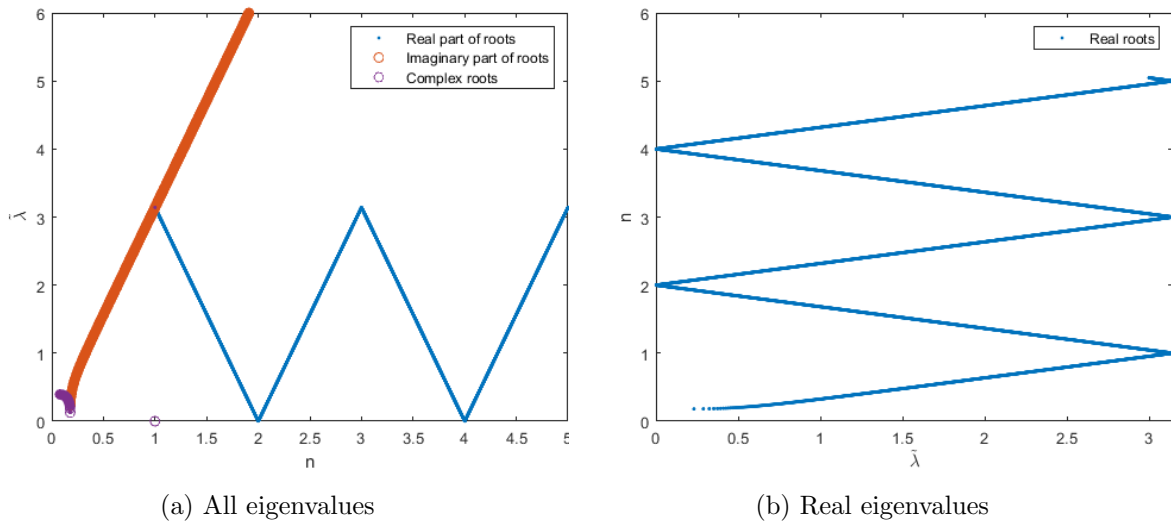
(b) Real eigenvalues

Figure F.9: Bloch eigenvalues for $\alpha_s = 0.1$, $\eta_r = 1$, $\eta_s = 25.26$

From Figs. F.8 to F.11 we can see that at low values of α_s the influence of the resonance on the response of the beam is negligible as opposed to Figs. F.12 to F.15, where we can see it heavily influences the dispersion curves. Regarding the resonance itself, η_r has the most pronounced effect. If one compares Fig. F.10 with Fig. F.11, we can see that the effect of the resonance is smaller in the latter case and even completely disappears in Fig. F.9.

Furthermore, increasing values of η_r will counter the effect that α_s has on the dispersion curves. This may be seen in Figs. F.10 and F.14a, where the complex wave band is much more narrow.

(a) All eigenvalues
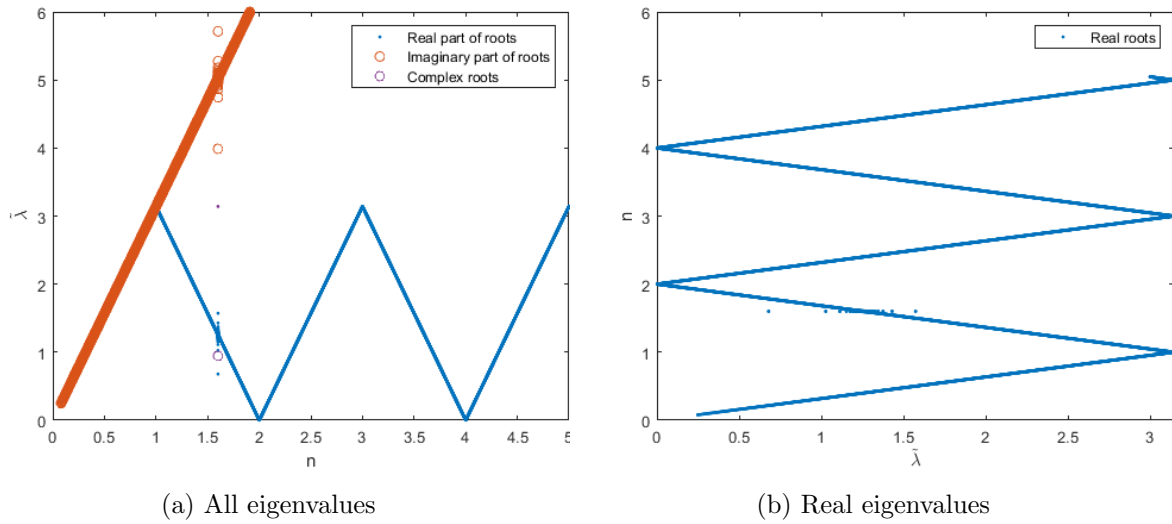
(b) Real eigenvalues

Figure F.10: Bloch eigenvalues for $\alpha_s = 0.1$, $\eta_r = 25.26$, $\eta_s = 1$

(a) All eigenvalues
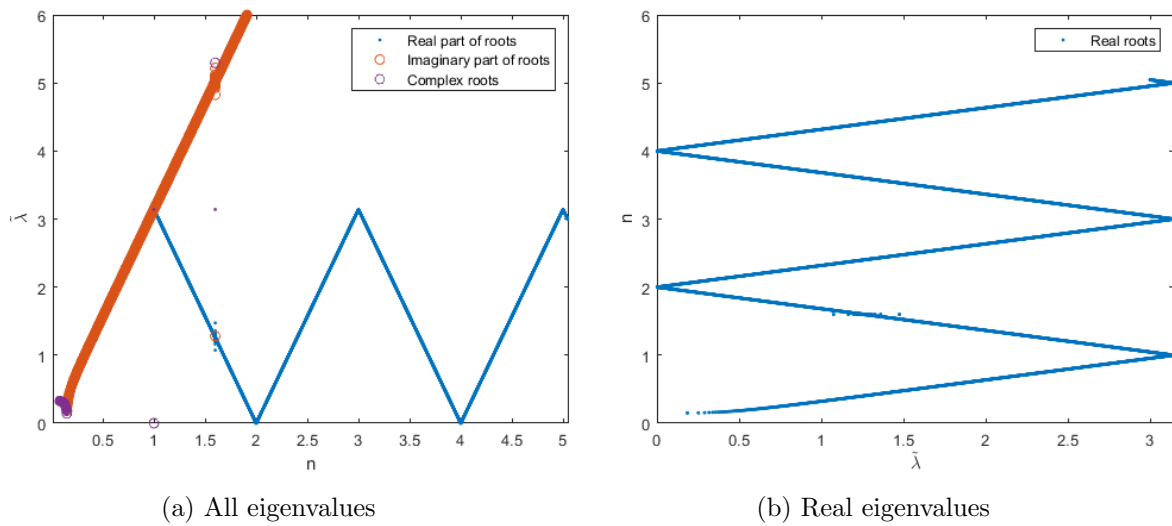
(b) Real eigenvalues

Figure F.11: Bloch eigenvalues for $\alpha_s = 0.1$, $\eta_r = 17.86$, $\eta_s = 17.86$

(a) All eigenvalues
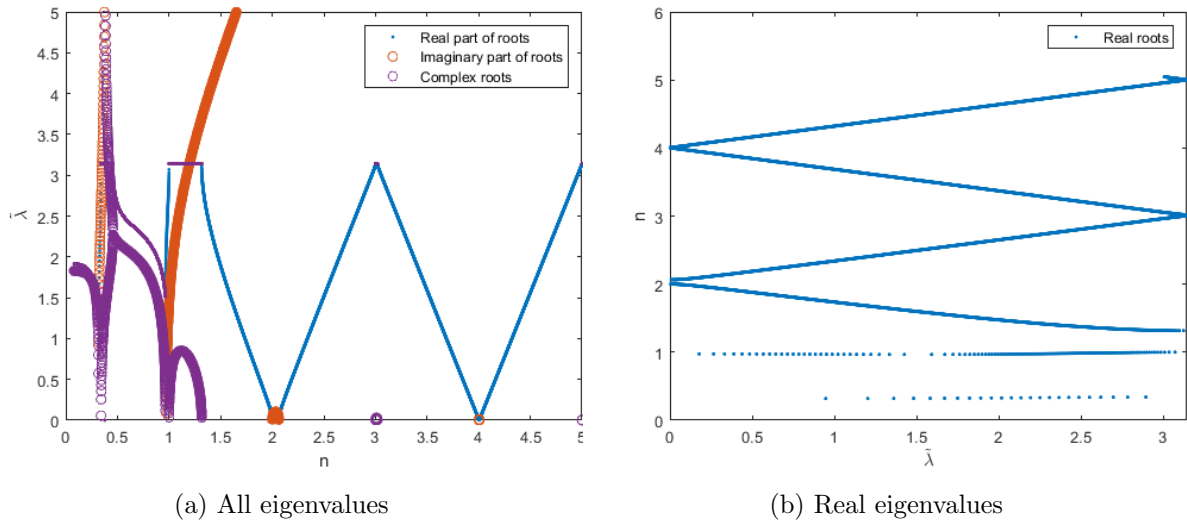
(b) Real eigenvalues

Figure F.12: Bloch eigenvalues for $\alpha_s = 100$, $\eta_r = 1$, $\eta_s = 1$

(a) All eigenvalues
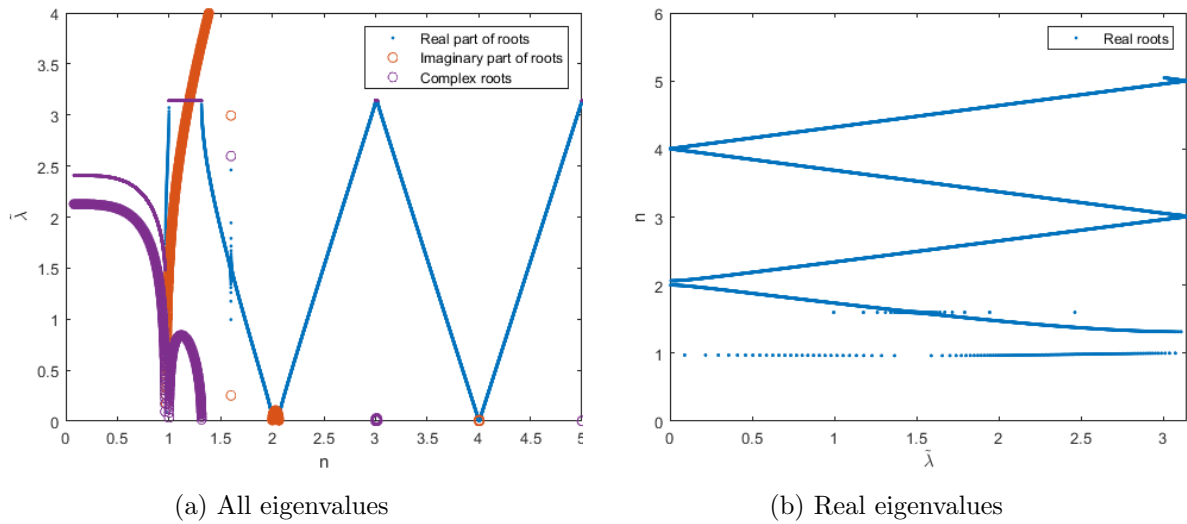
(b) Real eigenvalues

Figure F.13: Bloch eigenvalues for $\alpha_s = 100$, $\eta_r = 1$, $\eta_s = 25.26$

(a) All eigenvalues
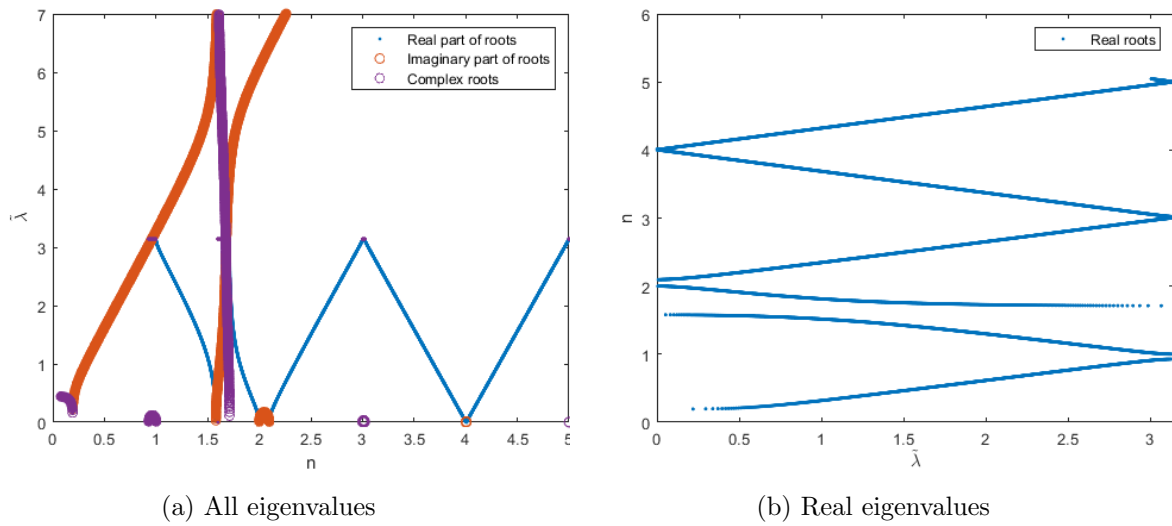
(b) Real eigenvalues

Figure F.14: Bloch eigenvalues for $\alpha_s = 100$, $\eta_r = 25.26$, $\eta_s = 1$

(a) All eigenvalues
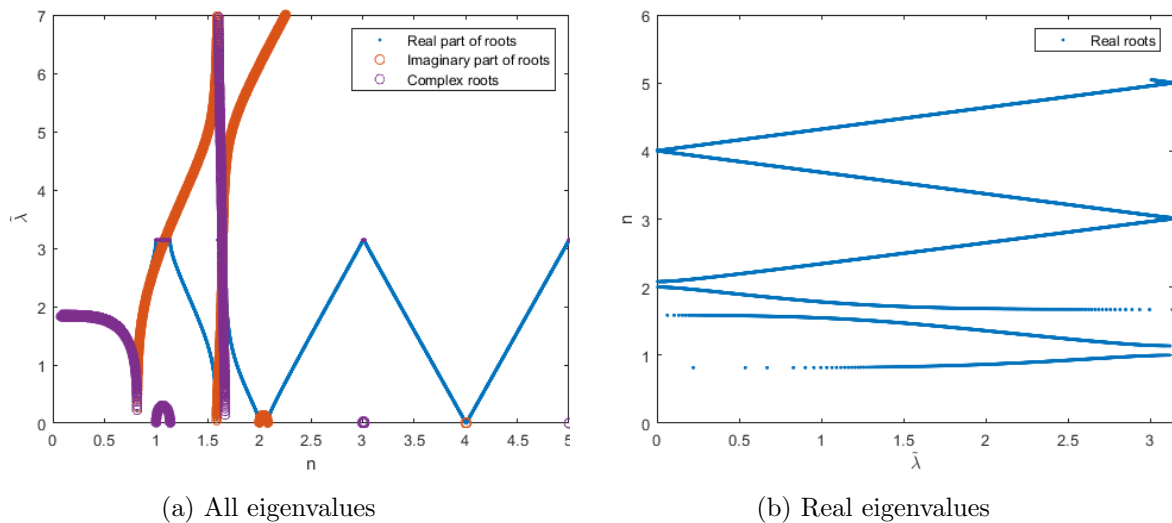
(b) Real eigenvalues

Figure F.15: Bloch eigenvalues for $\alpha_s = 100$, $\eta_r = 17.86$, $\eta_s = 17.86$